The Reliability of Zinc Oxide Based Thin Film Transistors Under Extreme Conditions

by

Kosala Indrajith Yapa Bandara

A dissertation submitted to the Graduate Faculty of
Auburn University
in partial fulfillment of the
requirements for the Degree of
Doctor of Philosophy

Auburn, Alabama
May 5, 2018

Keywords: ZnO TFTs, Radiation effect, Proton irradiation, Defects

Approved by

Minseo Park, Chair, Professor of Physics
Michael Bozack, Professor of Physics
Sarit Dhar, Associate Professor of Physics
Michael C. Hamilton, Associate Professor of Electrical & Computer Engineering
Dong-Joo Kim, Alumni Professor of Materials Research & Education Center

Abstract

In this Ph.D. dissertation, I report the device instability of ZnO thin film transistors (TFTs) under extreme environmental conditions. It is extremely important to identify the cause of device instability under different environmental conditions. The types of defects and its influence in ZnO TFT performance have been analyzed in this work.

The device instability under electrical stressing and subsequent relaxation have been investigated for ZnO TFTs. A systemic comparison between ambient and vacuum conditions was carried out to investigate the effect of adsorption of oxygen and water molecules, which leads to the creation of defects in the channel layer. The observed subthreshold swing and change in field effect mobility under gate bias stressing have supported the fact that oxygen and moisture directly affect the threshold voltage (V_{TH}) shift. We have presented the comprehensive analysis of device relaxation under both ambient and vacuum conditions to further confirm the defect creation and charge trapping/de-trapping process since it has not been reported before. It was hypothesized that chemisorbed molecules form acceptor-like traps and can diffuse into the ZnO thin film through the void on the grain boundary, being relocated even near the semiconductor/dielectric interface. The stretched exponential and power-law model fitting reinforces the conclusion of defect creation by oxygen and moisture adsorption on the active layer.

I have investigated the displacement damage (DD) effect on the electrical characteristics of ZnO thin film transistors (TFTs) based on its location of origin in the device structure. The

area subjected to maximum proton dose induces maximum DD effect in that particular location. ZnO TFTs with two different passivation layer thicknesses were prepared to obtain maximum proton dose distribution in either the ZnO channel layer or ZnO/SiO_2 interface. The devices were irradiated by a proton beam with an energy 200 keV and 1×10^{14} protons/cm^2 fluence. Transport of Ions in Matter (TRIM) simulation, followed by calculation of depth distribution of the non-ionizing energy loss (NIEL), illustrated different proton dose distribution profiles and NIEL profiles along the depth of the device for these two types of samples. The sample with maximum proton dose peak at the ZnO/SiO_2 interface exhibited a significant degradation in device electrical characteristics after the irradiation compared to negligible degradation of the sample where the maximum proton dose was absorbed in the ZnO layer. Therefore, one must be cautious when studying the radiation hardness of proton-irradiated ZnO TFTs since the displacement damage induces drastic changes on the device characteristics based on the damage location.

Acknowledgments

I would like to convey my most profound gratitude to my supervisor, Dr. Minseo Park, for his guidance and support throughout the last four years. Without his patience, wisdom, and motivation, it would not have been possible for me to succeed in this program. I am also thankful to Dr. Michael Bozack, Dr. Sarit Dhar, and Dr. Michael Hamilton for agreeing to serve as my dissertation committee members and for evaluating this work. I would like to thank Dr. Dong-Joo Kim for accepting my invitation to be the university reader for my dissertation.

Also, I am grateful to Dr. Claude Ahyi for his invaluable time spent on intellectual discussions, instrument training and design of experiments. His inputs have made a more significant impact on my successful research work. I appreciate Mrs. Tamara Isaac-Smith for her assistance in proton irradiation experiment planning and instrument training. I am so thankful to Mr. Max Cichon for his contribution to building and troubleshooting the instruments so I could continue my research work without any disturbances. AU IGP and Walter professorship funded the research projects. I would like to thank Mr. Vincent Salva from Intellectual property developers, LLC. (vpsuss@aol.com) for additional support.

I would like to express my heartful gratitude to my beloved wife, Ayani, for her love, support, understanding, and encouragement throughout my graduate school time. I would also like to thank my parents Thilak Yapa Bandara and Prema Galpothawela for their unconditional love, support, patience and encouragement in my whole life. Finally, I praise the guidance of my life, Lord Buddha for his blessings for my success.

Table of Contents

List of Tables

List of Figures

List of Abbreviations

AC	Alternating Current
ADX	Angular Dispersive X-ray Diffraction
BE^*	Bound Exciton
BE	Binding Energy
CCD	Charge-Coupled Detector
CCP	Capacitively Coupled Plasma
C-V	Capacitance-Voltage
CVD	Chemical Vapor Deposition
DC	Direct Current
DD	Displacement Damage
DI	Deionized
ECR	Electron Cyclone Resonance
EDX	Energy Dispersive X-ray Diffraction
EHP	Electron-Hole Pair
FCC	Face Centered Cubic
FE	Free Exciton
FET	Field Effect Transistor
FWHM	Full-Width at Half Maximum
HCP	Hexagonal Close-packed

ICB	Intercontinental Ballistic Missiles
ICP	Inductively Coupled Plasma
IR	Infrared
ITO	Indium-Tin-Oxide
I-V	Current-Voltage
KE	Kinetic Energy
LDA	Local Density Approximation
LO	Longitudinal Optical
LPP	Longitudinal Phonon Plasmon
LTMO	Linear Muffin-Tin Orbital
MBE	Molecular Beam Epitaxy
MEA	Monoethanolamine
MFS	Minimum Feature Size
MIS	Metal-Insulator-Semiconductor
MOSFET	Metal-Oxide-Semiconductor Field Effect Transistor
NIEL	Non-Ionizing Energy Loss
OFET	Organic Field Effect Transistor
PL	Photoluminescence
PLD	Pulsed Laser Deposition
PTAA	Ploy triarylamine
RF	Radio Frequency

RHA	Radiation Hardness Assurance
RHESE	Radiation Hardened Electronics for Space Environment
RIE	Reactive Ion Etching
RTA	Rapid Thermal Annealing
STEM	Scanning Transmission Electron Microscopy
SS	Subthreshold Swing
TFT	Thin Film Transistor
TID	Total Ionizing Dose
TLM	Transmission Line Model
TO	Transverse Optical
TRIM	Transport of Ion in Matters
TRM	Triple Module Redundancy
UV	Ultra-Violet
XAS	X-ray Absorption Spectroscopy
XRD	X-ray Diffraction Spectroscopy

Chapter 1
Introduction

The history of Zinc goes back to as early as the first century A.D. Ancient Romans have used zinc in the fabrication process of brass and also a Greek physician, pharmacologist, and botanist named Pedanius Dioscorides have described the oxidation of zinc in his book, "De Materia Medica." However, the first record of recognition for zinc as a metal dated back to 14th century in India. Zinc Oxide (ZnO) was a byproduct of the smelting process in jewelry production [1]. Then the smelting technology was spread to China in the 16th or 17th century to be used in brass manufacturing with high zinc composition. Europeans imported zinc from China around the same period. Zinc was first introduced to the periodic table as an element by a French chemist, Antoine Lavoisier in 1789 [2]. Before the electrical and optical properties of ZnO were discovered, ZnO powder was used in oil-based paints in the late 1800s. The first application of ZnO in electronics was in ZnO radios in the 1920s [3]. The Schottky barrier created by contacting a copper wire with ZnO crystal was utilized in the process of AC radio wave converted into DC signals. The first significant application of ZnO in electronic was the varistors, which a component uses to protect circuits against excessive transient voltages.

ZnO was one of the materials that got attention in the 20th century with the improvement of material analysis. The first electron diffraction data on ZnO was published in 1935 [4]. After three years, the first scanning transmission electron microscopic (STEM) image was taken on ZnO crystal [5]. The undoped n-type conductivity ZnO was experimentally identified by the temperature dependent Hall measurements in 1954 [6]. In the same year, the optical properties of ZnO were initially studied by a German research group [7]. Since then ZnO has been extensively

studied for its electrical and optical properties. ZnO is one of the essential materials in nanotechnology due to its varieties in self-assembled nanostructured forms. Moreover, the transparency of visible light has made ZnO an ideal candidate material for transparent electronics. The softness of the ZnO films is another property which introduced ZnO for flexible electronics. Flat panel display technology and solar cell industry require transparent conductive oxides. The conductivity of ZnO can be significantly increased by doping with Al, B, and Ga. The inexpensive large-scale deposition capability and abundancy of ZnO show potential to replace expensive Indium-Tin oxide (ITO) in flat panel display technology. However, ZnO still requires more improvements to make to enhance its quality and durability to compete with ITO.

ZnO can be comparable to GaN due to its similar properties such as direct wide bandgap, wurtzite crystal structure, and break down voltage [8]–[10]. Further, ZnO has some advantages over GaN such as larger excitonic binding energy (60 meV) [11], [12] and its availability as large single crystal [11]. The ZnO growth on native substrate yields a lower concentration of extended defects compared to GaN, which results in higher electrical and optical device performances [13]–[15]. Also, ZnO shows amenability to wet chemical etching, unlike GaN. This property is an added advantage in device fabrication process. However, the use of ZnO as an alternative for GaN has been limited with difficulty to obtain stable p-type conductivity in ZnO [14], [15]. There are several reports which claim proper p-type doping in ZnO with appropriate hole concentrations and hole mobility [16], [17]. However, the reliability and the reproducibility are still inadequate to make a strong claim.

ZnO is an inorganic material with high spontaneous polarization. Hence, the surface of ZnO is prone to contaminated by adsorbed elements in the ambient air. Therefore, the conductivity of ZnO film shows high sensitivity towards absorbents. In a way, this nature of ZnO is useful as

in gas sensors to detect gas contaminations [18], and also as odor sensors to identify the freshness of food and drinks [19]. But the surface sensitivity causes electrical instability in ZnO thin film transistors (TFTs) and consequently, limiting its applicability in logic circuits. Extensive researches have done to investigate the surface sensitivity effect on device instability of ZnO based TFTs [20]–[22]. It is essential to study the mechanism of defect creation and its influence on the electrical performance of devices. In chapter 5 of this dissertation, a model is proposed to explain the defect creation mechanism when ZnO TFTs are operating under constant gate bias in ambient air.

The radiation hardness of ZnO has been reported as higher than other semiconductor materials such as GaN, Si, GaAs, and CdS [23]–[25]. With the advancement of space exploration, it was a necessity to employ electronics onboard of space crafts to operate without getting damaged by high energy radiation in space. Different types of defects are generated in the device structure to influence the device operations based on the type of radiation. ZnO TFTs have been studied for its radiations hardness against charged particle irradiations such as electrons [23], [25], [26], protons [27]–[29], and photons (gamma rays) [30], [31]. In chapter 6, the formation of displacement damage due to the energetic proton irradiation in rf-sputtered ZnO films and its effect on the ZnO TFT performances were investigated, and the results are discussed. Further, the proton radiation-induced damage mechanisms in ZnO/SiO_2 interface and SiO_2 dielectric layer were investigated by using sol-gel derived ZnO TFTs. The results and conclusion are reported in appendix II.

References

[1] V. Deshpande, "(04) A Note on Ancient Zinc-Smelting in India and China," 1996.

[2] J. R. Partington, *A short history of chemistry*. Courier Corporation, 1960.

[3] C. Jagadish and S. J. Pearton, *Zinc oxide bulk, thin films and nanostructures: processing, properties, and applications*. Elsevier, 2011.

[4] H. J. Yearian, "Intensity of diffraction of electrons by ZnO," *Phys. Rev.*, vol. 48, no. 7, p. 631, 1935.

[5] M. Von Ardenne, "The scanning electron microscope: Practical construction," *Z Phys*, vol. 19, pp. 407–416, 1938.

[6] H. B. Harrison, *Characterizing metal semiconductor ohmic contacts*. Royal Melbourne Institute of Technology, 1980.

[7] F. A. Kröger and H. J. Vink, "The origin of the fluorescence in self-activated ZnS, CdS, and ZnO," *J. Chem. Phys.*, vol. 22, no. 2, pp. 250–252, 1954.

[8] D. G. Thomas, "The exciton spectrum of zinc oxide," *J. Phys. Chem. Solids*, vol. 15, no. 1–2, pp. 86–96, 1960.

[9] D. C. Reynolds, D. C. Look, B. Jogai, C. W. Litton, G. Cantwell, and W. C. Harsch, "Valence-band ordering in ZnO," *Phys. Rev. B*, vol. 60, no. 4, p. 2340, 1999.

[10] Y. Chen *et al.*, "Plasma-assisted molecular beam epitaxy of ZnO on c-plane sapphire: Growth and characterization," *J. Appl. Phys.*, vol. 84, no. 7, pp. 3912–3918, 1998.

[11] D. C. Reynolds, D. C. Look, and B. Jogai, "Optically pumped ultraviolet lasing from ZnO," *Solid State Commun.*, vol. 99, no. 12, pp. 873–875, 1996.

[12] D. M. Bagnall *et al.*, "Optically pumped lasing of ZnO at room temperature," *Appl. Phys. Lett.*, vol. 70, no. 17, pp. 2230–2232, 1997.

[13] D. C. Look, “Recent advances in ZnO materials and devices,” *Mater. Sci. Eng. B*, vol. 80, no. 1–3, pp. 383–387, 2001.

[14] Ü. Özgür *et al.*, “A comprehensive review of ZnO materials and devices,” *J. Appl. Phys.*, vol. 98, no. 4, p. 11, 2005.

[15] N. H. Nickel and E. Terukov, *Zinc Oxide-A Material for Micro-and Optoelectronic Applications: Proceedings of the NATO Advanced Research Workshop on Zinc Oxide as a Material for Micro-and Optoelectronic Applications, held in St. Petersburg, Russia, from 23 to 25 June 2004*, vol. 194. Springer Science & Business Media, 2006.

[16] D. C. Look, D. C. Reynolds, C. W. Litton, R. L. Jones, D. B. Eason, and G. Cantwell, “Characterization of homoepitaxial p-type ZnO grown by molecular beam epitaxy,” *Appl. Phys. Lett.*, vol. 81, no. 10, pp. 1830–1832, 2002.

[17] Y. R. Ryu, S. Zhu, D. C. Look, J. M. Wrobel, H. M. Jeong, and H. W. White, “Synthesis of p-type ZnO films,” *J. Cryst. Growth*, vol. 216, no. 1–4, pp. 330–334, 2000.

[18] M. C. Carotta *et al.*, “ZnO gas sensors: a comparison between nanoparticles and nanotetrapods-based thick films,” *Sens. Actuators B Chem.*, vol. 137, no. 1, pp. 164–169, 2009.

[19] H. Nanto, H. Sokooshi, and T. Usuda, “Smell sensor using zinc oxide thin films prepared by magnetron sputtering,” in *Solid-State Sensors and Actuators, 1991. Digest of Technical Papers, TRANSDUCERS’91., 1991 International Conference on*, 1991, pp. 596–599.

[20] J.-S. Park, J. K. Jeong, H.-J. Chung, Y.-G. Mo, and H. D. Kim, “Electronic transport properties of amorphous indium-gallium-zinc oxide semiconductor upon exposure to water,” *Appl. Phys. Lett.*, vol. 92, no. 7, p. 72104, Feb. 2008.

[21] J. K. Jeong, H. W. Yang, J. H. Jeong, Y.-G. Mo, and H. D. Kim, “Origin of threshold voltage instability in indium-gallium-zinc oxide thin film transistors,” *Appl. Phys. Lett.*, vol. 93, no. 12, p. 123508, Sep. 2008.

[22] Y.-C. Chen *et al.*, “Bias-induced oxygen adsorption in zinc tin oxide thin film transistors under dynamic stress,” *Appl. Phys. Lett.*, vol. 96, no. 26, p. 262104, Jun. 2010.

[23] D. C. Look, D. C. Reynolds, J. W. Hemsky, R. L. Jones, and J. R. Sizelove, “Production and annealing of electron irradiation damage in ZnO,” *Appl. Phys. Lett.*, vol. 75, no. 6, pp. 811–813, 1999.

[24] F. Tuomisto, K. Saarinen, D. C. Look, and G. C. Farlow, "Introduction and recovery of point defects in electron-irradiated ZnO," *Phys. Rev. B*, vol. 72, no. 8, p. 85206, 2005.

[25] D. C. Look, J. W. Hemsky, and J. R. Sizelove, "Residual native shallow donor in ZnO," *Phys. Rev. Lett.*, vol. 82, no. 12, p. 2552, 1999.

[26] C. Coskun, D. C. Look, G. C. Farlow, and J. R. Sizelove, "Radiation hardness of ZnO at low temperatures," *Semicond. Sci. Technol.*, vol. 19, no. 6, p. 752, 2004.

[27] W.-K. Hong *et al.*, "Tuning of the Electronic Characteristics of ZnO Nanowire Field Effect Transistors by Proton Irradiation," *ACS Nano*, vol. 4, no. 2, pp. 811–818, Feb. 2010.

[28] G. Jo, W. K. Hong, M. Choe, W. Park, Y. H. Kahng, and T. Lee, "Proton Irradiation-Induced Electrostatic Modulation in ZnO Nanowire Field-Effect Transistors With Bilayer Gate Dielectric," *IEEE Trans. Nanotechnol.*, vol. 11, no. 5, pp. 918–923, Sep. 2012.

[29] M. Choe *et al.*, "UV photoconductivity characteristics of ZnO nanowire field effect transistor treated by proton irradiation," *Thin Solid Films*, vol. 520, no. 9, pp. 3624–3628, Feb. 2012.

[30] J. I. Ramirez, Y. V. Li, H. Basantani, and T. N. Jackson, "Effects of gamma-ray irradiation and electrical stress on ZnO thin film transistors," in *71st Device Research Conference*, 2013, pp. 171–172.

[31] J. I. Ramirez *et al.*, "Radiation-Hard ZnO Thin Film Transistors," *IEEE Trans. Nucl. Sci.*, vol. 62, no. 3, pp. 1399–1404, Jun. 2015.

Chapter 2
Theoretical background

2.1 Zinc Oxide Semiconductor

2.1.1 Crystal Structure

ZnO is a group II-VI compound belongs to C_{6v}^4 or P63m space group and commonly occurs in wurtzite, zinc blende, and rock salt crystal structures as shown in figure 2.1-1 [1]. As a group II-VI semiconductor compound, ZnO is thermodynamically stable at ambient conditions in wurtzite structure.The zinc blende structure can be obtained when the ZnO is grown on the cubic substrate. The high-pressure growing conditions stabilize the rock salt crystal structure in ZnO [2]–[4].

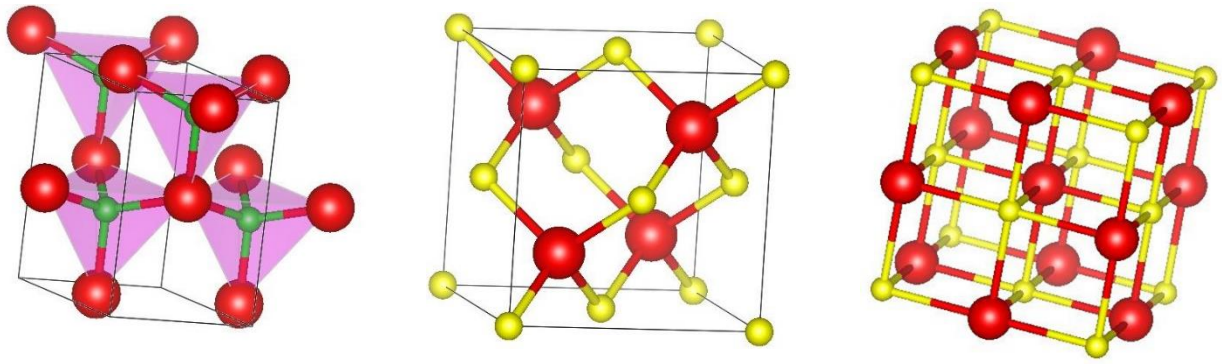

(a) (b) (c)

Figure 2.1-1: Schematics of the crystal structures of ZnO; (a) Wurtzite, (b) Zinc-blende, and (c) Rock-salt.

The metastable zinc blende structure of ZnO can be obtained by heteroepitaxial growth on cubic substrates such as ZnS, GaAs/ZnS, and Pt/Ti/SiO_2/Si [5]–[7]. The zinc blende structure belongs to the space group $F\bar{4}3m$ and constructed by two interpenertating face centered cubic

(fcc) sublattices shifted along the body diagonal by one quarter of the body diagonal. There are four atoms in unit cell, each atom is tetrahelrally coordinated with four atoms of other type, and vice versa. Since, both wurtzite and zinc blende structures posses tetrahedral coordination, the four nearest neighbours and 12 next nearest neughours share same bond length between atoms in both structures. The main deviation of these two structures is the stacking sequency of closed-packed diatomic planes. The zinc blende structure contains Zn and O atoms in closed packed stacking sequency *AaBbCcAaBbCs*.. along <111> direction along (111) plane. In addition that, the phase transistion of wurtzite to rocksalt (NaCl) structure occures at high pressure near 10 GPa. Futher, it has been suggested that phase transitions of sixfold coordinated cubic (NaCl) to eightfold coordinated cubic (CsCl) is attained at sufficiently high pressure conditions.

The ZnO wurtzite structure contains a hexagonal unit cell with lattice parameters, a= 3.2496 Å and c= 5.2042 Å to have a relation to c/a= 1.6018 [8]. The ZnO crystal shows deviation from the ideal wurtzite structure (c/a= 1.633).This crystal structure is composed of two interpenetrating hexagonal close-packed (hcp) sublattices, each for each type of atoms which are separated with respect to each other by parameter, u= 0.382 along the c-axis [9]. The u parameter is defined as the bond length between Zn and O atom along the c-axis in units c. Each sublattice contains four atoms per unit cell and each Zn atom tetrahedrally surrounded by four O atoms and visa verse. This tetrahedral coordination is typically generated with sp^3 covalent bonding between Zn and O atom. However, ZnO shows substantial ionic character with ionicity of 39%, which makes ZnO treated as an ionic oxide [10]. Moreover, the tetrahedral sublattice causes for noncentral symmetry in ZnO structure. The combination of non-central symmetry and the large electromechanical coupling result in large piezoelectric and pyroelectric properties of ZnO.The ZnO structure contains alternating bi-atomic closed packed planes with stacking sequence *AaBbAa*

along the *c*-axis. The positively charged Zn-(0001) Surface and negatively charged O-$(000\bar{1})$ Surface results in dipole moment and hence, a large spontaneous polarization of -0.05 C m^{-2} in ZnO [11], [12]. The polar surfaces maintain the stability of the structure by massive surface reconstructions. However, ZnO ± (0001) differentiated from other polar surfaces by exhibiting atomically flat and stable nature without reconstructions. The other two mostly observed facets of ZnO are $\{2\bar{1}\bar{1}0\}$ and $\{01\bar{1}0\}$, which are nonpolar surfaces having lower energy than $\{0001\}$ facet [13], [14]. The polar faces exhibit different chemical and physical properties, while the O-terminated face contains slightly different electronic structure compared to other three faces [15]. The non-polar $(11\bar{2}0)$ surface is less stable and posses a higher level of surface roughness, while polar surface and the $(10\bar{1}0)$ The surface is stable. Among the most commonly observed planes in ZnO, the (0001) plane posses the highest surface energy. Hence, ZnO structure shows highest growth rate along c-axis and the minimum surface area of the (0001) plane.

2.1.2 Electronic Band Structure

The electronic band structure of wurtzite ZnO has been widely investigated by Local Density Approximation (LDA) [16]–[18]. However, when the *d* electrons are treated as the core electrons in LDA approach, the calculated lattice constants were underestimated the experimental value. Even if the *d* electrons are appropriately taken into account in LDA approach, the estimated value for band gap energy for wurtzite ZnO has underestimated the experimental value. The LDA approach underestimated the band gap to be as low as E_g=0.23 eV compared to the experimental value, E_g^{exp}= 3.37 eV. In contrast, the self-interaction corrected pseudopotentials (SIC-PP) approach has estimated results in closer agreement with the experimental value (E_g=3.77 eV) compared the values extracted from LDA [19]. The wurtzite ZnO shows a direct band gap of E_g= 3.37 eV at room temperature. The Table 2.2-1 shows the basic physical parameters of ZnO.

Table 2.1-1 Properties of ZnO wurtzite structure [20].

Property	Value
Lattice parameters at 300 K	
a	3.2495 Å
c	5.2069 Å
a/c	1.602
u	0.375
Band-gap	3.37 eV
Density	5.606 g/cm^3
Melting point	1975 ℃
Thermal conductivity	0.6, 1-1.2 W/cm K
Static dielectric constant	8.656
Exciton binding energy	60 meV

The ZnO band structure exhibits high symmetry in the hexagonal Brillouin zone. The direct interband transitions take place at the Γ point (k=0) since the minimum of the conduction band and the maximum of the valence band alined at the k=0 in the Brillouin zone as shown in figure 2.1-2.

The conduction band of ZnO is s-like while the valence band is p like state with six-fold degeneracy. As shown in band diagram 2.2-1, the bottom bands located between -8 to -9 eV correspond to 3d levels of Zn while the upper six bands correspond to 2p levels of O. The two conduction bands are strongly localized and correspond to empty Zn 3s levels. Moreover, the valence band split into three twofold sub-bands due to the spin-orbit interaction and crystal-field

effect [21]. The degenerated p state bands in valence bands are denoted as A, (Γ_7 symmetry), B(Γ_9), and C(Γ_7) as illustrated in figure 2.1-3 [22].

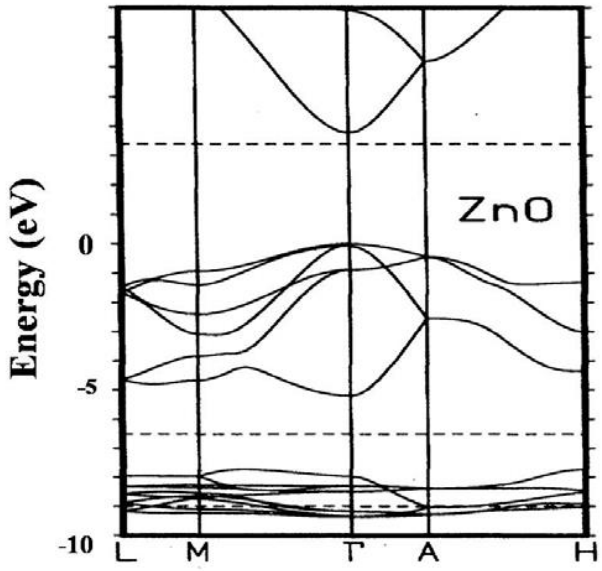

Figure 2.1-2 The bulk band structure diagram of ZnO calculated by LDA-SIC-PP [19].

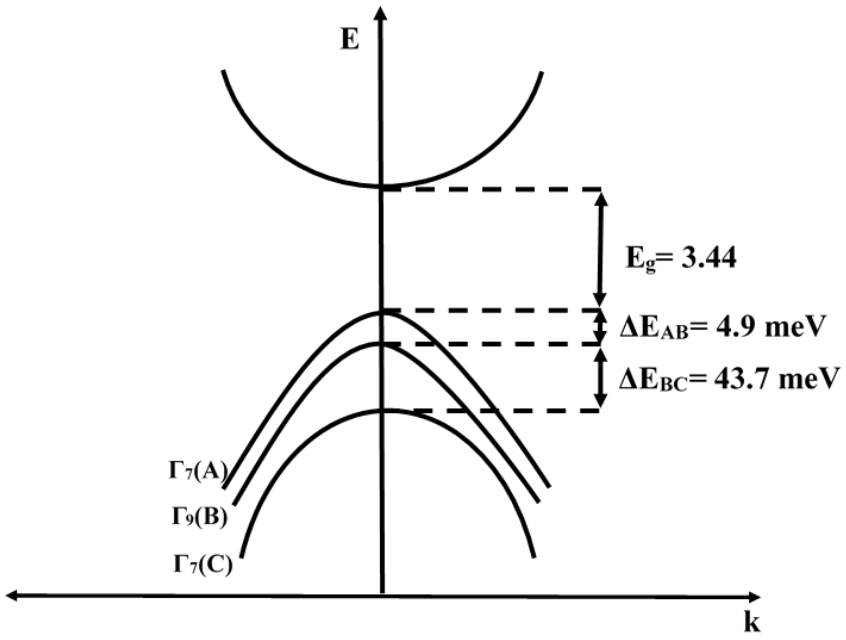

Figure 2.1-3 The band structure of hexagonal ZnO. The Splitting of valence band into three sub-bands A, B, and C due to the spin-orbit interaction and crystal field effect at 4.2 K [23].

The band gap is temperature dependent up to 300 K according to the following equation [23].

$$E_g = E_{g(T=0)} \frac{5.05\times10^{-4}\, T^2}{900-T} \qquad 2.1\text{-}1$$

The key properties of the binary II-VI oxides are given in table 2.1-2.

Table 2.1-2 Properties of binary II-VI oxides [24],[25]

	ZnO	MgO	CdO
E_g (eV)	3.37	5.4	2.2
$m_e^*(m_o)$	0.28	0.35	-
$m_{hh}^*(m_o)$	0.78	1.60 [001], 2.77 [111]	-
$m_{lh}^*(m_o)$	-	0.35 [001], 0.31 [111]	-
a ($\dot{A}$)	3.2	4.2	4.7
c ($\dot{A}$)	5.2	-	-
Stable crystal structure	Wurtzite	Rocksalt	Rocksalt

Table 2.1-3 Parameters of the alloy $Zn_{(1-x)}Mg_xO$ and $Zn_{(1-y)}Cd_yO$ [26],[27],[28],[29]

Parameter	$Zn_{(1-x)}Mg_xO$	$Zn_{(1-y)}Cd_yO$
Band gap (eV)	3.37 – 4	2.9 – 3.37
Maximum alloy incorporation	43%	70%
a-axis length expansion ($\dot{A}$)	3.250+0.036x	$3.252+0.143y - 0.147y^2$
c-axis length expansion ($\dot{A}$)	3.34 – 0.063x	$5.204+ 0.956y - 5.42y^2$

Band gap engineering is a crucial process in a semiconductor in reference to optoelectronic device applications. The alloying process allows a tailoring of the band gap of a semiconductor

material, whereby the wavelength of the exciton emission could be fine-tuned. The energy band gap of ZnO can be increased or decreased by alloying with Mg and Cd, respectively. The important parameters of the alloy ZnO, $Zn_{(1-x)}Mg_xO$ and $Zn_{(1-y)}Cd_yO$ are listed in table 2.1-3.

2.1.3 Optical Properties

The optical properties of ZnO depend on the intrinsic and extrinsic properties of the material. Typically, intrinsic transitions take place between free electrons in the conduction band and the holes in the valance band, including excitonic transitions due to Coulomb interactions. The excitonic recombinations can be categorized into free excitons which have energy slightly less than band gap and bound excitons. Bound excitons define as excitons bound to shallow donor recombination with a hole and free electron recombination with the deep acceptor [23]. The extrinsic optical properties accompanied with impurities introduced into ZnO during the growth and preparations. These impurities create defect levels with discrete energies in the band gap. The optical properties of ZnO heavily rely on the transition which occurs between band- defect levels, and inter-defect level transitions. The band to band transitions in ZnO generates UV emission (~3.75 eV) which makes ZnO is an ideal candidate for UV sensing devices. Moreover, the higher exciton binding energy well above the room temperature thermal energy (25 meV) facilitates the possibility of excitonic recombination even at room temperature. Therefore, efficient excitonic emission can be seen in ZnO at room temperature and above which makes ZnO a suitable material for exciton related optoelectronic applications. The table 2.1-4 shows the comparison of exciton binding energy for wide bandgap semiconductor materials.

Table 2.1-4 Exciton binding energies for wide bandgap semiconductors [30].

Material	Exciton binding energy (meV)
ZnO	60
GaN	21
ZnS	39
ZnSe	20

The extrinsic optical properties of ZnO rely on the type of impurities and native defects. The native point defects and impurities create defect states with discrete energy in the bandgap of ZnO. The electron-hole recombination associated with these defect levels emit visible luminescence observed in photoluminescence analysis of ZnO. A wider visible spectrum of ZnO indicates a larger number of transitions occurred with little differences between each transition. It has been widely accepted that the visible luminescence occurs due to the transitions related to oxygen vacancies in ZnO. The three types of oxygen vacancies in ZnO as native defects create three different energy states and show deep and shallow donor nature. The blue, green, and yellow luminescences are attributed to the mechanisms of delocalized electron recombination with doubly ionized oxygen vacancy (V_O^{++}), electron transition from singly ionized oxygen vacancy (V_O^{+}) to valance band, and electron transition from neutral oxygen vacancy (V_O^{*}) to valance band, respectively [31]–[33]. However, other authers have suggested that green luminesence occurred due to transition from near conduction band to deep oxygen antisites (O_{Zn}) [34]. Annealing of ZnO under oxygen rich conditions would modify the oxygen vacancy concentration in the material. Therefore, the oxygen annealing should produce a significant change in visible luminesence in ZnO. However, contravertial results have been reported after the oxygen annealing

as some authers observed enhancement in visible PL spectra and reduction in UV peak in PL analysis [35], [36].

2.1.4 Mechanical Properties

The mechanical properties of a material primarily identified with the parameters such as hardness, piezoelectric constant, Young's and Bulk moduli. The mechanical properties of a semiconductor material need to take into account when device designing and material processing for different applications. Table 2.1-5 shows an overview of experimental and theoretical parameters to describe the mechanical properties of ZnO.

Table 2.1-5 Experimental and theoretical values of mechanical properties of ZnO

Parameter	Experimental	Theoretical
Young's modulus, *E* (GPa)	111.2± 4.7 [37]	
Bulk modulus, *B* (GPa)	142.4 [38]	156.8 [39]
Hardness, *H* (GPa)	5.0 ± 0.1 [37]	
C_{11} (GPa)	207 [40]	209 [41]
C_{12} (GPa)	121.1 [37]	127 [42]
C_{13} (GPa)	105.1 [37]	105 [42]
C_{33} (GPa)	210.9 [37]	246 [42]
C_{44} (GPa)	42.47 [37]	56 [42]
Spontaneous polarization (C/m^2)		-0.057 [43]
e_{33}	0.96 [44]	1.19 [42]
e_{31}	-0.62 [44]	-0.55 [42]
e_{15}	-0.37 [44]	-0.46 [42]

$\frac{dB}{dP}$ 3.54 [38] 3.6 [39]

There are five independent elastic constants in hexagonal structures, C_{11}, C_{12}, C_{13}, C_{33}, and C_{44}. The C_{11} and C_{33} are corresponding to longitudinal modes along [1000] and [0001] directions, respectively. The C_{44} and $C_{66}= (C_{11}- C_{12})/2$ can be determined from the sound velocity of transverse modes propagating along [0001] and [1000] directions, respectively. The C_{13} can be obtained by combining other four moduli in the velocity of modes propagate in [0011] direction. The Bulk modulus (B) can be calculated as follows [45];

$$B = \frac{(C_{11}-C_{12})C_{33}-2C_{13}^2}{C_{11}+C_{12}-2C_{33}-4C_{13}} \quad \text{2.1-2}$$

The wurtzite ZnO has the negligible difference between the shear velocities propagating along [001] and [100] directions. Therefore, it is reasonable to apply isotropic approximation to ZnO to determine Young's modulus (E) as follows,

$$E = 3B(1-2\nu) \quad \text{2.1-3}$$

where ν is the Poisson ratio $\nu = \frac{C_{13}}{(C_{11}+C_{12})}$

The elastic constant can be determined by ultrasonic measurements for compound materials in the single-crystalline state. Moreover, Brillouin scattering technique which uses the interaction of light with thermal excitation in a material is also utilized to obtain elastic constants. x-ray based methods such as energy-dispersive x-ray spectroscopy (EDS), angular-dispersive x-ray diffraction (ADX), and x-ray absorption spectroscopy (XAS) can be used to determine the pressure dependence of lattice parameters. And then, under the assumption of linear dependence

of the bulk modulus on pressure, Brich-Murnaghan equation of state would deduce the bulk modulus [46].

$$V = V_0 \left(1 + \frac{B'P}{B}\right)^{1/B'} \quad \text{2.1-4}$$

where V_0 is the unit volume at ambient pressure and B' is the derivative of B with respect to pressure. Besides the experimental techniques, theoretical methods based on density-functional theory within the LDA, plane-wave expansion pseudopotentials or LMTO employed to determine the mechanical properties of ZnO.

Among other tetrahedrally bonded semiconductors, it is claimed that ZnO has a piezoelectric tensor greater or at least comparable to that of GaN and AlN [47]. This property of ZnO makes it is an important material for device applications which require a larger electromechanical coupling. The piezoelectric tensor contains three independent components in the wurtzite phase and one in zinc-blende phase. Two components in wurtzite phase measure the polarization along the c-axis by uniform strain either along the c-axis or basal plane when no electric field is present. The piezoelectric polarization along c-axis can be represented as follows [11];

$$P_z^{piezo} = e_{33}\varepsilon_z + e_{31}\varepsilon_\perp \quad \text{2.1-5}$$

where ε_z and $\varepsilon_\perp$ are the strain along the c-axis and the basal plane, respectievly. The e_{33} and e_{31} are the piezoelectric componenets. The sign of the piezoelectric tensor is fixed as the direction along the c-axis from cation to anion to be positive. The wurtzite ZnO shows low symmtry in the crystal structure, resulting a spontaneous polarization along c-aixs. The spontaneous polarization can be experimentally determined by studying the two-dimentinal electron gas and the red shift of transitions in quatum well albeit inderictrly [48]. The theoritical approach to determine the

spontaneous polarizations is the comparison of polarization of low-symmetric (wurtzite) crystal with highly symmetric (zinc-blende) crystal of the same material.

ZnO is relatively a soft material with hardness (*H*) is approximately 5 GPa at a plastic penetration depth of 300 nm [37]. Therefore, it is an important material property in device designing and processing. Nanoindentation is a widely used method to determine the hardness of ZnO in a range of size scales and temperatures. The hardness measurements are usually employed by pyramid-shaped diamond tip indented on (0001) surface of the crystal. The insight into the hardness and the pressure-induced phase transformation of the semiconductor material can be extracted by the depth-sensing indentation measurements.

In the case of ZnO, the experimental and theoretical values are in good agreement with each other for mechanical properties. However, the precision of the determined values is based on the quality of the crystals and the theoretical approximations.

2.2 Optical Characterizations

2.2.1 Raman Spectroscopy

1. Introduction to Micro-Raman Spectroscopy

Raman is a widely used material characterization method in semiconductor research area due to its nondestructive and simple sample preparation nature. Raman spectroscopy is based on inelastic scattering of monochromatic light of elementary excitations generated or annihilated by lattice vibration (phonons). Therefore, Raman spectroscopy provides information about sample lattice dynamics which could reveal the chemical composition, crystal quality, and crystal orientation. Apart from that, Raman spectroscopy could give information on electrical and magnetic properties of the sample with additional measurements.

Typically, molecular vibrational transitions are observed by IR and Raman spectrum. Generally, Raman spectra are measured in UV-visible region while IR spectra collected in IR region. When laser beam incident on the sample, it produces two types of scattering, elastic Rayleigh scattering which has the same frequency as incident photon and inelastic scattering (Stoke and ani-Stoke Raman) caused by generation or annihilation of elementary excitation [49]. Raman shift is measured with the frequency difference between inelastically scattered light and the incident photon [1], [50], [51]. Therefore, the Raman scattering is denoted as $\omega_o \pm \omega_m$ [49]. Positive Raman shift occurs in Stoke Raman scattering and negative Raman shift in anti-Stoke. In figure 2.3-1, the schematic diagram of excitation energy states is illustrated the Rayleigh and Raman scattering processes.

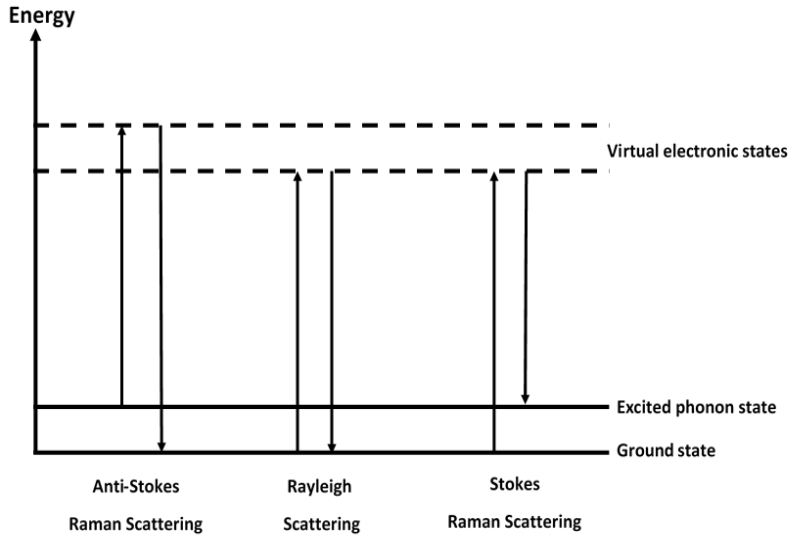

Figure 2.2-1: Schematic energy diagram of transitions corresponding to Rayleigh and Raman scattering.

The frequency of the incident photon is much higher than the elementary excitation frequencies. Therefore, Raman shift is very small. Since there are only a few phonons are thermally

excited at room temperature, stokes lines are dominating over anti-stokes lines in room temperature Raman spectroscopy [1].

In classical theory, Raman scattering is explained as the electric field (E) fluctuation with time (t) as showed below,

$$E = E_0 \cos(2\pi\nu_0 t) \qquad 2.2\text{-}1$$

where E_0 is the vibration amplitude and ν_0 is the frequency of the incident laser beam. In order to explain the Raman scattering, a simple diatomic molecule was chosen. The dipole moment (P) produced by the incident laser can be expressed as below,

$$P = \alpha_0 E_0 \cos 2\pi\nu_0 t + \frac{1}{2}\left(\frac{\partial\alpha}{\partial q}\right)_0 q_0 E_0[\cos\{2\pi(\nu_0 + \nu_m)t\} + \cos\{2\pi(\nu_0 - \nu_m)t\}] \qquad 2.2\text{-}2$$

where α_0 is the polarizability at the equilibrium position and $\left(\frac{\partial\alpha}{\partial q}\right)_0$ is the rate of change of polarizability with respect to the nuclear displacement ($q = q_0 \cos 2\pi\nu_m t$). The second term denotes the Raman scattering with $(\nu_0 + \nu_m)$ anti-stokes and $(\nu_0 - \nu_m)$ stokes frequencies while first term represents Rayleigh scattering according to the classical theory. To be Raman active, $\left(\frac{\partial\alpha}{\partial q}\right)_0$ should not be zero.

2. Selection Rules for Raman Spectroscopy

The selection rules must be applied to the normal vibration to determine whether the vibration is Raman active or not. Based on quantum mechanics, a vibration is Raman active if the polarizability is changed during the vibration. The size, shape, and orientation of the molecule tend to distort when molecules are exposed to an electric field induced by the laser beam due to charge separation in the molecule and created dipole moment. This dipole moment can be expressed in matrix form as,

$$\begin{bmatrix} P_x \\ P_y \\ P_z \end{bmatrix} = \begin{bmatrix} \alpha_{xx} & \alpha_{xy} & \alpha_{xz} \\ \alpha_{yx} & \alpha_{yy} & \alpha_{yz} \\ \alpha_{zx} & \alpha_{zy} & \alpha_{zz} \end{bmatrix} \begin{bmatrix} E_x \\ E_y \\ E_z \end{bmatrix} \quad \text{2.2-3}$$

The matrix contains polarizability components is called polarizability tensor. If one of these polarizability components is changed during the vibration, the vibration would be Raman active [49]. Since this simple normal mode approach not suitable for complex molecules, group theory has introduced selection rules for Raman spectrum by integrals.

$$[\alpha_{xx}]_{\nu'\nu''} = \int \psi^*_{\nu'}(Q_a)\alpha_{xx}\psi_{\nu''}(Q_a)dQ_a$$

$$[\alpha_{yy}]_{\nu'\nu''} = \int \psi^*_{\nu'}(Q_a)\alpha_{yy}\psi_{\nu''}(Q_a)dQ_a$$

$$[\alpha_{zz}]_{\nu'\nu''} = \int \psi^*_{\nu'}(Q_a)\alpha_{zz}\psi_{\nu''}(Q_a)dQ_a \quad \text{2.2-4}$$

$$[\alpha_{xy}]_{\nu'\nu''} = \int \psi^*_{\nu'}(Q_a)\alpha_{xy}\psi_{\nu''}(Q_a)dQ_a$$

$$[\alpha_{xz}]_{\nu'\nu''} = \int \psi^*_{\nu'}(Q_a)\alpha_{xz}\psi_{\nu''}(Q_a)dQ_a$$

$$[\alpha_{yz}]_{\nu'\nu''} = \int \psi^*_{\nu'}(Q_a)\alpha_{yz}\psi_{\nu''}(Q_a)dQ_a$$

where $\psi_{\nu'}$ and $\psi_{\nu''}$ are vibrational wavefunctions with ν' and ν'' are the vibrational quantum numbers before and after the transition. Q_a is the normal coordinate of the normal vibration. If all six integrals are zero, then the vibration is Raman inactive.

Raman Scattering by phonons shows higher efficiency in molecules with covalent bonds than ionic bonds. Since valence electrons are poorly localized in covalent crystals, large fluctuations in polarizability can be induced by the lattice vibrations. Therefore, Raman spectroscopy would give accurate results for ZnO due to its covalent and ionic nature of bonding. In ambient conditions, ZnO shows a stable hexagonal Wurtzite structure. The wurtzite structure belongs to the space group C^4_{6v} [52], [53],[54]. A unit cell contains four atoms, two from each Zn

and O. Since there are four atoms in the unit cell, 12 phonons in total exist. These 12 phonons consist of 3 acoustic modes (1LA and 2TA) and 9 optical modes (3LO and 6TO) [1]. Due to the conservation of momentum rule in light scattering, first-order Raman scattering is caused by phonon with k~0 (Γ point). By group theory, eight possible phonon modes are predicted at Γ point, $2A_1+2B_1+2E_1+2E_2$ [50]. The A and B modes are one-dimensional irreducible representations, and E modes are two-dimensional representations. Among them, one of A_1 and one of the E_1 modes are acoustic modes which show zero phonon curves at Γ point. Therefore, rest of the 6 phonon modes are optical, $A_1+2B_1+E_1+2E_2$ [48], [51], [55]. The B_1 mode is silent, and Raman inactive, and E_2 modes are only Raman active [56], [57]. The A_1 and E_1 modes are Raman active and each split into LO and TO modes with different frequencies under macroscopic electric field due to its polar nature [58]. All vibrational modes in wurtzite are characterized by the atomic displacement of 4 atoms in the unit cell. While atomic displacements along C-axis are responsible for A_1 and B_1 modes, E_1 and E_2 modes are produced by atomic vibrations perpendicular to the C-axis. The atomic displacements within the unit cell corresponding to each vibrational mode are given in figure 2.2-2.

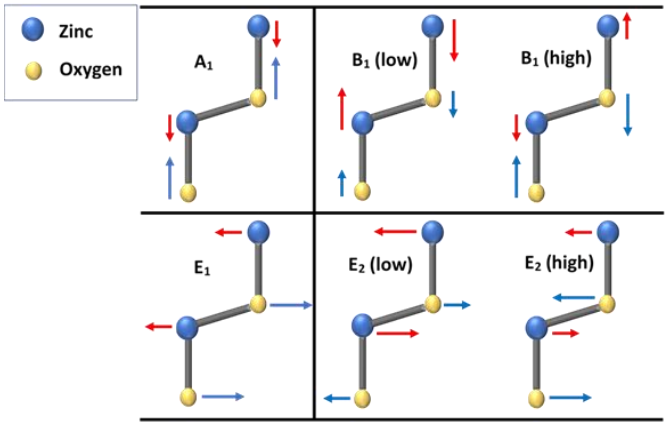

Figure 2.2-2: Schematic of atomic displacment of four atoms in the unit cell of ZnO for each vibrational mode.

The A_1 mode shows oscillating polarization due to the strong polar nature of the Zn vs. O oscillations. In contrast, B_1 mode consists of the atomic vibrations which one sub-lattice is at rest while the atoms in another sub-lattice move in opposite directions. Therefore, the net polarization induced by the lattice vibration is zero, which makes B_1 mode Raman inactive. B_1 mode shows two non-polar modes, B_1^{Low} responsible for Zn sub-lattice distortion and B_1^{High} for predominantly Oxygen distortion. The E modes are twofold degenerated due to the energy equivalence in its two-vibrational axis perpendicular to C-axis. The E_1 mode shows strong net polarization due to the oscillation of Zn sub-lattice with respect to Oxygen sub-lattice. In contrast, one sub-lattice predominantly moves in opposite directions to the neighboring atom compared to the other sub-lattice in E_2 mode. In E_2^{Low}, the vibration of heavy Zn sub-lattice dominates and vibration of lighter Oxygen sub-lattice responsible for the E_2^{High} mode. Raman shifts for ZnO wurtzite structure at room temperature for each vibrational mode are given in table 2.2-1.

Table 2.2-1: Raman shifts of ZnO for vibrational modes at room temperature [53], [54], [59]–[61].

Optical Mode	A_1(LO)	A_1(TO)	E_1(LO)	E_1(TO)	E_2^{High}	E_2^{Low}
ZnO (cm^{-1})	574-579	378-380	584-590	410-414	435-438	99-101

As mentioned in this section, it is a necessity to have non-vanishing components in Raman tensor. The Raman tensors for Raman active A_1, E_1 and E_2 modes are given below.

$$A_1(z) = \begin{pmatrix} a & 0 & 0 \\ 0 & a & 0 \\ 0 & 0 & b \end{pmatrix} \qquad E_1(x) = \begin{pmatrix} 0 & 0 & c \\ 0 & 0 & 0 \\ c & 0 & 0 \end{pmatrix} \qquad E_1(y) = \begin{pmatrix} 0 & 0 & 0 \\ 0 & 0 & c \\ 0 & c & 0 \end{pmatrix} \qquad 2.2\text{-}5$$

$$E_2^1 = \begin{pmatrix} d & 0 & 0 \\ 0 & -d & 0 \\ 0 & 0 & 0 \end{pmatrix} \qquad E_2^2 = \begin{pmatrix} 0 & d & 0 \\ d & 0 & 0 \\ 0 & 0 & 0 \end{pmatrix}$$

where a, b, and c are material constants, and x, y, z represent the phonon polarization of modes with (x, y, z) coordinate system with z-axis along the c-axis of the wurtzite structure. The observability of the modes depends on the scattering configuration as denoted by Porto notation. For example, 180^0 backscattered light from incident light beam along c-axis and detected in parallel represented as $z(x,x)\bar{z}$. The allowed modes for wurtzite structure at different scattering configurations are listed in the table 2.2-2.

Table 2.2-2: Corresponding Raman modes for different scattering configurations [51], [54].

Configuration	Modes
$x(yy)\bar{x}$	A_1(TO), E_2
$x(zz)\bar{x}$	A_1(TO)
$x(xy)\bar{x}$	E_1(TO)
$x(zy)y$	E_1(LO), E_1(TO)
$x(yy)z$	E_2
$z(xx)\bar{z}$	A_1(LO), E_2
$z(xy)\bar{z}$	E_2
$z(yy)\bar{z}$	A_1(LO), E_2

3. Crystal quality and the stress effect.

The changes in stress induced in the wurtzite crystal can be extracted from the shift in the phonon frequency. There are three types of stresses can be observed in semiconductor materials: biaxial stress, uniaxial stress, and hydrostatic stress. The biaxial and uniaxial stresses arise due to the thermal expansion mismatch between the films and the substrate, lattice mismatch, and the

distortion [61]. The lattice distortion is considered as a result of doing the material. The native defects and incorporated impurities in the material would cause the hydrostatic stress [51]. The deformation is conserved in C^4_{6v} space group, hence only the phonon shift is observed. An increment in phonon frequency ascribes to the compressive stress, while reduction indicates the tensile stress. The atomic positions are characterized by the two hexagonal lattice constants a and c Therefore, the in-plane ($\epsilon_{xx} = \epsilon_{yy}$) and a normal ($\epsilon_{zz}$) component of the strain tensor can be expressed as follows [62].

$$\epsilon_{xx} = (a - a_0)/a_0 \qquad 2.2\text{-}6$$

$$\epsilon_{zz} = (c - c_0)/c_0 \qquad 2.2\text{-}7$$

The corresponding stress tensor can be obtained via Hook's law as follows [62].

$$\sigma_{xx} = (C_{11} - C_{12})\epsilon_{xx} + C_{13}\epsilon_{zz} \qquad 2.2\text{-}8$$

$$\sigma_{zz} = 2C_{13}\epsilon_{xx} + C_{33}\epsilon_{zz} \qquad 2.2\text{-}9$$

where C_{ij} is the independent stiffness constants of the corresponding wurtzite structure. For pure biaxial stress, σ_{zz}=0 since all the forces vanishes along c-axis. Therefore, the relationship between ϵ_{xx} and ϵ_{zz} stain components derives the in-plane stress σ_{xx} by equation 2.2-8 and 2.2-9 [63].

$$\sigma_{xx} = \left[(C_{11} - C_{12}) - \frac{2C_{13}^2}{C_{33}}\right]\epsilon_{xx} \qquad 2.2\text{-}10$$

where elastic constants of ZnO are C_{11}= 206 GPa, C_{12}= 118 GPa, C_{13}= 118 GPa, and C_{33}= 211 GPa [64], [65]. The phonon frequency shift in Raman modes are associated with the stress and strain can be calculated with the following relationships.

$$\Delta\omega_\lambda = 2a_\lambda\epsilon_{xx} + b_\lambda\epsilon_{zz} \qquad 2.2\text{-}11$$

where a_λ and b_λ are the deformation potential constant in the case of stain. For stress, the deformation potential of stress, $\widetilde{a_\lambda}$ and $\widetilde{b_\lambda}$ need to be substituted instead of stain deformation potentials in equation 2.3-11. Therefore, the relationship between phonon shift in Raman spectrum and the pure biaxial stress and strain can be presented as follows,

$$\Delta\omega_\lambda = 2[a_\lambda - b_\lambda(C_{13}/C_{33})]\epsilon_{xx} \qquad 2.2\text{-}12$$

The phonon frequency shift increases as stress and strain in the wurtzite crystal increases for both (LO) and (TO) modes of A_1 and E_1 Raman modes, and E_2^{High} mode. However, E_2^{Low} mode shows opposite characterization of phonon frequency shift upon increasing stress and strain to A_1 and E_1 modes [48]. Since the E_2^{High} mode commonly yields higher signal compared to other modes in biaxial strain in c-plane, the Raman frequency shift corresponding to the E_2^{High} peak is used to evaluate the biaxial stress in c-plane. The full width at half maximum (FWHM) of E_2^{High} peak gives the information about the crystal quality.

When plasmon frequency (ω_p) reaches to the frequency of LO phonon mode (ω_{LO}), the free electrons start to couple with LO phonons via its longitudinal electric field. The LO phonon-plasmon coupled mode splits into two LPP modes: higher (LPP^+) and lower (LPP^-) modes. If the plasmon is in over damped condition; $\omega_p < \gamma$, only the LPP^+ mode can be detected [66]. The LPP^+ mode shifts to a higher frequency and peak broadening occurs if the free carrier concentration increases. Therefore, the free carrier concentration can be determined by the Raman spectra analysis. If the damping is negligible, the frequency of LPP^+ and LPP^- modes can be calculated as follows.

$$\omega_{LPP}^{\pm} = \frac{\omega_{LO}^2 - \omega_p^2}{2} \pm \left[\left(\frac{\omega_{LO}^2 + \omega_p^2}{2}\right)^2 - \omega_p^2\omega_{TO}^2\right]^{1/2} \qquad 2.2\text{-}13$$

where ω_p is the plasmon frequency, ω_{LO} and ω_{TO} are the frequencies of LO and TO modes, respectively. The ω_{LO} and ω_{TO} values can be extracted from Raman spectra as 574 cm^{-1} and 378 cm^{-1}, respectively [66]. When the free carrier concentration is higher than 10^{18} cm^{-3}, it is expected to obtain a plasmon dominance in LPP mode and symmetry in shape. Therefore, the Gaussian fit to the A_1(LO) peak could be useful to extract LPP mode frequency [67]. Hence, the plasmon frequency (ω_p) can be calculated by rearranging the equation 2.2-13 and substituting the extracted values from Raman spectra. After that, the free carrier concentration (n) can be obtained by using the following equation.

$$\omega_p = \sqrt{\frac{4\pi n e^2}{\varepsilon_\infty m^*}} \qquad 2.2\text{-}14$$

where m^* is the effective mass of free carrier, and it is determined as $0.23m_e$ for ZnO [68]. The ε_∞ is the high frequency optical dielectric constant for ZnO; 3.68 [69]. Moreover, the free carrier mobility along the z-axis can be obtained data aquired from A_1(LO) with the relationship given below.

$$\gamma = \frac{e}{m^* \mu} \qquad 2.2\text{-}15$$

where γ is the damping constant. The ZnO lattice stress induced by the proton radiation calculated by Raman spectroscopic analysis is reported in chapter 6.

2.2.2 Photoluminescence (PL)

1. Introduction to Photoluminescence

Photoluminescence is a nondestructive technique to detect certain impurities in semiconductor materials [70]. The method relies on the creation of electron-hole pairs (EHPs) by the incident laser beam on the sample and detection of emitted photons of subsequent radiative

recombinations. The photoluminesce is suited as a precise method for impurity level identification due to its higher energy resolution. The intensity of the PL spectra is proportional to the impurity concentration. However, the accuracy of impurity concentration detection is low due to the non-radiative recombinations through deep level defects and surface recombination [71]. The photoluminescence technique shows higher sensitivity to semiconductor materials with high internal efficiency. Internal efficiency is higher when the optically generated EHPs recombine radiatively. Semiconductor materials with direct band gap show significant internal efficiency compared to indirect band gap. Because most of the recombinations in indirect bandgap materials occur via Shockley-Read-Hall or Auger recombinations, which are non-radiative [72]. Therefore, low-temperature PL measurements are much desirable to obtain much information since it minimizes the thermally activated nonradiative recombinations.

2. Basics of photoluminesces

When the sample is excited with the incident laser beam with energy $h\nu > E_g$, electron-hole pairs (EHPs) are generated and then recombine via several mechanisms. If the recombination process is radiative, then photons are emitted, and the PL intensity for the particular recombination can be obtained. The electron eigenvalues of excited EHP is given by the Schrodinger equation as follows.

$$\left(-\frac{\hbar^2}{2m_e^*}\nabla e^2 - \frac{\hbar^2}{2m_h^*}\nabla h^2 - \frac{e^2}{\varepsilon r_{eh}}\right)\psi = E\psi \qquad 2.2\text{-}16$$

where $\hbar = {}^{h}/_{2\pi}$ and h is the Planck's constant, m_e^* and m_h^* are effective masses of electron and hole, respectively. The $\frac{e^2}{\varepsilon r_{eh}}$ is the modified coulombic electron-hole intercation for the medium with dielectric constant ε and r_{eh} is the distance between electron and hole. The solution for the equation applied to Bloch wavefuntion (ψ) is given below.

$$E_n = -\frac{\mu e^2}{2(n\varepsilon h)^2} \qquad 2.2\text{-}17$$

where μ is the reduced mass of EHP, ε is the dielectric constant of the material, *n* is the quantum exciton state and *e* is the charge of an electron. The bottom of the conduction band is considered as the zero energy level. The free excitons would emit light only when they are at the quantum energy states given by equation 2.2-17. The energy of the emitted photon depends on the recombinations process as shown in figure 2.2-3.

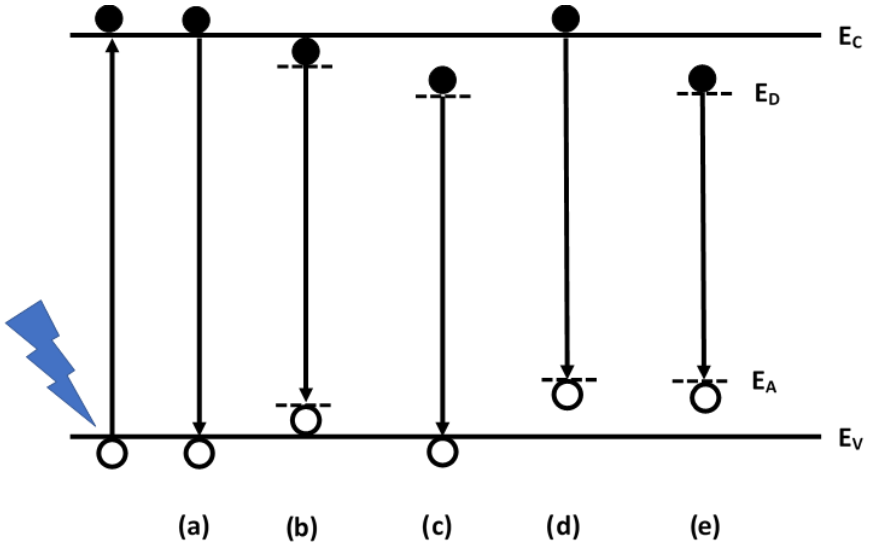

Figure 2.2-3: Radiative recombinations of electron-hole in photoluminescence process.

There are five most common PL transitions after EHP generation as illustrated in figure 2.2-3 [71]. The first type of transition is the band to band recombination as in figure 2.2-3 (a). The band to band recombination is dominant at room temperature. However, it is rarely seen in materials with smaller effective mass due to large electron orbital radii at low temperatures. The free exciton (FE) recombination is shown in figure 2.2-3(b). The energy of FE is slightly less than the band gap. Therefore, the energy of the emitted photon in direct bandgap semiconductor can be expressed as [73];

$$h\nu = E_g - E_x \qquad 2.2\text{-}18$$

where E_g is the band gap energy, and E_x is the excitonic binding energy. Since an exciton is a bound EHP, both electron and the hole move together. Therefore, the photoconductivity does not occur through bound excitons. The excitons bound to shallow donor recombination with a hole and free electron recombination with deep acceptor to form bound exciton (BE) is illustrated in figure 2.2-3(c). For less pure materials, bound exciton recombination dominates over free exciton recombination. A free electron in conduction band minimum can recombine with, and a hole in acceptor level to complete the transition showed in figure 2.2-3(d). The final type of recombination is the electron in donor level recombines with a hole in acceptor level which is known as donor-acceptor (D-A) recombination [showed in figure 2.2-3(e)]. The emitted photon energy can be expressed with the following relationship modified by the Coulombic interaction between donor and acceptor [74].

$$h\nu = E_g - (E_A + E_D) + \frac{q^2}{K_s \varepsilon_0 r} \qquad 2.2\text{-}19$$

where K_s is the dielectric constant of the semiconductor, ε_0 is the permitivity of free space, and r is the distance between donor and acceptor. If the (E_A+E_D) is low, the photon energy of the D-A recombination would be higher than the band gap energy. Such photons are reabsorbed in the sample. The FWHM of the bound exciton transition peaks are typically less than $kT/2$. However, the donor-valance band transitions are generally given wider peaks with few kT for FWHM. Hence, the FWHM values are a good measure of identifying the type of transitions since the energy for both types of recombinations are similar.

3. Photoluminescence spectra of ZnO

Typically, low-temperature photoluminescence (~ 4 K) measurements are preferable in ZnO due to two main reasons. When the temperature is sufficiently low, all the carriers are in their

ground state. Therefore, the complicated transitions from the ground state to excited states can be eliminated with low-temperature PL measurements. Moreover, the low-temperature conditions minimize the thermal line broadening and thermally activated non-radiative transitions. The thermal factor for a free electron at 4 K is about 0.18 meV while it is as high as 3.31 meV at 77 K [71]. The line broadening can cause the screening of important details in the PL spectra. It has been reported that low temperature such as 1.8 K is necessary to obtain some high-resolution PL spectra [75]. The extrinsic optical properties of ZnO is caused by native point defects and impurities. The defects states are located in band gap region as discrete energy levels. The radiative recombination of electron-hole pairs occurres between the conduction-valence bands, conduction band-defect levels, and defect levels-valence band emit visible luminances in ZnO [23]. Even though the room temperature PL spectra does not provide high-resolution spectrum, a sharp UV emission peak due to the near band edge emission and a broad visible peak can be observed for ZnO. The oxygen vacancies are widely accepted as the defect states that is responsible for visible luminescence [31]–[33]. Oxygen vacancies occur at three different levels in the band gap with discrete energies. The singly ionized oxygen vacancy (V_0^+) is singly positive chagred relative to the ZnO lattice, the doubly ionized oxygen vacancy (V_0^{++}) is doubly positive charged relative to the ZnO lattice, and the neutral oxygen vacancy (V_0^*) captures two electrons and is neutral relative to the lattice [31].

The blue, green and yellow luminescence observed in PL spectra can be attributed to the electron transition from neutral oxygen vacancy to valence band (~2.8 eV), electron transition from singly ionized oxygen vacancy to valance band (~2.5 eV), and delocalized electron near conduction band recombination with doubly ionized oxygen vacancy (~2.2 eV), respectively [31]–[33], [48]. However, some other authors have suggested that the blue luminescence generated by

radiative recombination between zinc interstials (Zn_i) and valance band and green and yellow luminescences occurred due to the transitions from near conduction band to deep oxygen anti-site (O_{Zn}) (~2.38 eV) and oxygen interstitials (O_i) (~2.28 eV), respectively [34]. The PL analyses for sol-gel derived and rf-sputtered ZnO films are presented in chapter 4.

2.3 Metal-Semiconductor Contacts

The metal-semiconductor (M-S) contact can be either rectifying or non-rectifying. The low contact resistance between metal and the semiconductor forms an ohmic contact (non-rectifying) which is necessary for source/drain contacts in MOSFETs and interconnections in IC processing. A Schottky contact (rectifying) is required for switching and rectification in circuits.

2.3.1 Schottky Contact

For an n-type semiconductor, the Schottky barrier height is defined as the potential difference between the Fermi energy level of a metal and the conduction band edge of a semiconductor. Figure 2.3-1 (a) shows the energy band diagram of an n-type semiconductor and metal in proximity.

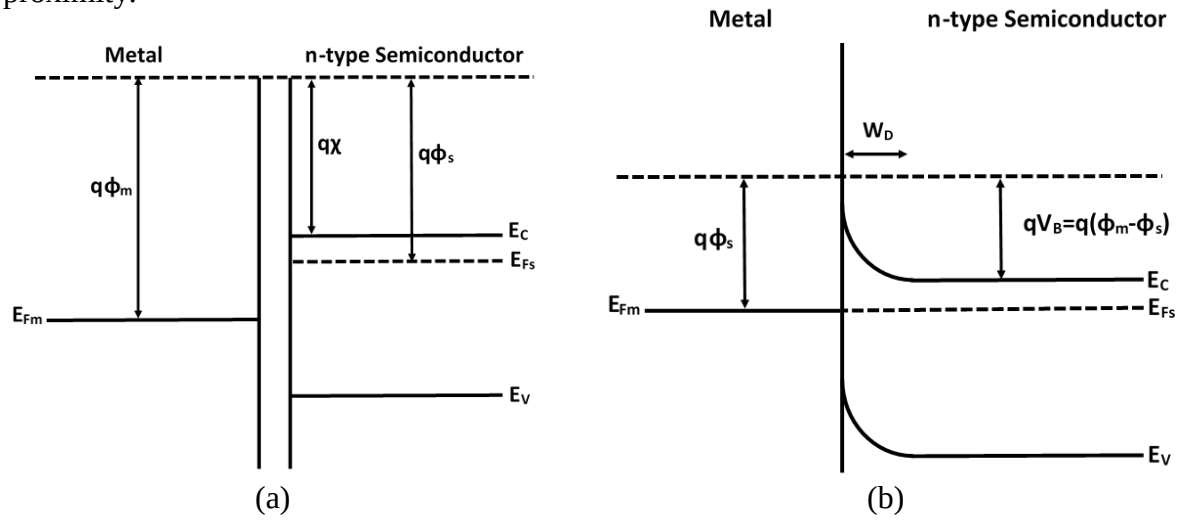

Figure 2.3-1: Energy band diagram of metal and an n-type semiconductor (a) in close proximity, and (b) in contact.

Before the semiconductor and the metal bring in to contact, the vacuum energy levels are aligned while Fermi levels are separated. The Fermi levels aligned when the metal and the semiconductor brought into contact, while conduction and valence bands bend at the M-S contact interface as shown in figure 2.3-1 (b). This band bending creates an energy barrier for free electrons that defines as the Schottky barrier. For the n-type semiconductor, the Schottky barrier height (φ_B) is defined as follows;

$$\varphi_B = \varphi_m - \chi \qquad 2.3\text{-}1$$

where φ_m is the work function of the metal and χ is the electron affinity of the semiconductor. The work function of the metal is defined as the energy required move an electron from the Fermi level to the vacuum level of a metal. The electron affinity is the energy required to move an electron from the bottom of the conduction band to the vacuum level of a semiconductor.

The alignment of Fermi level of metal and the semiconductor creates and depletion region with the width (W_D) that varies with built-in potential potential (V_B) of the Schottky barrier.

$$W_D = \sqrt{\frac{2\varepsilon_S}{qN_D}\left(V_B - \frac{kT}{q}\right)} \qquad 2.3\text{-}2$$

where ε_s is the permitivity of the semiconductor, N_D is the donor concentration of the semiconductor, q is the charge of an electron, k is the Bolzmann constant and T is the ablsoulte temperature. The built-in potential is required for electron in the conduction band to overcome the Schottky barrier and move to the metal.

$$V_B = \varphi_m - \varphi_s \qquad 2.3\text{-}3$$

where φ_s is the work function of the semiconductor. When a positive voltage is applied to the metal (forward bias), the barrier height is lowered and carrier conduction across the M-S contact increases. When a negative voltage is applied to the metal (reverse bias), the barrier height

increases and the current flow is rectified. Figure 2.3-2 shows the characteritics current-voltage (I-V) curve for both ohmic and shottky contacts.

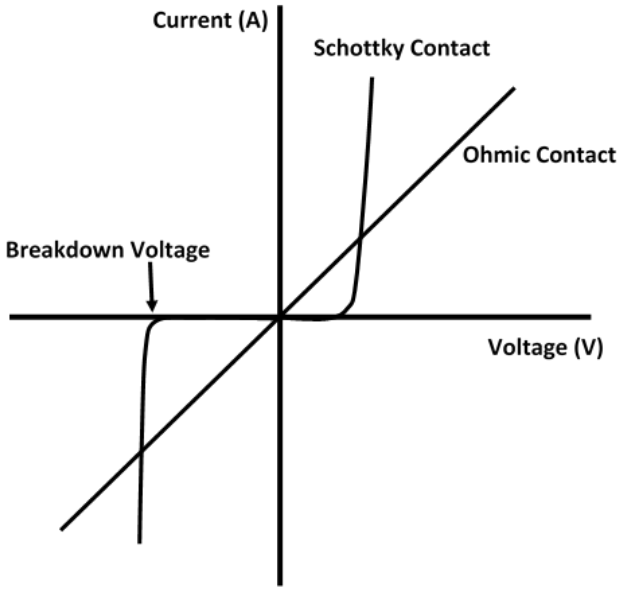

Figure 2.3-2: Current-Voltage (I-V) characteristics of Schottky and Ohmic contacts.

Table 2.3-1 showed the work function of selected metals and calculated Schottky barrier potential from equation 2.3-1. The work function of the ZnO is considered as 4.71 eV [76]. The calculated values often deviate from the experimental values since the ideal conditions are assumed in the calculation. The deviation in experimental and the estimated values can be attributed to the chemical reactions between metal and semiconductor and interfacial contamination, which change the barrier potential.

Table 2.3-1 Work function, and calculated barrier potential for selected metals on ZnO.

	Al	Ti	Ni	Au	Pt
φ_m (eV)	4.28	4.33	5.10	5.15	5.65
φ_B (eV)	-0.43	-0.38	0.39	0.44	0.94

2.3.2 Ohmic Contact

Ohmic contact has negligible barrier between the Fermi level of the metal and the conduction band of the semiconductor. An ideal ohmic contact exhibits a straight line relationship in *I-V* characteristic with low contact resistance (R_c). The R_c of a semiconductor with high doping level can be calculated as follows [77];

$$R_c = exp\left(\frac{2\sqrt{\varepsilon_s m^*}}{h}\left[\frac{\varphi_B}{\sqrt{N_D}}\right]\right) \quad \text{2.3-4}$$

where ε_s is the permitivity of the semiconductor, m^* is the effective mass of an electron, h is the Plank's constant, φ_B is the barrier potential and N_D is the donor concentration of the semiconductor. A low contact resistance compared to the bulk resistance is required to obtain low voltage drop across the metal-semiconductor junction to reduce power dissipation during the current conduction.

A semiconductor with higher doping concentration and a metal-semiconductor contact with low barrier potential can facilitate a low contact resistance. Fine control in surface variables that affect the Schottky barrier height dictates the Schottky or Ohmic nature of the contact. If the work function of the metal (φ_m) is lower than the work function of the semiconductor (φ_s), a ohmic contact can be obtained for n-type semiconductors as shown in figure 2.3-3.

The ohmic characteristics of an M-S contact can be obtained by controlling the Schottky barrier via specific processing steps to reduce the height of the Schottky barrier or width of the depletion region. The height of the Schottky barrier is a function of the work function of the metal in contact with the semiconductor. However, the width of the depletion region can be manipulated with the doping of the semiconductor. A thinner depletion region facilitates carrier tunneling through the barrier to obtain an ohmic contact. Moreover, the barrier height can be lowered with

selected metal that has a work function lower than the work function of ZnO and also with contact metal annealing by rapid thermal annealing (RTA) in N_2.

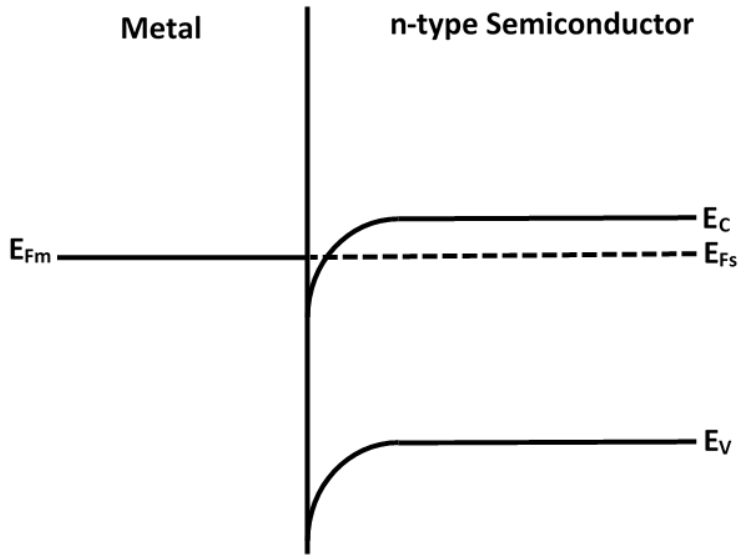

Figure 2.3-3: Energy band diagram of an ohmic contact on n-type semiconductor.

2.3.3 Transmission Line Model (TLM)

One of a most effective method of evaluating the specific contact resistivity of ohmic contacts is Transmission Line Model (TLM). The TLM technique was first proposed by Shockley as a convenient method to determine the specific contact resistivity of planer ohmic contacts[78].

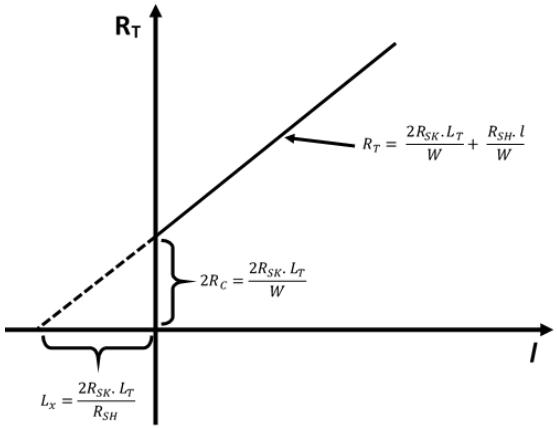

Figure 2.3-4: Plot of total contact resistance (R_T) as a function of l to obtain transfer length and contact resistance.

The experiment is to measure the total resistance (R_T) between two contact pads (d×w) separated by a distance *l* and plot as a function of *l* as shown in figure 2.3-4. The equation of the fitted linear plot for R_T vs. *l* provides an estimation for ρ_C through transfer length (L_T) extracted from the x-intercept of the plot. The R_T between two contact pads seperated by a distance *l* is given by,

$$R_T = 2R_C + \frac{R_{SH} l}{w} \qquad 2.3\text{-}5$$

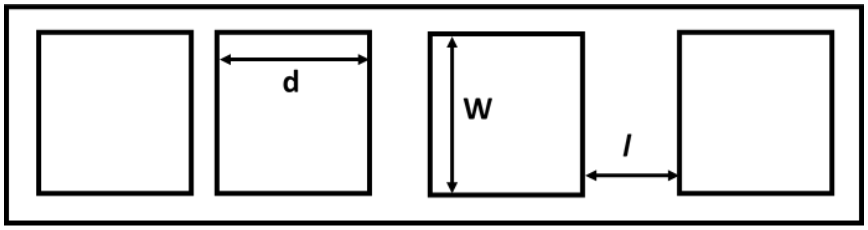

Figure 2.3-5: Top view of the linear transmission line method (LTLM) contacts.

where R_C is the contact resistance, R_{SH} is the sheet resistance of the semiconductor outside the contact region, and *w* is the width of the contact pad. The R_C has the relationship as follows;

$$R_C = \frac{R_{SK} L_T}{w} \coth\left(\frac{d}{L_T}\right) \qquad 2.3\text{-}6$$

$$\text{where } L_T = \sqrt{\frac{\rho_c}{R_{SK}}} \qquad 2.3\text{-}7$$

Therefore, when $d > 2L_T$,

$$R_T = \frac{2R_{SK} \cdot L_T}{w} + \frac{R_{SH} \cdot l}{w} \qquad 2.3\text{-}8$$

The R_{SK} is the modified sheet resistance of the semiconductor under the contact pad, *d* is the length of the contact pad. Under the assumption that the sheet resistance of the semiconductor outside the contact region (R_{SH}) is same as the sheet resistance of the semiconductor directly beneath the contact region (R_{SK}), the L_T can be deduced as following,

$$-l = L_x = 2L_T \quad \text{2.3-9}$$

Once L_T is extracted, the ρ_C can be determined from equation 2.3-7. However, the M-S contact interface modification brought by sintering during the contact deposition process enforce the $R_{SH} \neq R_{SK}$ condition. Therefore, L_T can not be extracted from the x-axis extrapoltion of the R_T *vs. l* plot. In this case, an extra experimental data called "end resistance" (R_E) need to be collected to obtain the L_T as shown in figure 2.3-6.

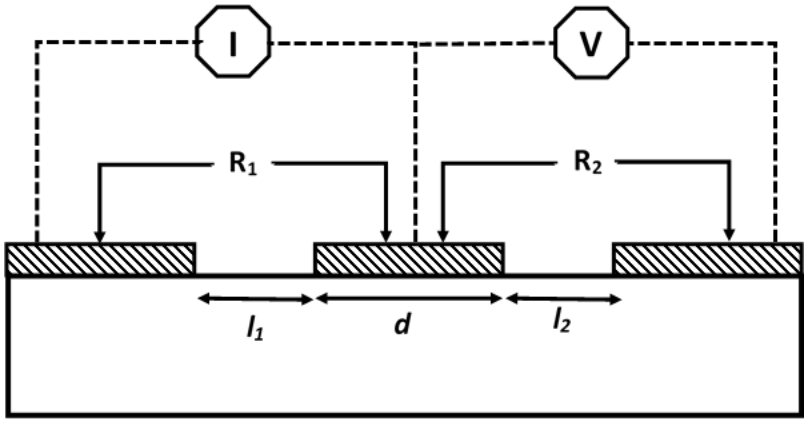

Figure 2.3-6: Experimental measurement set up to extract end resistance (R_E).

A constant current was passed between two contacts and the, potential was measured between one the contacts and an opposite outside contact pad. The R_E value calculated by simple ohms law.

$$R_E = \frac{V}{I} \quad \text{2.3-10}$$

where *V* is the potential between the contact pads and the *I* is the constant current passed between contacts. Then the L_T can be determined by using parameters extracted from the R_T *vs. l* plot and the R_E.

$$\frac{R_C}{R_E} = \cosh\left(\frac{d}{L_T}\right) \quad \text{2.3-11}$$

The relationship between TLM parameters and the R_E can be shown as follows [79];

$$R_E = \frac{\rho_c}{L_T.w} \frac{1}{\sinh\left(d/L_T\right)} \qquad 2.3\text{-}12$$

The ρ_C can be calculated accuratly from equation 2.3-12 with L_T extracted from equation 2.3-7. The LTLM measurment and data analysis performed to identify the proton irradiation effect on metal contacts of ZnO TFTs are reported in chapter 6.

2.4 Basics of Metal-Insulator-Semiconductor Field Effect Transistors

2.4.1 Metal-Insulator-Semiconductor Band Diagram

In an ideal Metal-Insulator-Semiconductor (MIS) structure, an applied external voltage to the metal accumulates charges either only at the metal-insulator interfaces or opposite charges in the semiconductor. An ideal insulator is assumed with infinite resistivity. Hence no charges are allowed within the insulator. Also, an ideal insulator-semiconductor interface without trap charges is assumed. For an ideal MIS, there is no difference between metal and semiconductor work function under a zero external applied voltage;

$$\varphi_{ms} = \varphi_m - \varphi_s = \varphi_m - \left(\chi_s + \frac{E_g}{2q} - \Psi_B\right) = 0 \qquad 2.4\text{-}1$$

where φ_m and φ_s are the work functions of the metal and the semiconductor, respectively. The χ_s is the electron affinity of the semiconductor, E_g is the band gap of the semiconductor, q is the charge of an electron and Ψ_B is the difference between Fermi energy level (E_F) and the intrinsic energy level (E_i). Figure 2.4-1 shows the band diagram of an ideal MIS structure in flat-band condition (zero applied voltage).

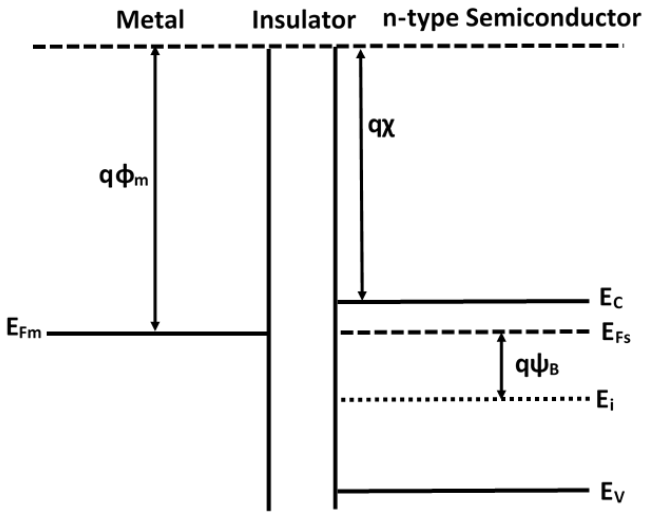

Figure 2.4-1: Band diagram of an ideal MIS structure in flat-band condition.

For n-type semiconductors, the Ψ_B can be obtain from the bulk electron concentration.

$$\Psi_B = \frac{k_B T}{q} \ln\left(\frac{N_D}{n_i}\right) \qquad 2.4\text{-}2$$

where $n \approx N_D = n_i e^{(E_i - E_F)/k_B T}$

where n_i is the intrinsic carrier concentration and N_D is the donor concentration.

An MIS structure undergoes three possible cases when an external voltage is applied: a) accumulation, b) depletion and c) inversion.

a) Accumulation

If a positive voltage is applied to the metal, the bands bend downwards with respect to the Fermi energy level allowing no current flow through the insulator as shown in figure 2.4-2 (a). Due to the charge neutrality, the positive charge at the metal interface is equalized by electrons accumulated at the insulator-semiconductor interface. This process is known as the field effect.

b) Depletion

If a negative voltage is applied to the metal, the bands bend upwards, creating a Schottky barrier at the insulator-semiconductor interface. However, the intrinsic energy level does not cross the Fermi energy level band. When the applied negative voltage increases, the Schottky barrier expands.

c) Inversion

When the applied voltage is further increased beyond Ψ_B , the E_i level crosses the E_F and creates a inversion layer. In the inversion layer, thermally generated hole concentration increases over the electron concentration. However, the inversion due to the thermally generated holes in ZnO is impossible due to the large band gap.

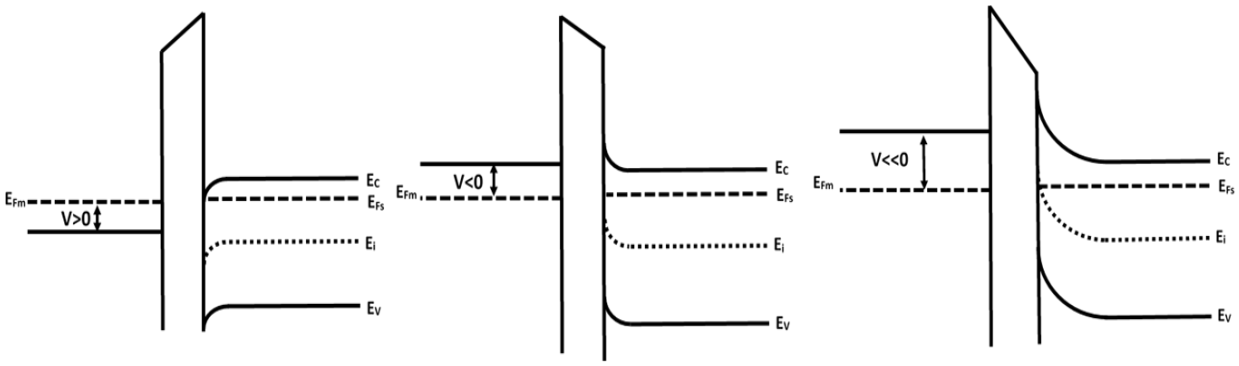

(a) (b) (c)

Figure 2.4-2: Band diagrams of ideal MIS structure with applied external voltage; (a) accumulation, (b) depletion, and (c) inversion.

2.4.2 Operation Principle of ZnO Thin Film Transistors

The operation principle of n-type, normally-on ZnO MISFET will be discussed in this section. When a positive gate voltage (V_{GS} >0V) is applied, electron accumulation occurs at the semiconductor-insulator interface to create an active channel between the source and drain as shown in figure 2.4-3 (a). For V_{DS} > 0V, an electric field will be created between source and drain

and current (I_D) will start the flow. For lower V_{DS}, the channel resistance is constant and therefore, I_D will linearly vary with V_{DS} according to the Ohm's law. With increasing $V_{DS,}$ the potential drop across the channel and the potential difference lead to expanding the depletion layer at the drain side of the channel. At a critical value of V_{DS} ($V_{DS,\,sat}$), the depletion layer width expands to the full width of the active channel, causing a pinch off as shown in figure 2.4-3 (b). Further increase in V_{DS} to $V_{DS,\,sat} + \Delta V$ shifts the pinch-off point towards the source and ΔV potential drops across the depleted region. Therefore, the potential drop across the source and the pinch-off point remains same as the $V_{DS,\,sat}$ to obtain contact I_D for higher V_{DS} values [I_D ($V_{DS} > V_{DS,\,sat}$)= $I_{D,\,sat}$].

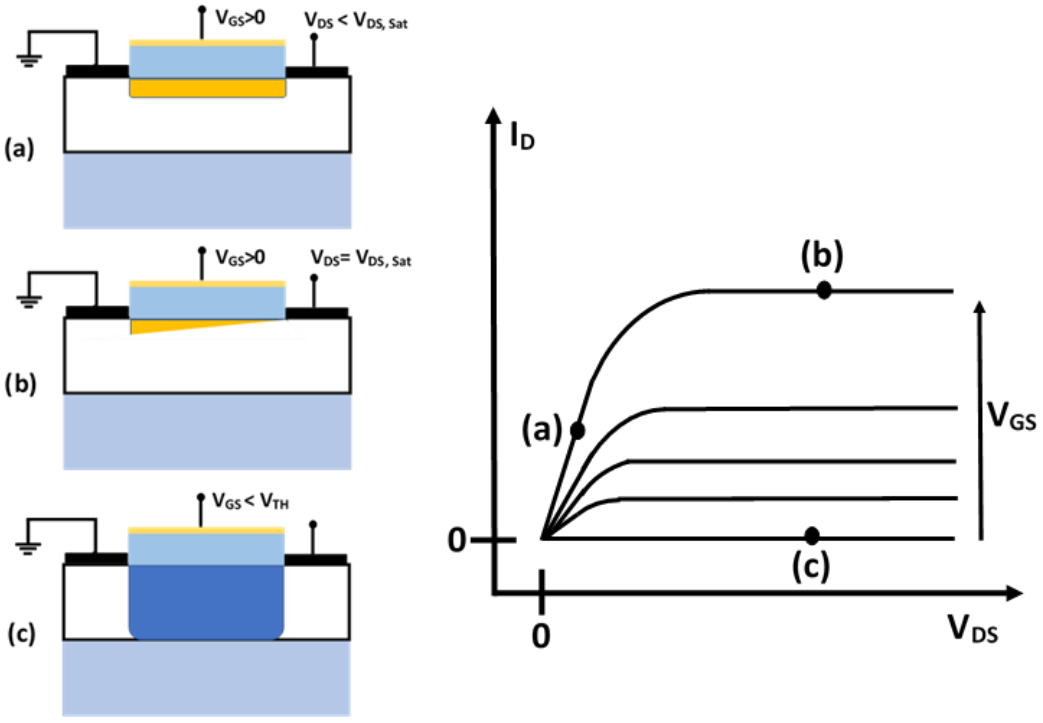

Figure 2.4-3: Operation principle and schematic output characteristics of a MISFET.

The width of the open channel or active channel can be controlled by the gate voltage (V_{GS}). If the V_{GS} is high enough to expand the depletion region to the full channel width as shown in figure 2.4-3 (c), no current will flow between source and drain (I_D) for any V_{DS} keeping the transistor off state. The critical value of V_{GS} that requires to fully deplete the channel layer is known

as the threshold voltage (V_{TH}). For $V_{GS} > V_{TH}$, the transistor is in on state and for $V_{GS} < V_{TH}$, the transistor is in off state. With increasing negative V_{GS} and constant V_{DS}, the width of the active channel decreases and the ohmic resistance of the linear region of the output characteristics increases. The pinch-off potential reaches to small V_{DS}; $V_{DS\,sat} \rightarrow 0$ for $V_{GS} \rightarrow V_{TH}$. Therefore, the ΔV of the V_{DS} drops across the active channel and I_D decreases until $V_{DS,sat} = 0$V to be $I_D = 0$.

2.4.3 Current-Voltage Characteristics

The following assumptions are made to derive the current-voltage characteristics of MISFET;

1. The direction parallel to the substrate is referred as x-direction.
2. The channel is homogeneously doped with doping concentration; N_D.
3. The size of the depletion layer is slowly changing in x-direction compared to y-direction ($\varepsilon_x \ll \varepsilon_y$).
4. The length of the gate is larger than the channel thickness, (L>> d)
5. The mobility of the electron is constant, ($v = \mu\varepsilon_x$)
6. The gate leakage current is negligible.

The drift current density can be written regarding mobile charges and their velocity.

$$j(x) = Qv(x) = -qN_D\mu\varepsilon_x = qN_D\mu\frac{\partial V}{\partial x} \qquad 2.4\text{-}3$$

Therefore, the source-drain current in the neutral part of the channel with cross-section $A = W(d - w(x))$, W is the channel width, and $w(x)$ is the depletion layer width can be given as,

$$I_D(x) = j(x)A = qN_D\mu\frac{\partial V}{\partial x}(d - w(x))W \qquad 2.4\text{-}4$$

Since inversion cannot be achieved in ZnO MISFET, an electrostatic approach need to be used to discuss the electrical characteristics of the transistors. The induced charge Q_{ind}, in the ZnO

channel is given by the insulator capacitance (C_i) and the difference between the gate voltage and the threshold voltage.

$$Q_{ind} = -C_i(V_G - V_{TH}) \quad \text{2.4-5}$$

Under the assumption of constant charge density along the channel, the source-drain current can be written as,

$$I_D = -Q_{ind} \nu W = -Q_{ind} \mu \frac{W}{L} . V_{DS} \quad \text{2.4-6}$$

where $\nu = \mu\varepsilon = \mu \frac{V_{DS}}{L}$ is the charged carrier velosity. By substituting equation 2.4-5 into equation 2.4-6,

$$I_D = \mu C_i \frac{W}{L} (V_G - V_{TH}) V_{DS} \quad \text{2.4-7}$$

The equation 2.4-7 is valid for small V_{DS} where the channel act as a linear resistor modulated by V_{GS} [80].

Since the electric field varies along the channel from source to drain, a small section of the channel (dx) and a local channel voltage (V_C) accounted in the equation 2.4-7. Hence the modified relationship of current-voltage in ZnO MISFET can be given as,

$$I_D = \mu C_i \frac{W}{dx} (V_G - V_C - V_{TH}) dV_C \quad \text{2.4-8}$$

when both sides of the equation 2.4-8 integrated from source to drain; I_D remains constant according to the Kirchhoff's second law.

$$\int_0^L I_D dx = \mu C_i W \int_0^{V_{DS}} (V_G - V_C - V_{TH}) dV_C \quad \text{2.4-9}$$

The integration results in;

$$I_D = \mu C_i \frac{W}{L} \left[(V_G - V_{TH}) V_{DS} - \frac{V_{DS}^2}{2} \right] \quad \text{2.4-10}$$

I_D increases linearly with increasing V_{DS} until V_{DS} reaches to $V_{DS,\,sat}$ where the pinch-off occurred. Further increased V_{DS} beyond the $V_{DS,\,sat}$ resulted in saturation I_D which is independent of the $V_{DS.}$

$$I_D = \mu C_i \frac{W}{L} \frac{(V_G - V_{TH})^2}{2} \quad 2.4\text{-}11$$

Equation 2.4-10 is usually applied to extract V_{TH} of MISFET by extrapolating the x-axis intercept of I_D *vs.* V_{GS} plot. Moreover, the field effect mobility can be obtained from transconductance extracted from equation 2.4-10.

$$g_m = \frac{\partial I_D}{\partial V_{GS}} = \mu C_i \frac{W}{L} V_{DS} \quad 2.4\text{-}12$$

Therefore, the field effect mobility is given by,

$$\mu_{FE} = \frac{g_m}{C_i V_{DS} (W/L)} \quad 2.4\text{-}13$$

The subthreshold swing (*SS*) can be extracted from transfer charactersitics; I_D *vs.* V_{GS}. The linear extrapolation of *log* I_D *vs.* V_{GS} in the region between V_{ON} and V_{TH} yields the subthreshold swing as follows,

$$SS = \frac{dV_{GS}}{d \log I_D} \quad 2.4\text{-}14$$

Then the interface trap density (D_{it}) can be calculated by using the equation 2.4-15.

$$D_{it} = \left(\frac{0.434.(SS)}{k_B T/q} - 1 \right) \frac{C_i}{q} \quad 2.4\text{-}15$$

where C_i is the capacitance of the dielectric layer, k_B is the Bolzmann constant, T is the temperature, and q is the charge of an electron.

The I-V data analysis for ZnO TFTs by methods mentioned above are reported in chapter 5,6, and appendix II.

2.4.4 Capacitance-Voltage Characteristics

When an oxide is used as an insulator such as SiO_2 in MIS structure, a metal-oxide-semiconductor (MOS) capacitor can be obtained. The capacitance-voltage characterization is used

to identify the behavior of trap charges in the MOS structure. The capacitance is defined as the change of charge due to the change of voltage,

$$C = \frac{dQ}{dV} \qquad 2.4\text{-}14$$

During the capacitance measurements, a small ac voltage is applied across the MOS structure. The change is the charge across the MOS generates a capacitance, $C = \frac{dQ_G}{dV_G}$. Since the voltage is applied to the gate, charge the accumulated in the gate electrode should be balanced by the charges across the MOS structure. Hence, under the assumption of no oxide charges,

$$Q_G = -(Q_S + Q_{it}) \qquad 2.4\text{-}15$$

where Q_S and Q_{it} are the charges in the semiconductor and interface trapped charges, respectively. The band diagram of the MOS capacitor is given in the figure 2.4-4.

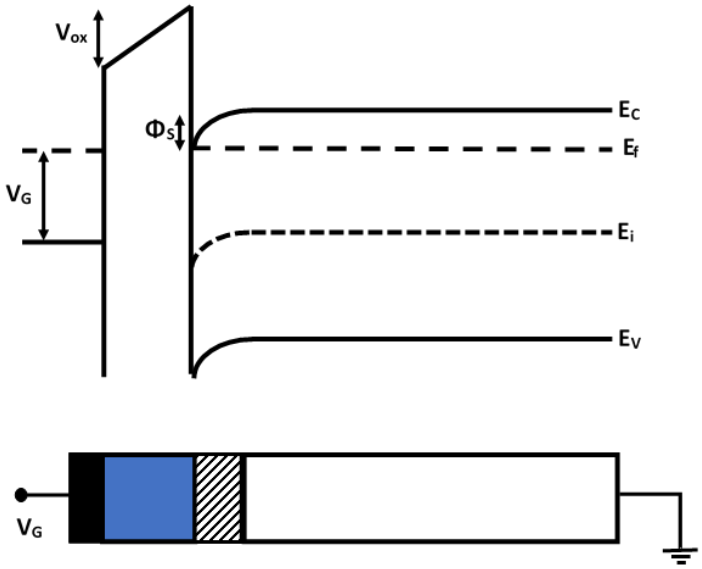

Figure 2.4-4: Schematics of potential band diagram and the cross-section of an MOS capacitor.

The applied gate voltage drop across the oxide-semiconductor structure. Therefore, $V_G = V_{FB}+V_{ox}+\varphi_S$, where V_{FB} is the flat band voltage, V_{ox} is the voltage across the oxide, and φ_S is the surface potential. By equation 2.4-14 and 2.4-15;

$$C = \frac{dQ_S + dQ_{it}}{dV_{ox} + d\emptyset_S} \quad \text{2.4-16}$$

The semiconductor charge density, Q_S consists of the hole charge density (Q_p), and electron charge density (Q_n). Therefore, the relationship in equation 2.4-16 can be written as,

$$C = \frac{1}{\frac{dV_{ox}}{dQ_S + dQ_{it}} + \frac{d\emptyset_S}{dQ_p + dQ_n + dQ_{it}}} \quad \text{2.4-17}$$

By the definition of the capacitance of as in equation 2.4-14,

$$C = \frac{1}{\frac{1}{C_{ox}} + \frac{1}{C_p + C_n + C_{it}}} \quad \text{2.4-18}$$

In undoped ZnO, the hole density is relatively low compared to electron density, resulting in negligible C_p. Hence, the equation 2.4-18 needs to be modified for ZnO as follows.

$$C = \frac{C_{ox}(C_n + C_{it})}{C_{ox} + C_n + C_{it}} \quad \text{2.4-19}$$

For a negative gate voltage, the surface is depleted, thus the electron density in the semiconductor becomes negligibly smaller. Therefore, the contribution of the free electron density to the total capacitance is negligible in a fully depleted MOS capacitor. The interface trapped charge density also contributes total capacitance across the MOS structure. When the semiconductor layer is fully depleted, the total capacitance is given by the combination of C_{ox} and C_{it} in series. For a positive gate voltage applied, free electrons accumulate in the semiconductor to increase the electron density. Hence, the C_n dominates over the C_{ox} when the MOS capacitor is in accumulation mode. The C-V measurement can be done by using high-frequency and low-frequency (quasi-static) AC signal.

The low-frequency C-V method is commonly used to determine interface trap charges in MOS structure [81]. During the low-frequency C-V measurements, the interface traps are able to respond to the low ac probe frequency. Therefore, the contribution of C_{it} is presented in the total

capacitance. The comparison of the quasi-static C-V curve with the theoretical C-V curve which is free of interface traps would give the insight into interface trap density. The high-frequency C-V measurement uses higher ac probe frequency to which the interface traps cannot respond. Therefore, the high-frequency C-V curve does not include the C_{it} contribution. The comparison between the quasi-static and high-frequency C-V curves has been a common practice to determine the interface trap density [72]. The relationship between the interface trap density (D_{it}) and high (C_{hf}) and low -frequency (C_{lf}) C-V measurements can be illustrated as follows,

$$D_{it} = \frac{C_{ox}}{q^2}\left(\frac{C_{lf}/C_{ox}}{1-C_{lf}/C_{ox}} - \frac{C_{hf}/C_{ox}}{1-C_{hf}/C_{ox}}\right) \quad \text{2.4-20}$$

The series resistance and the stray light can influence the C-V curve in quasi-static measurement. Moreover, the quasi-static method has a lower limit of D_{it} to be determined at 10^{10} cm^{-2} eV^{-1}. Also when the oxide layer thickness decreases, the oxide leakage current component dominates in the C-V curve. Therefore, the D_{it} determined in quasi-static method contains its limitations. Then, more sensitive method such as conductance method was proposed to determine D_{it} of 10^9 cm^{-2} eV^{-1} and lower [82]. The conductance method measures the equivalent parallel conductance of the MOS capacitor as a function of gate bias and the frequency. The conductance is a measure of the loss mechanism due to the interface trapping and emission of carriers. Other than that, high-frequency techniques such as Terman method [83], Gray-Brown [84] and Jenq [85] methods are used to determine the interface trap density. The C-V data analysis are reported in appendix II.

2.5 Fixed, Trapped, Mobile Oxide, and Interface Trapped Charges

In an ideal MOS structure, the flat band occurs at V_G=0. However, there are charges present within the insulator layer and at the semiconductor-insulator interface influencing a nonzero flat band voltage. These nonidealities of the MOS structure affects the threshold voltage (V_{TH}) of the

MOS transistor. Based on the type and the location of the trapped charges in the MOS structure, different effects on the V_{TH} can be observed.

2.5.1 Fixed Oxide Charges (Q_f)

Typically for the Si-SiO_2 system, positive charges are invariably seen in the insulator. The origin of these positive charges linked with the oxidation conditions such as temperature and oxidation ambient and also silicon orientation. It has been identified that majority of the fixed oxide charges are located in the proximity of the Si-SiO_2 interface and do not electrically interact with semiconductor bands [86]. It is challenging to analyze fixed oxide charges at room temperature measurements with the interference of the interface trapped charge effect. Therefore, the standard practice is to take place measurements at low temperature (450℃) which minimizes interface trap charge effect [72]. The relationship between the oxidation conditions and the Q_f is summarized in the *Deal triangle* as shown in figure 2.5-1 [87].

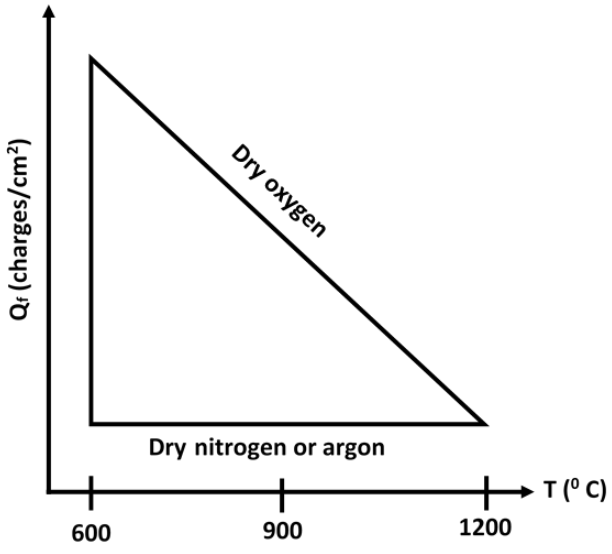

Figure 2.5-1: Schematic of the Deal triangle, which represents the dependence of Q_f on processing [86].

At higher temperature oxidation with dry oxygen yields lower Q_f. However, it is possible to obtain lower Q_f with low-temperature annealing in a nitrogen or argon ambient after the oxidation. The Q_f of a carefully grown SiO_2 is maintained in less than 10^{11} charges/cm^2.

2.5.2 Tapped Oxide Charges (Q_{ot})

The trapped oxide charges are defined as positive or negative charges induced in the insulator due to hole or electron trapped in the insulator. The origin of the Q_{ot} influenced mechanisms such as electron-hole pair production during ionizing radiation [88], avalanche injection, and Fowler-Nordheim tunneling [89]. The higher mobility in electrons compared to holes results in generated electrons to be immediately swept to the gate of the MOS structure while slow holes are trapped in the insulator [90]. Therefore, it is highly likely that Q_{ot} to be positively charged. However, unlike fixed oxide charges, Q_{ot} can be annealed out by low-temperature (< 500℃) annealing process.

2.5.3 Mobile Oxide Charges (Q_m)

The alkali metal ions such as Na^+, Li^+, K^+, and Cs^+ present in the insulator are mobile slightly above room temperature. The ionic impurities can be introduced to the insulator during the growth process and as contaminants of process chemicals. In a case of proton irradiation, H^+ possibly be contributed to the mobile oxide charge density. The electrical effect of Q_m on the MOS structure is described as follows.

When positive gate bias is applied at elevated temperatures, mobile ions drift towards the semiconductor-insulator interface. The ions located in the proximity of the interface cause the band bending and shift the V_{FB}, thereby the V_{TH} of the MOS transistor shifts. In contrast, negative gate bias attracts positive Q_m towards the gate and keeping them away from the semiconductor-insulator

interface. Hence, the influence on semiconductor bands is low, and V_{FB} shift back to its original value so does V_{TH}. Therefore, Q_m causes an electrical instability in MOS devices under bias-temperature stress. In modern device manufacturing processes, the mobile oxide charge density has controlled by meticulous cleaning in the fabrication process.

2.5.4 Interface Trapped Charges (Q_{it})

The interface trapped charges (Q_{it}) can be either positive or negative charge trapped at the semiconductor-insulator interface due to oxidation-induced defects, structural defects, ionic impurities or other types of defects induced by radiation (*e.g.,* hot electrons). The Q_{it} shows direct influence to the semiconductor band structure at the interface. Hence, Q_{it} is more electrically active than other types of defects in the MOS structure. The charges are trapped in interface states which are distributed based on energy. These trapped energy states are described by the density of state, D_{it}. The D_{it} shows a U-shaped distribution between the conduction band and the valence band energy. In equilibrium condition, the occupancy of the interface states is determined by the Fermi energy level of the semiconductor. The interface states located in the upper half of the bandgap are acceptor-like (neutral when empty, negatively charged when filled) and lower half are donor-like (neutral when filled, positively charged when empty) [91]. If a MOS structure with n-type semiconductor at flat band is considered, a considerable number of acceptor-like states are filled to yield net negative charge in the interface states.

$$Q_{i(flat\ band)} = -qD_{it}\varphi_F \qquad 2.5\text{-}1$$

where q is the magnitude of charge of an electron, and $\varphi_F = E_F - E_i = kT.\ln(N_D/n_i)$.

Also, the flat band voltage can be written as,

$$V_{FB} = \frac{Q_{i(flat\ band)}}{C_i} = \frac{qD_{it}\varphi_F}{C_i} \qquad 2.5\text{-}2$$

The additional negative charges due to Q_{it} increases the surface potential to create a wider depletion at the interface. Therefore, more positive gate voltage is required to reduce the surface potential at the semiconductor-insulator interface to obtain carrier accumulation. This phenomenon results in V_{TH} shift in positive gate bias direction for MOS transistor. The change in surface potential with gate bias due to interface state induces a change in capacitance of MOS capacitor. Therefore, the C-V curve shows a "stretche out" behavior compared to ideal MOS capacitor as shown in figure 2.5-2.

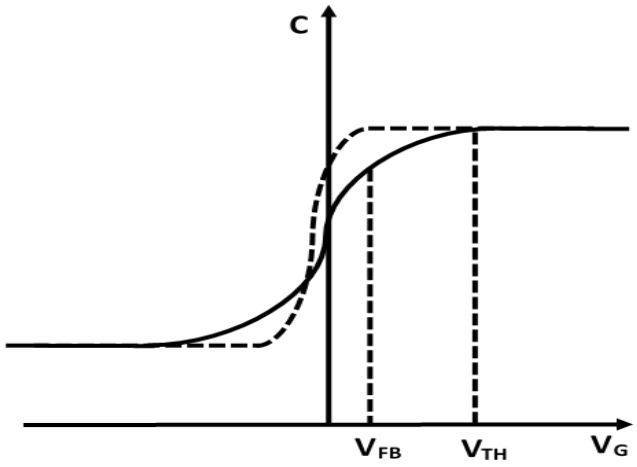

Figure 2.5-2: Schematic of C-V characteristics for MOS capacitor with interface trap states causing stretch out.

2.6 Etching Techniques

Chemical etching is a technique used to remove materials that are not protected with mask by a liquid or gaseous form of the etchant. The choice of chemical depends on the materials to be etched. A higher selectivity is required so that the etchant will remove the uncovered material much more than the masking material. The photoresist is typically using a masking material since it shows higher selectivity with most of the etchants. The wet chemical or dry chemical etching

techniques are selected based on parameters such as the etch rate, selectivity, pattern size and etching material.

2.6.1 Wet Chemical Etching

Wet chemical etching is a purely chemical etching process. Liquid chemicals or etchants are using to remove material from the surface of a substrate. The device patterns are defined by a mask on the substrate. The masks are deposited and patterned on the substrate by photolithography prior to the wet chemical etching process. Areas that are not protected by the mask are etched away by the chemical reaction [92].

In wet chemical etching, multiple chemical reactions are possible to aid the material removal process through original reactant itself and a by-product of primary reactions. The wet chemical etching process can be described by three main mechanisms;

1. Diffusion of the liquid etchant to the substrate that needs to be etched.
2. The redox reaction between the liquid etchant and the material. The redox reaction entails the oxidation of the material and then dissolve the oxidized material.
3. Diffusion of the by-products in the reaction from the reacted surface.

When a material is exposed to liquid or vapor etchant, it can be removed uniformly in all directions (isotropically) or uniformly only in the vertical direction (anisotropically). The etch rate is usually higher in wet chemical etching compared to dry etching. The etch rate can be varied with the temperature and the concentration of the etchant. Wet chemical etching is an isotropic process even with a mask since liquid etchant can penetrate through the mask to etch underneath the mask. For example, a mixture of hydrofluoric acid (HF), hydrocholic acid (HCl), nitric acid (HNO_3), and acetic acid (HNA) is the most common liquid etchant used for silicon etching through

the wet chemical process. Silicon dioxide (SiO_2) or silicon nitride (Si) is used as a mask material against HNA.

If the directionality of the etching process is very important for high-resolution pattern transfer, dry etching is used instead of wet chemical etching due to its anisotropic etching property. Figure 2.6-1 shows the schematic diagrams of anisotropic and isotropic etching profiles. The recipe of wet chemical etching performed for mesa etching in ZnO TFTs fabrication in chapter 6 and 7 is showed in table 2.6-1.

Table 2.6-1 The recipe of wet chemical etching and the yield

Etchent	Etch rate	Etch temperature
di. H_2O:HCl= 100:1	30 nm/s	Room temperature

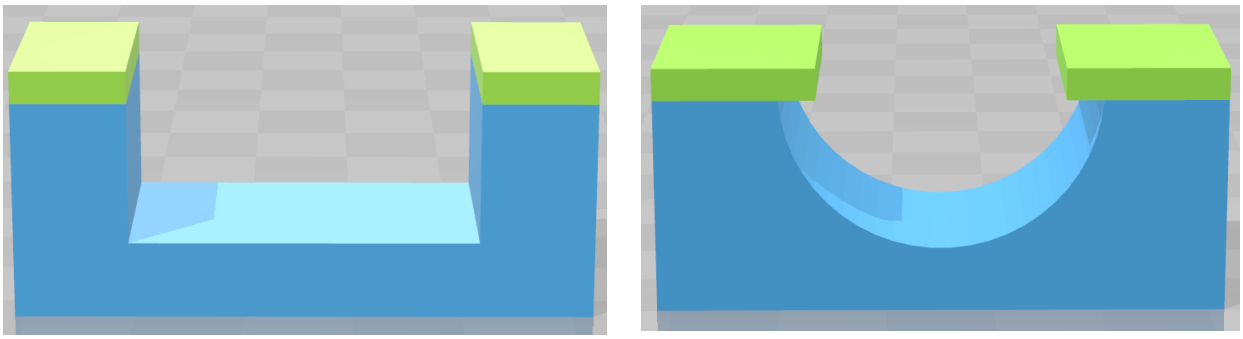

(a) (b)

Figure 2.6-1: Schematics of (a) anisotropic, and (b) isotropic etching profiles.

References

[1] M. Schumm, “ZnO-based semiconductors studied by Raman spectroscopy: semimagnetic alloying, doping, and nanostructures,” 2010.

[2] T. Sekiguchi, S. Miyashita, K. Obara, T. Shishido, and N. Sakagami, “Hydrothermal growth of ZnO single crystals and their optical characterization,” *J. Cryst. Growth*, vol. 214, pp. 72–76, 2000.

[3] N. Sakagami, M. Yamashita, T. Sekiguchi, S. Miyashita, K. Obara, and T. Shishido, “Variation of electrical properties on growth sectors of ZnO single crystals,” *J. Cryst. Growth*, vol. 229, no. 1, pp. 98–103, 2001.

[4] W.-J. Li, E.-W. Shi, W.-Z. Zhong, and Z.-W. Yin, “Growth mechanism and growth habit of oxide crystals,” *J. Cryst. Growth*, vol. 203, no. 1, pp. 186–196, 1999.

[5] T. Kogure and Y. Bando, “Formation of ZnO nanocrystals in the cubic phase was reported by electron-beam induced oxidation of ZnS surfaces during TEM observations,” *J Electron Microsc*, vol. 47, p. 7903, 1993.

[6] A. A. Ashrafi *et al.*, “Growth and characterization of hypothetical zinc-blende ZnO films on GaAs (001) substrates with ZnS buffer layers,” *Appl. Phys. Lett.*, vol. 76, no. 5, pp. 550–552, 2000.

[7] S.-K. Kim, S.-Y. Jeong, and C.-R. Cho, “Structural reconstruction of hexagonal to cubic ZnO films on Pt/Ti/SiO 2/Si substrate by annealing,” *Appl. Phys. Lett.*, vol. 82, no. 4, pp. 562–564, 2003.

[8] H. Karzel *et al.*, “Lattice dynamics and hyperfine interactions in ZnO and ZnSe at high external pressures,” *Phys. Rev. B*, vol. 53, no. 17, p. 11425, 1996.

[9] J. Albertsson, S. C. Abrahams, and Å. Kvick, “Atomic displacement, anharmonic thermal vibration, expansivity and pyroelectric coefficient thermal dependences in ZnO,” *Acta Crystallogr. B*, vol. 45, no. 1, pp. 34–40, Feb. 1989.

[10] J. A. Duffy, “Ionic- Covalent Character of Metal and Nonmetal Oxides,” *J. Phys. Chem. A*, vol. 110, no. 49, pp. 13245–13248, 2006.

[11] F. Bernardini, V. Fiorentini, and D. Vanderbilt, “Spontaneous polarization and piezoelectric constants of III-V nitrides,” *Phys. Rev. B*, vol. 56, no. 16, pp. R10024–R10027, Oct. 1997.

[12] Z. L. Wang, “Zinc oxide nanostructures: growth, properties and applications,” *J. Phys. Condens. Matter*, vol. 16, no. 25, p. R829, 2004.

[13] S. S. Alias and A. A. Mohamad, *Synthesis of Zinc Oxide by Sol–Gel Method for Photoelectrochemical Cells*. Springer Science & Business Media, 2013.

[14] J. Nishii *et al.*, “High mobility thin film transistors with transparent ZnO channels,” *Jpn. J. Appl. Phys.*, vol. 42, no. 4A, p. L347, 2003.

[15] O. Dulub, L. A. Boatner, and U. Diebold, “STM study of the geometric and electronic structure of ZnO (0001)-Zn,(0001)-O,(1010), and (1120) surfaces,” *Surf. Sci.*, vol. 519, no. 3, pp. 201–217, 2002.

[16] S.-H. Wei and A. Zunger, “Role of metal d states in II-VI semiconductors,” *Phys. Rev. B*, vol. 37, no. 15, p. 8958, 1988.

[17] J. L. Martins, N. Troullier, and S.-H. Wei, “Pseudopotential plane-wave calculations for ZnS,” *Phys. Rev. B*, vol. 43, no. 3, p. 2213, 1991.

[18] Y.-N. Xu and W. Y. Ching, “Electronic, optical, and structural properties of some wurtzite crystals,” *Phys. Rev. B*, vol. 48, no. 7, p. 4335, 1993.

[19] D. Vogel, P. Krüger, and J. Pollmann, “Ab initio electronic-structure calculations for II-VI semiconductors using self-interaction-corrected pseudopotentials,” *Phys. Rev. B*, vol. 52, no. 20, p. R14316, 1995.

[20] S. J. Pearton, D. P. Norton, K. Ip, Y. W. Heo, and T. Steiner, “Recent progress in processing and properties of ZnO,” *Prog. Mater. Sci.*, vol. 50, no. 3, pp. 293–340, 2005.

[21] A. Mang, K. Reimann, and others, “Band gaps, crystal-field splitting, spin-orbit coupling, and exciton binding energies in ZnO under hydrostatic pressure,” *Solid State Commun.*, vol. 94, no. 4, pp. 251–254, 1995.

[22] B. K. Meyer *et al.*, “Bound exciton and donor–acceptor pair recombinations in ZnO,” *Phys. Status Solidi B*, vol. 241, no. 2, pp. 231–260, Feb. 2004.

[23] C. Jagadish and S. J. Pearton, *Zinc oxide bulk, thin films and nanostructures: processing, properties, and applications*. Elsevier, 2011.

[24] T. Makino, Y. Segawa, M. Kawasaki, and H. Koinuma, "Optical properties of excitons in ZnO-based quantum well heterostructures," *Semicond. Sci. Technol.*, vol. 20, no. 4, p. S78, 2005.

[25] S. Adachi, *Properties of group-IV, III-V and II-VI semiconductors, series in materials for electronic and optoelectronic application*. New York: Wiley, 2005.

[26] K. Koike *et al.*, "Molecular beam epitaxial growth of wide bandgap ZnMgO alloy films on (111)-oriented Si substrate toward UV-detector applications," *J. Cryst. Growth*, vol. 278, no. 1, pp. 288–292, 2005.

[27] S. Shigemori, A. Nakamura, J. Ishihara, T. Aoki, and J. Temmyo, "Zn1-xCdxO film growth using remote plasma-enhanced metalorganic chemical vapor deposition," *Jpn. J. Appl. Phys.*, vol. 43, no. 8B, p. L1088, 2004.

[28] A. Ohtomo *et al.*, "Mg x Zn 1- x O as a II–VI widegap semiconductor alloy," *Appl. Phys. Lett.*, vol. 72, no. 19, pp. 2466–2468, 1998.

[29] T. Makino *et al.*, "Band gap engineering based on Mg x Zn 1- x O and Cd y Zn 1- y O ternary alloy films," *Appl. Phys. Lett.*, vol. 78, no. 9, pp. 1237–1239, 2001.

[30] Y. Chen *et al.*, "Plasma assisted molecular beam epitaxy of ZnO on c-plane sapphire: growth and characterization," *J. Appl. Phys.*, vol. 84, no. 7, pp. 3912–3918, 1998.

[31] K. Vanheusden, W. L. Warren, C. H. Seager, D. R. Tallant, J. A. Voigt, and B. E. Gnade, "Mechanisms behind green photoluminescence in ZnO phosphor powders," *J. Appl. Phys.*, vol. 79, no. 10, pp. 7983–7990, 1996.

[32] H. S. Kang, J. S. Kang, J. W. Kim, and S. Y. Lee, "Annealing effect on the property of ultraviolet and green emissions of ZnO thin films," *J. Appl. Phys.*, vol. 95, no. 3, pp. 1246–1250, 2004.

[33] Y.-J. Lin, C.-L. Tsai, Y.-M. Lu, and C.-J. Liu, "Optical and electrical properties of undoped ZnO films," *J. Appl. Phys.*, vol. 99, no. 9, p. 093501, 2006.

[34] B. Lin, Z. Fu, and Y. Jia, "Green luminescent center in undoped zinc oxide films deposited on silicon substrates," *Appl. Phys. Lett.*, vol. 79, no. 7, pp. 943–945, 2001.

[35] X. Liu, X. Wu, H. Cao, and R. P. H. Chang, "Growth mechanism and properties of ZnO nanorods synthesized by plasma-enhanced chemical vapor deposition," *J. Appl. Phys.*, vol. 95, no. 6, pp. 3141–3147, 2004.

[36] W. S. Shi, O. Agyeman, and C. N. Xu, "Enhancement of the light emissions from zinc oxide films by controlling the post-treatment ambient," *J. Appl. Phys.*, vol. 91, no. 9, pp. 5640–5644, 2002.

[37] S. O. Kucheyev, J. E. Bradby, J. S. Williams, C. Jagadish, and M. V. Swain, “Mechanical deformation of single-crystal ZnO,” *Appl. Phys. Lett.*, vol. 80, no. 6, pp. 956–958, 2002.

[38] S. Desgreniers, “High-density phases of ZnO: Structural and compressive parameters,” *Phys. Rev. B*, vol. 58, no. 21, p. 14102, 1998.

[39] J. E. Jaffe and A. C. Hess, “Hartree-Fock study of phase changes in ZnO at high pressure,” *Phys. Rev. B*, vol. 48, no. 11, p. 7903, 1993.

[40] I. B. Kobiakov, “Elastic, piezoelectric and dielectric properties of ZnO and CdS single crystals in a wide range of temperatures,” *Solid State Commun.*, vol. 35, no. 3, pp. 305–310, 1980.

[41] R. Ahuja, L. Fast, O. Eriksson, J. M. Wills, and B. Johansson, “Elastic and high pressure properties of ZnO,” *J. Appl. Phys.*, vol. 83, no. 12, pp. 8065–8067, 1998.

[42] M. Catti, Y. Noel, and R. Dovesi, “Full piezoelectric tensors of wurtzite and zinc blende ZnO and ZnS by first-principles calculations,” *J. Phys. Chem. Solids*, vol. 64, no. 11, pp. 2183–2190, 2003.

[43] Y. Noel, C. M. Zicovich-Wilson, B. Civalleri, P. D’arco, and R. Dovesi, “Polarization properties of ZnO and BeO: An ab initio study through the Berry phase and Wannier functions approaches,” *Phys. Rev. B*, vol. 65, no. 1, p. 014111, 2001.

[44] E. F. Tokarev, I. B. Kobyakov, I. P. Kuz’mina, A. N. Lobachev, and G. S. Pado, “Elastic dielectric and piezoelectric properties of zincite in the 4.2–800° K temperature range,” *Sov Phy Solid State*, vol. 17, pp. 629–632, 1975.

[45] A. Polian, M. Grimsditch, and I. Grzegory, “Elastic constants of gallium nitride,” *J. Appl. Phys.*, vol. 79, no. 6, pp. 3343–3344, 1996.

[46] F. D. Murnaghan, “The compressibility of media under extreme pressures,” *Proc. Natl. Acad. Sci.*, vol. 30, no. 9, pp. 244–247, 1944.

[47] A. Dal Corso, M. Posternak, R. Resta, and A. Baldereschi, “Ab initio study of piezoelectricity and spontaneous polarization in ZnO,” *Phys. Rev. B*, vol. 50, no. 15, p. 10715, 1994.

[48] Ü. Özgür *et al.*, “A comprehensive review of ZnO materials and devices,” *J. Appl. Phys.*, vol. 98, no. 4, p. 11, 2005.

[49] J. R. Ferraro, *Introductory raman spectroscopy*. Academic press, 2003.

[50] V. Russo, M. Ghidelli, P. Gondoni, C. S. Casari, and A. Li Bassi, "Multi-wavelength Raman scattering of nanostructured Al-doped zinc oxide," *J. Appl. Phys.*, vol. 115, no. 7, p. 073508, 2014.

[51] H. Harima, "Properties of GaN and related compounds studied by means of Raman scattering," *J. Phys. Condens. Matter*, vol. 14, no. 38, p. R967, 2002.

[52] J. M. Calleja and M. Cardona, "Resonant Raman scattering in ZnO," *Phys. Rev. B*, vol. 16, no. 8, p. 3753, 1977.

[53] F. Decremps, J. Pellicer-Porres, A. M. Saitta, J.-C. Chervin, and A. Polian, "High-pressure Raman spectroscopy study of wurtzite ZnO," *Phys. Rev. B*, vol. 65, no. 9, p. 092101, 2002.

[54] R. Cuscó *et al.*, "Temperature dependence of Raman scattering in ZnO," *Phys. Rev. B*, vol. 75, no. 16, p. 165202, 2007.

[55] M. S. Jang *et al.*, "A study on the Raman spectra of Al-doped and Ga-doped ZnO ceramics," *Curr. Appl. Phys.*, vol. 9, no. 3, pp. 651–657, 2009.

[56] R. Al Asmar *et al.*, "Characterization and Raman investigations on high-quality ZnO thin films fabricated by reactive electron beam evaporation technique," *J. Cryst. Growth*, vol. 279, no. 3, pp. 394–402, 2005.

[57] F. J. Manjón, B. Mari, J. Serrano, and A. H. Romero, "Silent Raman modes in zinc oxide and related nitrides," *J. Appl. Phys.*, vol. 97, no. 5, p. 053516, 2005.

[58] S. B. Yahia, L. Znaidi, A. Kanaev, and J. P. Petitet, "Raman study of oriented ZnO thin films deposited by sol–gel method," *Spectrochim. Acta. A. Mol. Biomol. Spectrosc.*, vol. 71, no. 4, pp. 1234–1238, 2008.

[59] T. C. Damen, S. P. S. Porto, and B. Tell, "Raman effect in zinc oxide," *Phys. Rev.*, vol. 142, no. 2, p. 570, 1966.

[60] C. A. Arguello, D. L. Rousseau, and S. P. da S. Porto, "First-order Raman effect in wurtzite-type crystals," *Phys. Rev.*, vol. 181, no. 3, p. 1351, 1969.

[61] Y. Huang, M. Liu, Z. Li, Y. Zeng, and S. Liu, "Raman spectroscopy study of ZnO-based ceramic films fabricated by novel sol–gel process," *Mater. Sci. Eng. B*, vol. 97, no. 2, pp. 111–116, 2003.

[62] J.-M. Wagner and F. Bechstedt, "Phonon deformation potentials of α-GaN and-AlN: An ab initio calculation," *Appl. Phys. Lett.*, vol. 77, no. 3, pp. 346–348, 2000.

[63] J. Gleize, F. Demangeot, J. Frandon, M. A. Renucci, F. Widmann, and B. Daudin, “Phonons in a strained hexagonal GaN–AlN superlattice,” *Appl. Phys. Lett.*, vol. 74, no. 5, pp. 703–705, 1999.

[64] P. Gopal and N. A. Spaldin, “Polarization, piezoelectric constants, and elastic constants of ZnO, MgO, and CdO,” *J. Electron. Mater.*, vol. 35, no. 4, pp. 538–542, 2006.

[65] G. Carlotti, D. Fioretto, G. Socino, and E. Verona, “Brillouin scattering determination of the whole set of elastic constants of a single transparent film of hexagonal symmetry,” *J. Phys. Condens. Matter*, vol. 7, no. 48, p. 9147, 1995.

[66] A.-J. Cheng *et al.*, “Raman analysis of longitudinal optical phonon-plasmon coupled modes of aligned ZnO nanorods,” *J. Appl. Phys.*, vol. 105, no. 7, p. 073104, 2009.

[67] M. J. Matthews, J. W. P. Hsu, S. Gu, and T. F. Kuech, “Carrier density imaging of lateral epitaxially overgrown GaN using scanning confocal Raman microscopy,” *Appl. Phys. Lett.*, vol. 79, no. 19, pp. 3086–3088, 2001.

[68] M. Oshikiri, Y. Imanaka, F. Aryasetiawan, and G. Kido, “Comparison of the electron effective mass of the n-type ZnO in the wurtzite structure measured by cyclotron resonance and calculated from first principle theory,” *Phys. B Condens. Matter*, vol. 298, no. 1, pp. 472–476, 2001.

[69] H. Yoshikawa and S. Adachi, “Optical constants of ZnO,” *Jpn. J. Appl. Phys.*, vol. 36, no. 10R, p. 6237, 1997.

[70] H. B. Bebb and E. W. Williams, “Photoluminescence I: theory,” *Semicond. Semimet.*, vol. 8, pp. 181–320, 1972.

[71] K. K. Smith, “Photoluminescence of semiconductor materials,” *Thin Solid Films*, vol. 84, no. 2, pp. 171–182, 1981.

[72] D. K. Schroder, *Semiconductor Material and Device Characterization*. John Wiley & Sons, 2006.

[73] J. I. Pankove, *Optical Processes in Semiconductors*. Courier Corporation, 2012.

[74] P. J. Dean, “Photoluminescence as a diagnostic of semiconductors,” *Prog. Cryst. Growth Charact.*, vol. 5, no. 1–2, pp. 89–174, 1982.

[75] R. J. Almassy, D. C. Reynolds, C. W. Litton, K. K. Bajaj, and D. C. Look, “Sharp line emission spectra from GaAs FET like structures,” *J. Electron. Mater.*, vol. 7, no. 2, pp. 263–277, 1978.

[76] M. Wei, C.-F. Li, X.-R. Deng, and H. Deng, “Surface work function of transparent conductive ZnO films,” *Energy Procedia*, vol. 16, pp. 76–80, 2012.

[77] S. M. Sze and K. K. Ng, *Physics of semiconductor devices*. John wiley & sons, 2006.

[78] W. Shockley, "Research and investigation of inverse epitaxial uhf power transistors, air force atomic laboratory, wright-patterson air force base," *Ohio Rep AL-TOR-64-207 Sept 1964*, 1964.

[79] H. B. Harrison, *Characterizing metal semiconductor ohmic contacts*. Royal Melbourne Institute of Technology, 1980.

[80] B. V. Zeghbroeck, "Principles of Semiconductor Devices (2011)," *URL Httpecee Colo. Edubartbookbookchapter3ch34 Htm*, 2015.

[81] C. N. Berglund, "Surface states at steam-grown silicon-silicon dioxide interfaces," *IEEE Trans. Electron Devices*, vol. 13, no. 10, pp. 701–705, 1966.

[82] E. H. Nicollian and A. Goetzberger, "The Si-SiO2 Interface—Electrical Properties as Determined by the Metal-Insulator-Silicon Conductance Technique," *Bell Syst. Tech. J.*, vol. 46, no. 6, pp. 1055–1133, 1967.

[83] L. M. Terman, "An investigation of surface states at a silicon/silicon oxide interface employing metal-oxide-silicon diodes," *Solid-State Electron.*, vol. 5, no. 5, pp. 285–299, 1962.

[84] P. V. Gray and D. M. Brown, "Density of SiO2–Si interface states," *Appl. Phys. Lett.*, vol. 8, no. 2, pp. 31–33, 1966.

[85] A. Mir and D. Vuillaume, "Positive charge and interface state creation at the Si-SiO2 interface during low-fluence and high-field electron injections," *Appl. Phys. Lett.*, vol. 62, no. 10, pp. 1125–1127, 1993.

[86] D. W. Greve, *Field Effect Devices and Applications: Devices for Portable, Low-power, and Imaging Systems*. Upper Saddle River, NJ, USA: Prentice-Hall, Inc., 1998.

[87] B. E. Deal, M. Sklar, A. S. Grove, and E. H. Snow, "Characteristics of the Surface-State Charge (Qss) of Thermally Oxidized Silicon," *J. Electrochem. Soc.*, vol. 114, no. 3, pp. 266–274, 1967.

[88] W.-K. Hong *et al.*, "Tuning of the Electronic Characteristics of ZnO Nanowire Field Effect Transistors by Proton Irradiation," *ACS Nano*, vol. 4, no. 2, pp. 811–818, Feb. 2010.

[89] M. Lenzlinger and E. H. Snow, "Fowler-Nordheim tunneling into thermally grown SiO2," *J. Appl. Phys.*, vol. 40, no. 1, pp. 278–283, 1969.

[90] T. R. Oldham and F. B. McLean, “Total ionizing dose effects in MOS oxides and devices,” *IEEE Trans. Nucl. Sci.*, vol. 50, no. 3, pp. 483–499, 2003.

[91] E. H. Nicollian, J. R. Brews, and E. H. Nicollian, *MOS (metal oxide semiconductor) physics and technology*, vol. 1987. Wiley New York et al., 1982.

[92] R. C. Jaeger, G. W. Neudeck, and R. F. Pierret, *Introduction to Microelectronic Fabrication, 2002*. Prentice Hall.

Chapter 3
Radiation Environmental conditions

3.1 Characterization of Radiations

The types of radiation can be categorized into charged particle radiation (electron, alpha, proton and other ions) and neutral radiation including photons (X-ray and gamma) and neutrons. Some key characteristics of each types radiations are summarized in table 3.1-1.

Table 3.1-1 Characteristics of ionizing radiation of 1MeV

	Alpha (α)	Proton (p)	Electron (e)	Gamma (γ)	Neutron (n)
Symbol	${}^{4}_{2}\alpha$ or He^{2+}	${}^{1}_{1}p$ or H^{+}	${}^{0}_{-1}e$ or β	${}^{0}_{0}\gamma$	${}^{1}_{0}n$
Charge	+2	+1	-1	neutral	neutral
Ionization	Direct	Direct	Direct	Indirect	Indirect
Mass (amu)	4.001506	1.007276	0.000549	-	1.008665
Velocity (m/s)	6.944×10^{6}	1.38×10^{7}	2.82×10^{8}	2.998×10^{8}	1.38×10^{7}
Speed of light	2.3%	4.6%	94.1%	100%	4.6%
Range in air (cm)	0.56	1.81	319	82000*	39250*

*based on 99.9% reduction

I. Charged Particle Radiation

The fundamental behavior of the charged particle radiation (*α, β, p*) is different from the neutral radiation (γ, *n*). For the same energy, heavy charged particles are slower, and the penetration depth into a material is small due to a rapid drop in its kinetic energy (higher stopping

potential). Charged particles strongly interact with the orbital electrons of elements in the material, thereby it is known as directly ionizing radiation. Moreover, the charged particle radiation can be categorized into two sub-section 1) heavy charged particle radiation (α, p), 2) light electrons.

1. **Heavy Charged Particle Radiation**

    In the beginning, heavy charged particles slow down by losing energy through interactions with electrons. Since charged particles are much heavier than electrons, they are rarely deflected from its path after electron interaction. Hence, they move in a straight path. Once heavy particles lose enough energy such that they do not have sufficient energy to excite electrons, the collision with nuclei becomes prominent. When nuclei receive sufficient transferred energy through collision which is larger than the atomic displacement energy threshold of the element, the atom can be removed from its original lattice point to create displacement damage. The heavy particles slow down almost entirely by Coulombic interactions with the atomic electrons. In contrast to the neutral radiation, heavy charged particles have well defined stopping potential for materials.

2. **Light Electrons**

    In the case of electron radiation, several interaction processes could be possible such as ionization, the creation of X-ray from the electron deceleration (Bremsstrahlung), and elastic scattering from nuclear and electron interactions. The scattered electrons tend to have an undefined random path. Therefore, its range is greater compared to heavy particles with the same energy.

II. Neutral Radiation

Neutral radiation can cause either direct ionized particles or transformation in the nucleus. Neutral radiation includes uncharged particle radiation such as neutron and photon radiation (γ). The fundamental interactions of neutron are scattering and absorption through capture and fission. Neutrons captured by a nucleus does change the isotope present. The new isotope could be radioactive and decay to change the chemical element present. During the decay process, additional radiation emits to the material.

The primary interaction of photon can be described in three mechanisms;

a) **Photoelectric Effect**: The photoelectric effect is prominent when the photon energy is less than 200 keV (E< 200keV). The incoming photon transfers its total energy into an orbital electron resulting an ejected electron. The ejected electron contains kinetic energy equals the energy difference between photon energy and the binding energy of the electron (KE= E_γ – BE).

b) **Compton Effect**: The elastic scattering between the photon and orbital electron results in an excited electron and scattered photon. Typically the Compton effect occurs with photon energy range 200 keV to 1.5 MeV. Scattered photon often has reduced energy and the direction change from the original incident photon.

c) **Pair Production**: The absorbed photon produces an electron-positron pair. The rest mass energy of electron/positron is 0.511 MeV. Hence the minimum required photon energy to obtain pair production is 1.02 MeV. Photons with energy higher than 1.5 MeV more likely to produce electron-positron pair in the matter with the kinetic energy of energy difference between photon energy and the pair production energy (KE= $E_\gamma – 2m_eC^2$). Eventually, the

positron and the electron recombines emitting two photons (annihilation radiation) with 0.511 MeV of each.

3.2 Space Radiation (Van Allen Radiation Belts)

The idea of the existence of radiation belts that trapped energetic particles by the Earth's magnetic field is first claimed by James Van Allen and his team in May 1958 at a meeting of the American Geophysical Union. In November 1957, Soviet scientists launched *Sputnik 2* which is the second human-made satellite ever sent into the Earth's orbit after their successful first launch, *Sputnik 1*. Soviet scientist, Sergei Vernov placed a Geiger-Muller (G-M) tube in *Sputnik* 2 to measure radiation encountered by the satellite in Earth's orbit [1]. Vernov has been studying the cosmic rays by using ground-based balloons at Moscow State University. Therefore, he wanted to explore the primary cosmic-ray particles from the deep galaxy before they interact with the Earth's atmosphere with *Sputnik 2* data. After less than three months of Sputnik 2 launch, the US launched their first artificial satellite, *Explorer 1* using Jupiter C rocket in January 1958. The US physicist, James Van Allen and his team at the University of Iowa were studying cosmic radiation with rockets and balloons even many years before the *Explorer 1* launch just like Vernov. Van Allen and his team designed, built and installed a Geiger-Muller tube on board *Explore 1*[2].

When Vernov and his team observed the data from *Sputnik 2*, they identified a significant fluctuation in G-M count rate. However, they interpreted the observation as fluctuations due to the interference of charged particles from a solar flare. As a result of the total secrecy of Soviet science in that period, Soviet scientists could not collect data from *Sputnik 2* received by other nations. However, Van Allen and his team realized that the observed fluctuation in G-M count rate from *Explorer 1* data is due to natural phenomenon. The count rate was far high for some period, and

then it dropped to zero for another period. Otherwise, it matched with expected cosmic rays. They first assumed the drop in count rate is due to low-energy particles encounter. However, later they realized that an area with higher particle flux would drive the G-M tube to saturation and it would stop counting entirely. This explanation was a breakthrough in the Geophysical research community. Then the Soviet scientists launched *Sputnik 3*, much larger satellite equipped with complex equipment to study the particle trapped in Earth's Magnetosphere. The data collected from *Sputnik 3* mission allowed to identify an outer zone of intense radiation separated from the inner zone. The inner and the outer radiation belts later named after the pioneer James Van Allen, *Van Allen Radiation belts*.

The majority of the inner belt contained by high energetic protons (0.1-40 MeV) and the outer belt composed of energetic electrons (0.1-7 MeV) [3]. It is estimated that the inner radiation belt is located in the lower altitude, which extends from above the atmosphere out to about 2.5 Earth radii. The outer radiation belt located at the altitude of 3-10 Earth radii. It is believed that the *Sputnik 2* was launched at the higher altitude and its orbital trajectory interfered with outer radiation belt. On the other hand, the *Explorer 1* was launched into equatorial orbit and the satellite's orbit extended to the inner radiation belt.

Soviet scientists Vernov and Alexander Lebedinsky of MSU first proposed the origins of the radiation belts in July 1958, only a few months after the discovery of the radiation belts. They claimed that the cosmic rays have too much momentum to become trapped. However, when cosmic rays interfere with the Earth's atmosphere, it creates neutrons as a result of nuclear reactions. Eventually, the created neutrons decay into electrons and protons that are trapped in Earth's magnetic field to generate radiation belts. A US scientist, Fred Singer also independently published a similar mechanism to describe the origin of the trapped electrons and proton in

radiation belts [4]. Later, researchers realized that proposed neutron decay model could successfully explain the trapped proton in the inner radiation belt, the trapped electrons in the outer belt are variable of radial extent, overall intensity, and energy range. The properties of the outer belt merely depend on the strength of the solar winds interact with the magnetosphere and thereby the acceleration and the transport of the electrons.

The apparent use of the naturally existed radiation belts was to keep the dangerous cosmic rays from reaching to the Earth's surface and affecting lives. Later, some researchers suggested that the high charged particle flux in the radiation belts can be utilized as a defensive screen against Intercontinental Ballistic Missiles (ICBs). The idea was that intense radiation in the radiation belt could disable the ICBs launched through the region. This idea was drawn Van Allen's team into classified experiments of nuclear explosions in space. The series of human-made nuclear explosions by the US and the Soviet Union in the 1960s severely altered the inner Van Allen radiation belt and introduced electrons with MeV energies to last for many years [5]. The human-made radiation intensified the radiation belt at least million times and made a hostile environment for satellites. Therefore, it was confirmed that artificially injection of particles into the Earth's magnetic field could create stable trapped flux region around the Earth.

Apart from the cosmic rays, there are several others sources of matters contribute to the radiation belts. They include solar plasma penetrated the Earth's magnetosphere, and ionospheric particles injected into the radiation belt region during magnetic storms. Among other sources, anomalous cosmic rays generated in the outer solar systems, particles of interplanetary matter that escaped from Jupiter's magnetosphere and travel towards Earth through interplanetary magnetic field lines are dominated.

With the technological evolution, Earth's human-made satellites have been launched for atmospheric studies, communications, navigation, weather observations, military surveillance, remote sensing and many other purposes. The conditions in the radiation belts extend serious threat to those satellites [6]. Therefore, understanding the variation and the detailed behavior of the Van Allen belts is essential. Since the 1970s to 1990s, space missions such as *the Combined Release and Radiation Effects Satellite* and NASA's *Solar Anomalous and Magnetospheric Particle Explorer* discovered vital information about the Van Allen belts such as loss of particles from the belts, particle acceleration, and the high-energy events during the solar activities. In 2012 NASA launched Van Allen probe mission which is a dual-spacecraft mission to explore the spatial structure and the dynamics of the radiation belt regions. The data from this mission revealed the existence of a third distinct population of energetic particles [7]. It was identified that the third radiation belt located in between inner and outer Van Allen belts consisted of ultrarelativistic electrons with energies greater than 2 MeV. The space missions conducted by the US, Russia and other nations were able to explore more about the Van Allen radiation belts such as the barrier to transport charged particles from the outer to the inner belt, fluctuation in the population of high-energy protons, and the existence of electric field that control the particles in the radiation belts [8]. The most recent satellites for space-environment studies were launched in December 2016 by Japan (Arase) and Russia (Lomonosov).

3.3 Radiation-Induced Damage

The detrimental effects on the performance of the microelectronics once they exposed to radiation is known as radiation-induced damage. The degree of the damage and its influence depend on parameters such as the type of radiation, energies, dose, and also the exposed material.

The general types of radiation-induced effect can be categorized into four such as 1) ionization, 2) atom displacement 3) impurity production, and 4) energy deposition.

1. Ionization

The ionization is a process that strips electrons from atoms in the material, thereby creating ions. The electron excitation is the closely related mechanism of ionization. However, the excitation happens when the energy is less than the potential for ionization. The charged particle radiation such as alpha (α), beta (β) and proton induce direct ionization to the material while neutral radiation such as neutron, and gamma (γ) cause indirect ionization. The susceptibility of ionization damage varies with the type of bonding in the material. Metallic bonding holds positive ions together with free valence electrons. Ionization radiation excites the electron to higher energy level, but they relax to its original energy state shortly. Therefore, there is no permanent damage occurred due to the ionization of metallic bonding. Ionic bonding is weaker than metallic bonding in ionization prospect. In ionic bonding, one element transfers its loosely bound electron to another element to create positive ion (cation) and negative ion (anion). The electrostatic attraction and repulsion between cation and anion lead to a well ordered three-dimensional arrangement in the crystal structure. The ionization could create a higher positive charge in cation due to electron stripping and hence enhanced the attraction between cation and anion. However, the ionization effect is temporary in ionic bonding due to its fast recovery of the excited electrons. The covalent bonding found in compounds such as H_2O, CO_2, Si, SiO_2, etc. shares outer electrons in a molecule between all the atoms. The resultant covalent molecules do not attract one another, and the energy of the bonding is in low eV range. Hence, the radiation has enough energy to separate the covalent

molecule into its constituent atoms or radicals through ionization. Therefore, the original chemical composition of the material changes leaving permanent damage.

ZnO has ionic bonding between Zn^{+2} and O^{-2} cation and anion [9]. On the other hand, Si and SiO_2 show covalent bonding in the lattice. Therefore, it is apparent that ionization effect in a microelectronic structure composed of ZnO/SiO_2/Si would be significant in the SiO_2 dielectric layer and Si substrate rather than ZnO channel layer. Extensive research has done on the ionization effect in SiO_2 since it is a widely used gate dielectric material in the commercial electronic manufacturing. Ionization radiation generates electron-hole pair by exciting an electron from the valence band of the elements in SiO_2. Excited electrons tend to swipe to the grounded gate rather than recombination due to its higher mobility compared to holes. The holes left behind would move in the SiO_2 layer with an applied gate bias and eventually trap to generate positive trap charges in SiO_2 to influence the device's electrical stability as shown in figure 3.3-1.

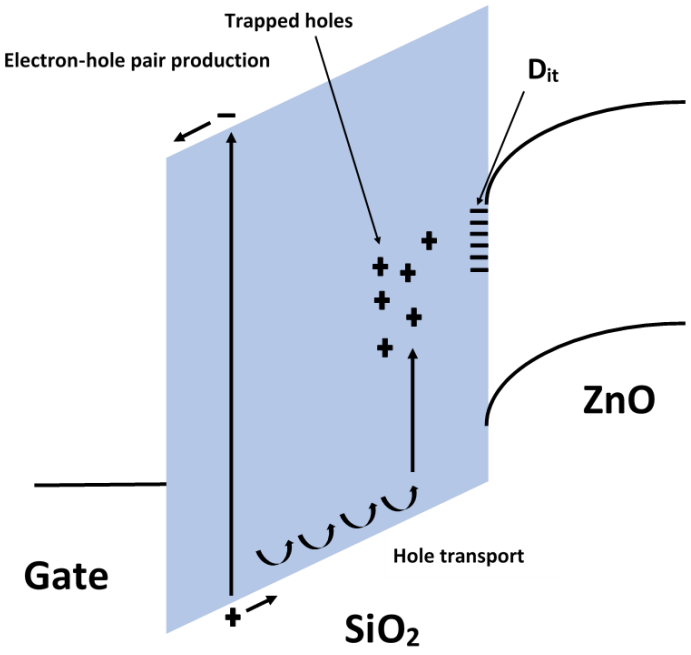

Figure 3.3-1: The band diagram of the device structure illustrating the ionization effect in SiO_2.

2. Atomic Displacement

The atomic displacement primarily occurs through kinetic energy transfer or radiolytically by the conversion of radiation-induced excitation into atom motion (recoil). When a charged particle passes through the material, some of the particle's energy dissipates by exciting orbital electrons of the elements and by elastic collisions with the nuclei. The atomic displacement damage is a result of an elastic nuclear collision caused by the incoming energetic particle. Due to the elastic collision, the atom could eject from its normal lattice position. The ejected atom is known as a primary knock-on, which may cause a cascade of atomic displacements before coming to rest. The figure 3.3-2 illustrates the mechanism of atomic displacement damage in a crystal structure.

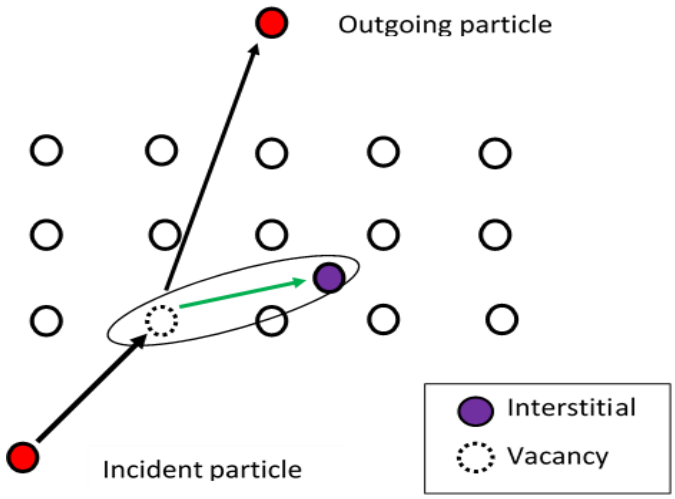

Figure 3.3-2: The schematic diagram of the mechanism of atomic displacement damage in a lattice.

The displaced atom becomes an interstitial, and its original vacant position in the lattice becomes a vacancy. Together the interstitial and the vacancy are known as a Frenkel pair. The displaced atom could continue the atomic displacement process with its excess transferred energy to create displacement cascade damage. The collisions are produced by both incident heavy

particles such as protons, neutrons, ions and secondary particles (recoils). The defects are produced along the path of the displacement cascade. The atomic displacement damage initiates when the transferred kinetic energy via elastic collision surpasses the atomic displacement energy threshold of the particular element or the compound. Therefore, the atomic displacement energy threshold is one of a measure of radiation hardness of a material. ZnO inherits one of the highest value compared to other mostly used materials as compared in the table 3.3-1.

Table 3.3-1: Atomic displacement energy threshold for selected materials [3],[10],[11],[12],[13] [14].

Material	Atomic displacement energy threshold (eV)
InAs	7.4
InP	7.8
GaAs	9.5
Si	12.9
Ge	14.5
GaN	19.5
4H-SiC	21.3
ZnO	57, 40-70 (Zn), and 47-55 (O), 18.5 (Zn), and 41.3 (O)

The protons impinging on *Zn* and *O* atoms in ZnO lattice would create simple Frankel pair by knocking out the particular atom and relocate it to the nearest interstitial position. However, as

argued previously, ZnO has a very high atomic displacement energy (133 eV for *Zn* and, 484 eV for *O*) for the creation of the nearest neighbor Frankel pair [15],[16] Look *et al.*[15] proposed a multiple displacement model where stable defects are created upon electron irradiations. The multiple displacement model has used Van Vechten's theoretical displacement energy values for *Zn* and *O* which has shown good agreement with experimental data as well as explained the atomic displacement mechanism in ZnO. In our work, we have utilized the multiple displacement model to identify the most likely displacement defects introduced to the ZnO lattice by 200 keV protons. We calculated the maximum energy transferred by protons after the elastic collision between the proton and the *Zn* or *O* nuclei (E_{max});

$$M_{\max(Zn)} = \frac{4M_pM_{Zn}}{(M_p+M_{Zn})^2}.E \qquad 3.3\text{-}1$$

Here, M_p is the atomic weight of the proton, M_{Zn} is the atomic weight of Zn and E is the energy of the proton beam. Here, the proton is treated as a non-relativistic particle. The E_{max} for *O* can be calculated by replacing M_{Zn} with an atomic weight of *O* (M_O) in equation 3.3-1.

After the initial knockoff of the Zn or O atom, the secondary particle could initiate multiple displacement chain reaction, and the energy associated with the total chain reaction ($E_{d,\,eff}$) could be calculated as follows; [15]

$$E_{d,eff(Zn)} = E_{d(Zn)} + \frac{E_{d(O)}}{R} + \frac{E_{d(Zn)}}{R^2} + \frac{E_{d(O)}}{R^3} + \cdots + \frac{E_{d(O)}}{R^{m-1}} \qquad 3.3\text{-}2$$

where $E_{d(Zn)}$ and $E_{d(O)}$ are theoretical displacement values for *Zn* and *O*, respectively. We have used the same Van Vechten's theoretical displacement values [14] as Look *et al.*[15] have used in their calculations; $E_{d(Zn)}$ = 18.5 eV and $E_{d(O)}$ = 41.5 eV. The calculated R value for ZnO is 0.6318 by $R = \frac{4M_{Zn}M_O}{(M_{Zn}+M_O)^2}$. The m is the total number of atoms displaced. When $E_{d,eff} < E_{max}$ for a certain m,

the particular chain displacement reaction corresponding to the *m* value is plausible to occure upon proton irradiation. When the *m* becomes larger, the displacement reaction chain becomes longer. Hence, the Frankel pair gets seperated far enough to create permenet damage to the lattice avoiding the defect recombination.

Displacement damage can be quantified using the non-ionizing energy loss (NIEL). The NIEL measures the energy lost to non-ionizing events per unit length, keV. cm^2/g. The product of NIEL and proton fluence (ψ) provides the displacement damage related deposited energy per unit mass of the material ($E_{d,\ (damage)}$), $E_{d,\ (damage)} = NIEL.\psi$ [17],[18]. The NIEL with respect to the penetration depth into the ZnO film can be calculated from the simulation data extracted from the Transport of Ion in Matters (TRIM) (see Appendix I) [19].

The production of interstitials and the vacancies involves the transfer of particle kinetic energy to potential energy stored in the lattice. Both interstitials and vacancies are mobile at sufficiently high temperature due to the increased vibration of the atoms in the lattice with supplied thermal energy [17]. Therefore, the interstitial atoms migrate to the vacancies to facilitate recombination, whereby the annealing process fix the induced displacement defects in the material [20],[21],[22].

3. Impurity Production

Impurities in a crystal structure induce imperfections to the lattice that alter electrical and mechanical properties. Electrons and photons do not directly introduce impurities to the lattice. However, they can cause impurity production indirectly through breaking chemical bonds. The neutron and ion radiation could show higher influence towards impurity production. In the case of ion radiation such as proton and alpha particle, the ion slows down eventually to capture necessary electrons to become neutral, thereby the protons (H^+) become Hydrogen and alpha particles

become Helium. At room temperature, both hydrogen and helium are in gas phase and exert pressure on its neighboring atoms. The internal pressurization mechanism in solids causes swelling in the material.

Apart from that the neutron and ion radiation could form radioactive species. Neutrons captured by a nucleus does change the isotope present. The new isotope could be radioactive and decay to change the chemical element present. During the decay process, additional radiation emits to the material.

4. Energy Deposition

Almost all the radiations cause energy deposition through ionization process within the material that exposed to the radiation. In organic materials, most of the absorbed ionization energy use for breaking chemical bonds while in metals, most of the absorbed energy appears as heat. The temperature rise due to the thermal heating could change some material properties. The volumetric heat generation rate in a material due to radiation ($\dot{Q}$) is the product of the absorbed dose rate ($\dot{D}$) and the material density (ρ);

$$\dot{Q} = \dot{D}\rho \qquad 3.3\text{-}3$$

3.4 Radiation Hard Electronics

Multiple approaches have employed independently or in combination to protect electronic systems in the radiation environment. So far, Shielding the vital electronic systems is the most common practical approach to protect electronics on board of space crafts. However, other approaches such as mission design, radiation hardening by architecture, design, and process are using in combination with shielding to enhance the protection of electronic systems from radiation.

When designing a shield for spacecraft, several factors needed to be analyzed such as radiation resistance of electronic devices used onboard, the ratio of minimum radiation limit for devices to be failed to amount of radiation in the desired location of spacecraft in space (radiation design margin), and self-shield analysis of electronic circuits [23]. These three factors are analyzed through extensive simulation process, and the results would aid to design additional shielding if necessary [24], [25]. In addition to the radiation hardening analysis, the weight and the volume limitations for the shedding material needs to be considered. Based on the satellite and the nature of the mission, spot shielding or local shielding are applied. These two types of shielding differ from each other based on weight, volume limitations and the parts of electronic systems that need to be shielded onboard [26]. When a collection of adjacent electronic devices or systems are required radiation shielding, the local shield is preferable. Notably, a large number of electronic devices are needed to be shielded from radiation environment such as nuclear power reactors. Therefore, local shielding over the entire electronic board is applied. However, such extensive shielding accompanied additional weight and volume to the electronic systems. In compact systems such as satellites, weight and volume are vital factors to consider as same as radiation hardening. Therefore, spot shielding is more practical in space mission applications. Also, the type and the dose of radiation that is expected to affect the electronic devices are also needed to consider in the design process. The radiation type and the dose merely depend on the altitude where the satellite will be located. The acceptable dose limitation for sensitive parts depends on the architecture of the devices. Typically, the shield thickness noted as aluminum thickness equivalent.

When positively charged particles irradiated on a dense matter, it tends to generate secondary radiation due to collision and particle splitting. Therefore, a higher thickness of shielding is required to stop secondary radiation to affect devices underneath [27]. In contrast,

lighter materials significantly reduce the generation of secondary radiation. However, its lighter density minimizes the particle stopping power, result in a larger thickness of shielding compared to the dense material is required to stop the radiation effect. Therefore, an ideal shield can be achieved by a multilayer shield consists of dense and light materials. Highly dense materials such as Tungsten and Tantalum and light materials such as polyethylene can be combined to achieve a better shield [23], [28]. The stopping power of a material is a useful parameter to consider during the investigation of the applicability of a material to be used in the shield. The stopping power is a measure of linear energy reduction along the material [24];

$$S = -\frac{dE}{dx} \tag{3.3-4}$$

The *S* values of protons can be calculated as,

$$S = \frac{4nZ^4e^4}{m_0v^2}NB = -\frac{dE}{dx} \tag{3.3-5}$$

$$\text{where } B = Z\left[ln\left(\frac{2m_0v^2}{I}\right) - ln\left(1 - \frac{v^2}{C^2}\right) - \frac{v^2}{C^2}\right] \tag{3.3-6}$$

where Z is the atomic density, *N* is the environment atomic number, m_0 is the electron inertia mass, *e* and *v* are the charges and the velocity of the radiated particle. Test analysis measures the potential of ionization and excitation of environment atom (*I*). The thickness of the shield determines based on the calculations total dose and the most sensitive part of the electronic system to be radiation resistance of 2 krad.

Mission design to minimize the radiation exposure of the spacecraft is another method to avoid device failure due to radiation. Since the space mission technology rapidly developed during past few decades, a higher level of limitations applied to mission design. Deep universe explorations accompanied higher risk of radiation exposure and could not be avoided. Therefore,

radiation hardening by architecture, design, and process drew more attention in research communities. Multiple levels of redundancy can be employed by the radiation such as component level, board level, subsystem level and spacecraft level. The triple module redundancy (TMR) method introduced to the electronic system architecture to identify the failed systems and correct the output with subsystems. A duplicative configuration of the vital electronic system is used to determine the faults by voting schemes. However, TMR method has its drawbacks with higher power consumption and additional weight.

In contrast, radiation hardening by design shows some advantages over architecture since TMR strategies can be introduced into the chip layout. Hence, the electronic systems can be designed to overcome the power consumption and additional mass issues as well. Also, designing dopant wells and isolated trenches into the chip layout, and device spacing and decoupling techniques are applied to the circuit design to achieve radiation hardness. Radiation hardening by the process is still at preliminary research level since it requires extensive research to replace the existing process with the new. Testing of new materials and process techniques are taking place in dedicated radiation-hard foundry fabrication facilities such as NASA's jet propulsion laboratories (JPL). NASA spacecraft developers have defined a radiation hardness assurance (RHA) methodology process [29]. NASA has launched the radiation hardened electronics for space environments (RHESE) project to deliver new technology and methodologies to implement RHA standards for constellation missions. The primary goal of the RHESE is to expand current state-of-the-art in radiation hardened electronics to develop high-performance devices robust enough to withstand the radiation conditions encountered in space.

References

[1] S. N. Vernov and A. E. Chudakov, “Investigations of cosmic radiation and of the terrestrial corpuscular radiation by means of rockets and satellites,” *Phys.-Uspekhi*, vol. 3, no. 2, pp. 230–250, 1960.

[2] J. A. Van Allen, “The geomagnetically trapped corpuscular radiation,” *J. Geophys. Res.*, vol. 64, no. 11, pp. 1683–1689, 1959.

[3] A. Johnston, *Reliability and radiation effects in compound semiconductors*. World Scientific, 2010.

[4] S. F. Singer, “Trapped albedo theory of the radiation belt,” *Phys. Rev. Lett.*, vol. 1, no. 5, p. 181, 1958.

[5] J. A. Van Allen, C. E. McIlwain, and G. H. Ludwig, “Satellite observations of electrons artificially injected into the geomagnetic field,” *Proc. Natl. Acad. Sci.*, vol. 45, no. 8, pp. 1152–1171, 1959.

[6] D. N. Baker and L. J. Lanzerotti, “Resource letter SW1: Space weather,” *Am. J. Phys.*, 2016.

[7] D. N. Baker, “New Twists in Earth’s Radiation Belts,” *Am. Sci.*, vol. 102, no. 5, p. 374, 2014.

[8] J. C. Foster *et al.*, “Observations of the impenetrable barrier, the plasmapause, and the VLF bubble during the 17 March 2015 storm,” *J. Geophys. Res. Space Phys.*, vol. 121, no. 6, pp. 5537–5548, 2016.

[9] C. Jagadish and S. J. Pearton, *Zinc oxide bulk, thin films and nanostructures: processing, properties, and applications*. Elsevier, 2011.

[10] D. R. Locker and J. M. Meese, “Displacement thresholds in ZnO,” *IEEE Trans. Nucl. Sci.*, vol. 19, no. 6, pp. 237–242, 1972.

[11] L. S. Vlasenko, “Magnetic resonance studies of intrinsic defects in ZnO: Oxygen vacancy,” *Appl. Magn. Reson.*, vol. 39, no. 1–2, pp. 103–111, 2010.

[12] E. A. Kotomin and A. I. Popov, “Radiation-induced point defects in simple oxides,” *Nucl. Instrum. Methods Phys. Res. Sect. B Beam Interact. Mater. At.*, vol. 141, no. 1, pp. 1–15, 1998.

[13] K. Lorenz, E. Alves, E. Wendler, O. Bilani, W. Wesch, and M. Hayes, “Damage formation and annealing at low temperatures in ion implanted ZnO,” *Appl. Phys. Lett.*, vol. 87, no. 19, p. 191904, 2005.

[14] J. A. Van Vechten and S. P. Keller, “Handbook on Semiconductors,” *Vol 3North-Holl. Amst.*, pp. 1–111, 1980.

[15] D. C. Look, J. W. Hemsky, and J. R. Sizelove, “Residual native shallow donor in ZnO,” *Phys. Rev. Lett.*, vol. 82, no. 12, p. 2552, 1999.

[16] D. C. Look, D. C. Reynolds, J. W. Hemsky, R. L. Jones, and J. R. Sizelove, “Production and annealing of electron irradiation damage in ZnO,” *Appl. Phys. Lett.*, vol. 75, no. 6, pp. 811–813, 1999.

[17] S. J. Pearton, F. Ren, E. Patrick, M. E. Law, and A. Y. Polyakov, “Review—Ionizing Radiation Damage Effects on GaN Devices,” *ECS J. Solid State Sci. Technol.*, vol. 5, no. 2, pp. Q35–Q60, Jan. 2016.

[18] I. Jun *et al.*, “Proton nonionizing energy loss (NIEL) for device applications,” *IEEE Trans. Nucl. Sci.*, vol. 50, no. 6, pp. 1924–1928, 2003.

[19] S. R. Messenger *et al.*, “Nonionizing energy loss (NIEL) for heavy ions,” *IEEE Trans. Nucl. Sci.*, vol. 46, no. 6, pp. 1595–1602, 1999.

[20] S. R. Messenger *et al.*, “NIEL for heavy ions: An analytical approach,” *IEEE Trans. Nucl. Sci.*, vol. 50, no. 6, pp. 1919–1923, 2003.

[21] J. R. Srour, C. J. Marshall, and P. W. Marshall, “Review of displacement damage effects in silicon devices,” *IEEE Trans. Nucl. Sci.*, vol. 50, no. 3, pp. 653–670, 2003.

[22] J. R. Srour and J. W. Palko, “A framework for understanding displacement damage mechanisms in irradiated silicon devices,” *IEEE Trans. Nucl. Sci.*, vol. 53, no. 6, pp. 3610–3620, 2006.

[23] M. Featherby, “Advanced Conformal Coating for Radiation Shielding of Microelectronics for Space,” *Maxwell Technol. Microelectron. Co*, 1999.

[24] E. N. Parker, “Shielding space explorers from cosmic rays,” *Space Weather*, vol. 3, no. 8, 2005.

[25] S. S. Orbiter, “SPACE RADIATION EFFECTS ON ELECTRONIC COMPONENTS IN LOW-EARTH ORBIT,” *SPACE*, 1996.

[26] C. Poivey, “RADECS Short Course Section 4 Radiation Hardness Assurance (RHA) for Space Systems,” 2003.

[27] J. W. Wilson *et al.*, “Materials for shielding astronauts from the hazards of space radiations,” *MRS Online Proc. Libr. Arch.*, vol. 551, 1998.

[28] L. Adams, R. Nickson, A. Kelleher, D. G. Millward, D. J. Strobel, and D. Czajkowski, “A dosimetric evaluation of the RADPAK using mono-energetic electrons and protons,” *IEEE Trans. Nucl. Sci.*, vol. 43, no. 3, pp. 1014–1017, 1996.

[29] K. A. LaBel, A. H. Johnston, J. L. Barth, R. A. Reed, and C. E. Barnes, “Emerging radiation hardness assurance (RHA) issues: A NASA approach for space flight programs,” *IEEE Trans. Nucl. Sci.*, vol. 45, no. 6, pp. 2727–2736, 1998.

Chapter 4
Device Processing & Experimental Procedure

4.1 Device Processing Procedure

In this chapter, a summary of the procedure of ZnO thin film transistors (TFTs) fabrication process and the fabrication recipes are presented. Mainly, the theoretical background of the device processing and the detailed description of the primary experimental procedures are described.

4.1.1 Growth

Thin films of ZnO can be grown by various deposition techniques such as thermal oxidation of metallic zinc films [1], spray pyrolysis [2], sol-gel process [3], dip-coating [4], rf-sputtering [5], chemical vapor deposition (CVD) [6], pulsed laser deposition (PLD) [7], and molecular beam epitaxy (MBE) [8]. Each technique has its advantages towards quality ZnO film as well as its drawbacks. For example, MBE, CVD, and PLD methodologies have been able to produce high-quality ZnO films. However, those methods require expensive instrumentation and carefully controlled environment. The rf-magnetron sputtering of ZnO resulted in polycrystalline films with preferred c-axis orientation at higher deposition rate. The growth of defect-free optical quality ZnO films by rf-sputtering is still an issue. The sol-gel, spray pyrolysis, and dip-coating are three different deposition techniques that use solution based ZnO. The advantages of the solution based film deposition are its inexpensive instrumentation and the capability to deposit films on very large substrates. In this dissertation work, the sol-gel process and rf-magnetron sputtering have used to deposit ZnO films. The table 4.1-1 shows a summary of device charactrstics of ZnO TFTs fabricated with various deposition methods.

Table 4.1-1 Summary of device characteristics of ZnO TFT fabricated by various film deposition methods [9].

Technique	Annealing temperature (°C)	Mobility (cm^2 /V.s)	V_{TH} (V)	On/off ratio	I_{sat} (μA)
Ion beam	600-800	0.2-2.5	10-20	10^6	70
Pulsed laser	450	0.031-0.97	-1.0-2.5	10^6	80
So-gel	700-800	0.2	-	10^7	14
rf-magnetron sputtering	Room temperature	20-70	1.8	10^5	1000

4.1.2 Sol-gel Process

1. ZnO Sol-gel Preparation

Zinc acetate dihydrate ($Zn(CH_3COO)_2.2H_2O$), isopropanol (C_3H_8O), and monoethanolamine ($HO(CH_2)_2NH_2$) are used in the ZnO sol-gel preparation process as the source of zinc, solvent, and stabilizer, respectively. To obtain 55 ml of 0.3 mole/cm^3 ZnO sol-gel, 3.58 g of zinc acetate dihydrate from Avantor performance materials Inc. was dissolved in 54 ml of isopropanol with 1 ml of 99% monoethanolamine (MEA) from Alfa Aesar. The solution mixture was stirred by a magnetic stirrer for 2 hours at 70℃ to yield a clear homogenous solution. The reaction between zinc acetate dihydrate and isopropanol initially forms a complex called monoacetate ($[ZnCH_3COO]^+$) [10]. The chemical reaction can be written as follows,

$$Zn(CH_3COO)_2.2H_2O + C_3H_8O \rightarrow [ZnCH_3COO]^+ + [CH_3COO]^- + 2H^+ + 2(OH)^- + C_3H_8O \quad 4.1\text{-}1$$

Low quantity of water in the solution slows the hydrolysis process of Zn cation and disturbs the condensation. Moreover, the MEA further prevent the Zn cation condensation result in milky solution turns into clear solution after adding MEA. Also, the MEA is an amine which increases the pH value of the solution to enhance the ZnO formation. The $[CH_3COO]^-$ and H^+ reacts to form acetic acid (CH_3COOH) and the monoacetate reacts with $(OH)^-$ groups to form zinc hydroxide ($Zn(OH)_2$) at temperatures below 150℃ [10].

$$[ZnCH_3COO]^+ + H^+ + 2OH^- \rightarrow CH_3COOH + Zn(OH)_2 \quad \text{4.1-2}$$

The chemical reaction mechanism and the subproducts of the ZnO sol-gel process were determined by FTIR absorption [10], [11] and transmittance spectra analysis [12]. The clear ZnO sol-gel contains zinc hydroxide and needs to be stored below 100℃ temperatures to avoid partial ZnO formation in the solution.

2. Spin Coating Process

Spin coating is a technique which uses centrifugal force generated by the rotating substrate combined with the surface tension of the solution to deposit thin film (typically ~ 10s of nm) across the surface of the substrate. One of the advantages of the spin coating process is its capability to deposit films on substrates with a broader range of sizes from few mm samples to larger flat panel TV screens. Also, due to the instrumental simplicity, it is easy to integrate into the process. The ability to achieve uniform and consistent film with high spin speeds is another advantage. However, there are few drawbacks in the techniques also such as low throughput due to single substrate deposition compared to batch deposition and high chemical waste. There is only 10% of the chemical used in the process while the rest being flung off during the deposition. The spin coating process involves three steps mechanism as shown in figure 4.1-1.

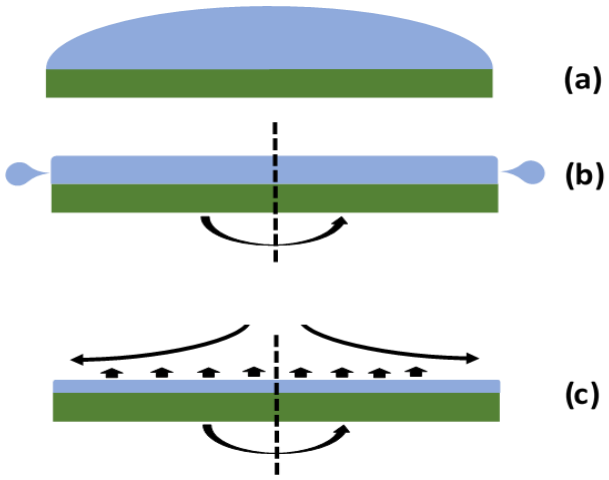

Figure 4.1-1: Schematic diagram of main steps of film deposition in spin coating; (a) sol-gel poured onto the substrate, (b) substrate spins at high speed, and excess solution fling off to sides, and (c) airflow dries the coated film by evaporating excess solvent.

The thickness of the film depends on the parameters such as speed of the spinner, the viscosity of the solution, vapor pressure, temperature and local humidity. The film thickness (t) and the spin-coated film can be obtained by [13],

$$t = k\frac{p^2}{\sqrt{\omega}} \sim \frac{v^{0.4}}{\omega^{0.2}} \qquad 4.1\text{-}3$$

where k is spinner constant, p is the percentage of solids in the solution, ω is the spin speed in rpm, and v is the viscosity of the solution. It is standard practice to determine the required conditions empirically to achieve the desired thickness for a film.

3. ZnO Thin Fim Deposition

The oxidized Si wafers with 100 nm dry oxidized SiO_2 and highly p doped (Boron) Si substrate with <100> orientation and 0.001-0.005 Ω. cm resistivity purchased from University wafers Inc. First, the Si wafer was cleaned with house nitrogen are gun to remove any dust particles

on the surface and attached to the spinning head of the spin coater. It is essential to make sure the Si wafer is well centered and leveled. The ZnO sol-gel solution pours onto an oxidized Si wafer to spin coat a thin film of ZnO. The spin speed was maintained at 3000 rpm for 30 s at room temperature under ambient. Then the coated film was calcined at 285℃ for 5 minutes on a hot plate under ambient. At 285℃ with O_2 from the air, zinc hydroxide decomposes into ZnO as following,

$$Zn(OH)_2 \rightarrow ZnO + H_2O \qquad 4.1\text{-}4$$

The thickness of the film was measured by profilometer and recorded as ~ 25 nm. The spin coating and following calcination process was repeated to obtain the desired ZnO film thickness, e.g., four times repetition to obtain 100 nm ZnO film. Finally, the film was post-annealed at 800℃ in air for 1 hour to achieve polycrystalline phase in deposited ZnO film.

4.1.3 Radio-Frequency Magnetron Sputtering

1. The principle of rf-Magnetron Sputtering

Sputtering systems use energetic ions generated in a plasma to bombard on a target which is the cathode of the setup. Then the ejected atoms from the surface of the target impinge on a substrate (sample) mounted to the anode to form a film [14]. In general, Ar^+ is widely used as the bombarding ions in the plasma. Sputtering systems can be categorized based on the source of plasma discharge; direct-current (DC) sputtering and radio-frequency (rf) sputtering. The rf-sputtering employed rf source to generate a plasma while DC sputtering used DC gaseous discharge. In rf-sputtering system, the cathode and the anode are in series with a blocking capacitor. The blocking capacitor is a part of an impedance matching network to maximize the

power transform from rf source to plasma. The rf source operates at fixed 13.56 MHz. Figure 4.1-2 shows the schematic diagram of an rf-sputtering system.

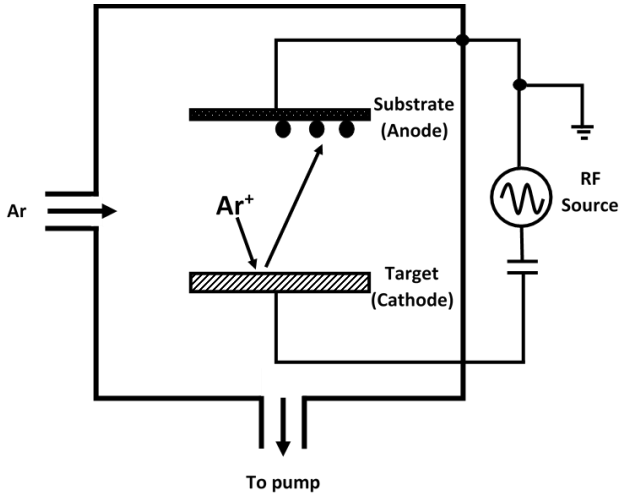

Figure 4.1-2: Schematic diagram of the rf-sputtering system.

The magnetron is a source that intensifies the plasma by using a magnetic field [15]. In the magnetron configuration, a permanent magnet is applied to create magnetic flux parallel to the surface of the target. Therefore, the plasma gets intensified due to the electron trapping took place with the magnetic field near the target surface. This phenomenon results in enhanced sputtering rate in rf-sputtering.

2. ZnO Thin Film Deposition

A 99.9% pure ZnO target from Kurt J. Lesker company was bonded to a copper back plate to enhance the conductivity between the cathode and the target. The diameter and the thickness of the target were 3" and 0.125", respectively. First, the ZnO target was attached to the cathode of the rf-sputtering system. Then the oxidized Si wafers with 100 nm dry oxidized SiO_2 and highly p doped (Boron) Si substrate with <100> orientation and 0.001-0.005 Ω. cm resistivity purchased

from University wafers Inc. loaded and attached to the anode. The parameters were fixed as shown in table 4.1-2 to deposit a thin film of ZnO.

Table 4.1-2 Parameters applied to Denton Discovery 18 rf-magnetron sputtering system

Material	ZnO
Pre-sputtering power (W)	160
Pre-sputtering time (s)	300
Sputtering power (W)	160
Sputtering time (s)	1200
Ar flow rate (sccm)	25
O_2/N_2 flow rate (sccm)	1
Deposition temperature (℃)	RT
Deposition pressure (mTorr)	5
Substrate holder rotation (%)	50

Then the films were post-annealed at 800℃ for 2 hours in air to obtain polycrystalline ZnO film. The thickness of the film was measured as 70 nm by a profilometer.

4.1.3 Cleaning

A clean substrate surface has been recognized as an essential requirement in the fabrication of semiconductor microelectronic devices. The micro-contamination causes 50% of yield loss in integrated circuit fabrication. The contaminants can be introduced to the surface during the storage and fabrication process through process chemicals, tools, and human operations. These impurities can be diffused into the material under high-temperature fabrication process leading to device

failure. Therefore, it is required to remove organic contaminants, metallic impurities, adsorbed molecules and residual species before and after low-temperature processing steps [16], [17]. The surface contaminants can be categorized into three main domains; molecular compounds, ionic materials, and atomic species [18]. Molecular compounds are most likely the organic contaminants from photoresist, solvent residues, storage containers, and metal oxides or hydroxides. Ionic materials such as sodium ions, fluorine ions, and chlorine ions are physically adsorbed to the surface during the processing. The atomic species such as gold and copper are mainly introduced by equipment.

For device fabrication, the ZnO deposited Si wafer was diced into 1×1 cm pieces. Then the individual pieces were chemically cleaned in the order of acetone and methanol in an ultrasonic bath for 5 minutes in each solvent. Finally, the samples were rinsed with deionized (DI) water to remove any remained acetone or methanol residuals. House nitrogen gas blew on the pieces to dry the samples before use for photolithography.

4.1.4 Photolithography

Photolithography is a process that uses light to transfer a pattern into the substrate. The photolithography has its limitation with the minimum feature sizes to be in few μm. Therefore, in most modern device fabrication process, electron beam lithography is employed to obtain smaller feature sizes in nm scale. In this dissertation, the sensitivity of the photolithography was sufficient with required minimum device dimensions. The patterns are initially transferred from the photomask to light-sensitive polymer called photoresist. Chemical or plasma etching is then used to transfer the pattern to the substrate. The typical photolithography process involves multiple steps

to follow to yield the device pattern on the substrate. Figure 4.1-3 illustrates the order of photolithography process.

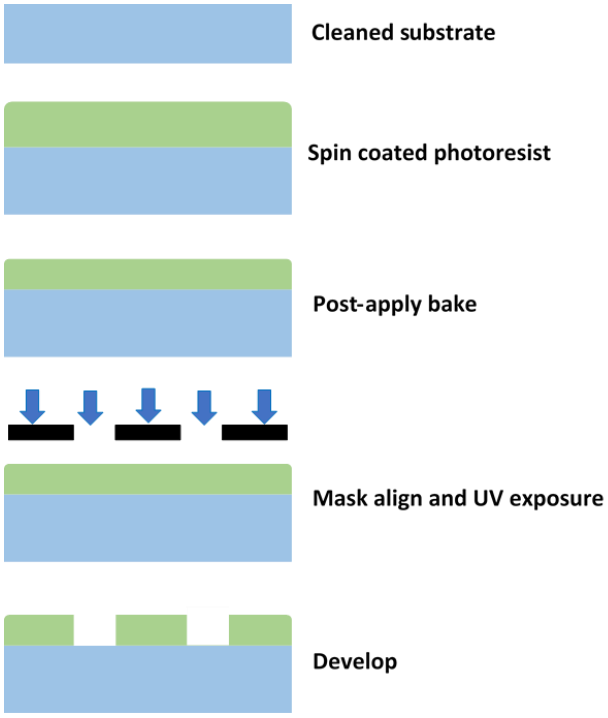

Figure 4.1-3: The order of photolithography process with positive photoresist.

Initially, a diced sample was attached to the center of a mechanical grade 3" Si wafer by acetone-soluble wax. Then the sample-wafer assembly was coated with photoresist (AZ-5414e IR) by spin coating at 4000 rpm for 30 s. Next, the sample was annealed in a process called post-apply bake. During the post-apply bake, the excess solvent in the photoresist layer will be removed. Hence, the thickness of the photoresist film reduces and also the adhesion of the photoresist to the substrate increases. The post-apply bake was carried out in an oven at 110℃ for 1 minute. The final thickness of the photoresist layer was approximately 1.4 µm. There are two types of photoresists; positive photoresist (e.g., AZ-5414e-IR) and negative photoresist (e.g., AZ-nLOF 2070). The positive photoresist becomes more soluble when it exposed to UV light, and negative photoresist gets harden with UV exposure. The selection of the type of photoresist depends on the

kind of photomask used to transfer the pattern. Figure 4.1-4 indicates the use of positive and negative photoresists.

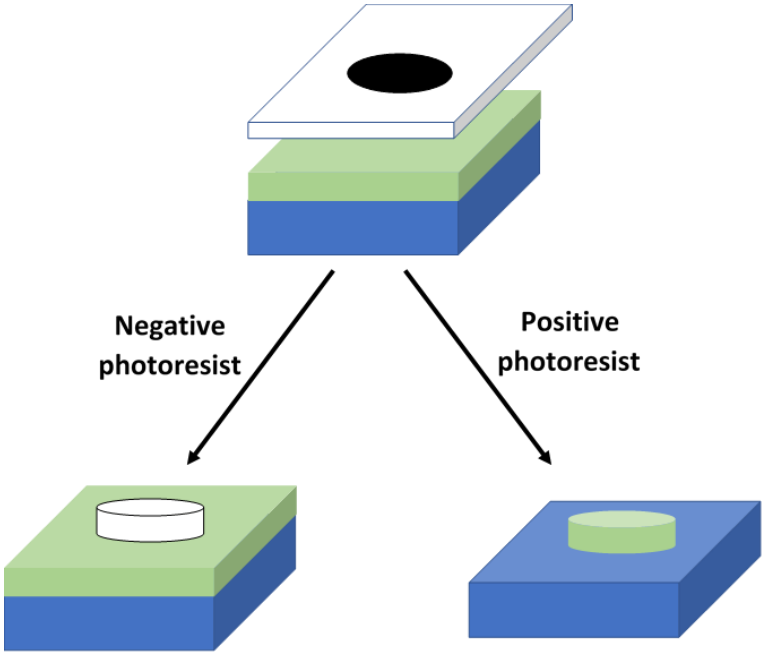

Figure 4.1-4: Illustration of pattern transfer mechanism of positive and negative photoresist.

After the post-apply bake, the sample was mounted to sample holder of the mask aligner to initiate photolithography process. A Karl Suss MJB3 UV400 mask aligner equipped with a 160W Hg lamp as the UV source was used for the photolithography. A photomask which is a quartz plate patterned with chromium was mounted above the sample. Then the sample and the pattern on the photomask were aligned by using the optical microscope attached to the mask aligner. After that, the sample was exposed to UV light for 30 s. Depending on the type of photomask and the photoresist, it is required to do post-exposure bake. Clear field photomask has an opaque pattern on a transparent background, and dark field photomask has a transparent pattern on an opaque background. AZ-5214e photoresist has a capability of image reversal (IR). A crosslinking (hardening) agent form in the photoresist when the post-exposure bake is applied at

110℃ for 1 minute. A direct Re-exposure of UV (flood exposure) to the post-exposure baked sample makes photoresist harden in areas where a higher dose of UV absorbed than the lower dose, results in the image reversal. Figure 4.1-5 illustrates the image reversal process with post-exposure bake and UV flood exposure.

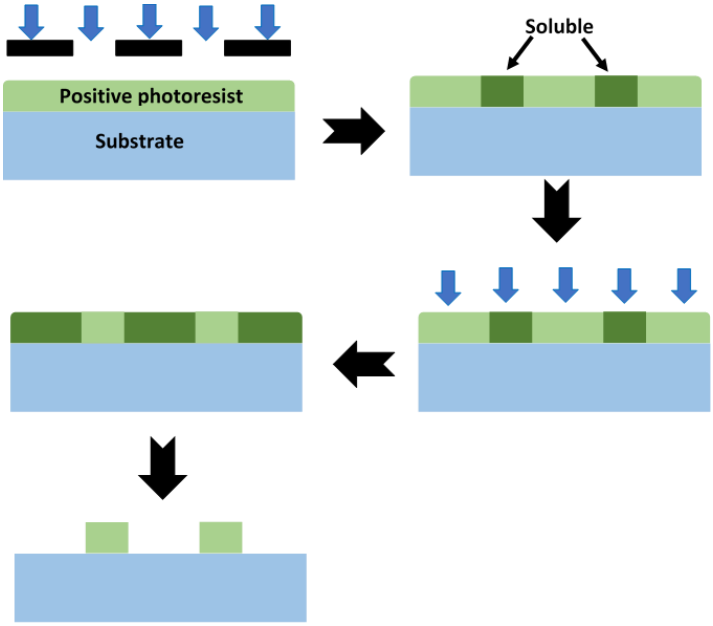

Figure 4.1-5: Illustration of image reversal process with AZ-5214e-IR (positive) photoresist.

Then the sample was developed in AZ 726 MIF developer to dissolve the soluble area of the photoresist film to develop the negative image of the pattern on the substrate. The shape of the transferred pattern and the linewidth control depend on the reaction between the developer and resist. In this work, the puddle development technique, which spins the substrate to spread developer efficiently was used develop the pattern on the photoresist. When the developing time elapsed, the additional developer was rinsed with DI water. It is essential to employ the rinsing immediately after development to avoid over developed patterns.

The spatial resolution of the photolithography process defines the minimum feature size (MFS) of the pattern. The MFS depends on the optical element and the wavelength of the light as follows [19],

$$resolution = \frac{\lambda}{NA} \quad 4.1\text{-}5$$

where λ is the wavelength of the exposure light, and *NA* is the numerical aperture.

4.1.5 Metal Deposition

1. Direct-Current (DC) Magnetron Sputtering

Sputtering is a process in which material is removed from a target at the cathode by bombarding energetic ions from the plasma and the ejected materials transport to the surface of the sample to deposit [20]. In a DC sputtering system, plasma is created with DC voltage applied between the cathode and the anode. Argon (Ar) is used as the regular feed gas to generate plasma with ions (Ar^+). The magnetron configuration enhances the intensity of the plasma by increasing energetic electron density near the target. Therefore, a DC magnetron sputtering system can yield higher sputtering rate compared to ordinary parallel electrode DC sputtering. Figure 4.1-6 is a schematic diagram of a DC magnetron sputtering system and elaborated metal deposition mechanism.

In the DC magnetron sputtering system in Leach science center of Auburn University, a high vacuum of 3×10^{-7} Torr can be achieved by a vacuum system coupled with roughing pump and turbopump. It consists of four 2" diameter magnetron sputtering guns and maximum DC power of 1000 W. The sample holder plate is located right above the sputtering target. The sample holder plate can be mechanically rotated once the vacuum chamber is closed. Therefore, it is plausible to

deposit four different metals on the same or several samples successively without venting the vacuum.

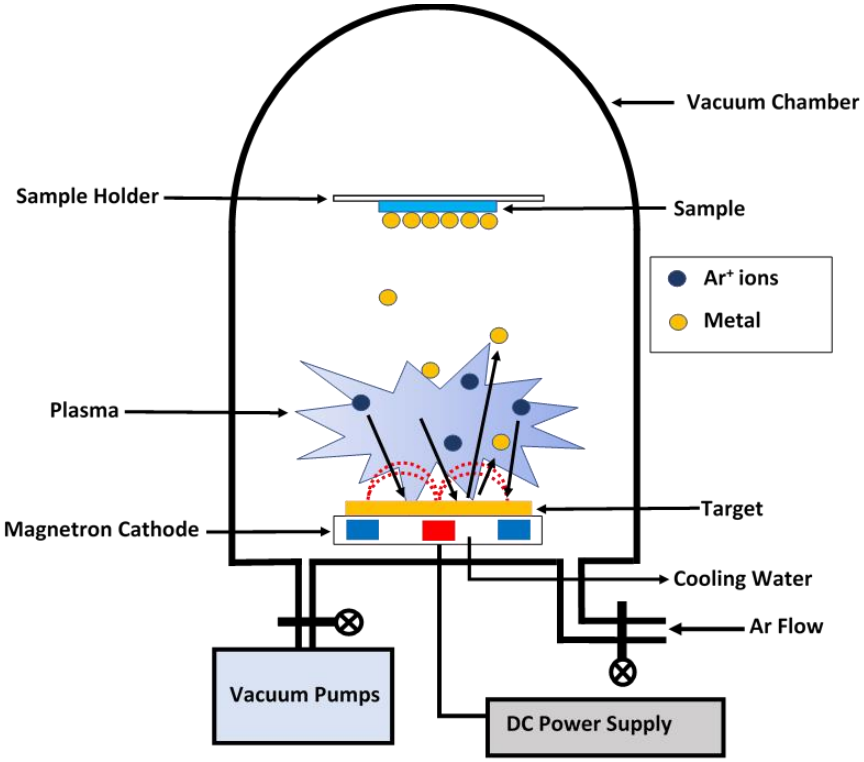

Figure 4.1-6: Schematic diagram of the DC magnetron sputtering system and the metal deposition process.

First, the 2" diameter sputtering target was attached to the sputtering gun and placed a chimney to keep the ejected material form wide spreading. Then the photolithographically patterned samples were attached to a 3" Si wafer and then mounted to the sample holder plate. The vacuum chamber was vented with the pumping assembly until it reaches to 3×10^{-7} Torr. During the sputtering, Ar was flowing into the chamber at the rate of 95 sccm (standard cubic centimeter per minute), and the pressure of the chamber was maintained at 17 mTorr. The samples were at room temperature during the deposition. A summary of parameters to be fixed for each metal deposition was given in table 4.1-3.

Table 4.1-3 Summary of sputtering parameters for different metal depositions

Metal	Voltage (V)	Current (A)	Pre-sputter time (s)	Sputter time (s)	Film thickness (nm)
Ti	290	0.25	180	360	100
Pd	380	0.25	40	120	140
Ir	490	0.25	60	20	15
$Ni_{93\%}$ $V_{7\%}$	340	0.25	120	240	40

The pre-sputter time is required to remove any impurities on the target surface before depositing the metal on samples. During the pre-sputter, the samples were kept away from the sputter target by mechanically rotating the sample holder. When the sputtering time is elapsed, the samples were taken out after venting the vacuum in the sputtering chamber.

2. Thermal Evaporation

Thermal evaporation method required to heat metal to the point of vaporization, and then the evaporated metal deposited on the surface of the sample. A higher vacuum is essential to control the composition of the deposited metal in thermal evaporation technique [21].

Figure 4.1-7 shows the schematic diagram of the thermal evaporation system in this dissertation work to deposit Aluminum (Al). The pressure of the chamber was maintained at approximately 5×10^{-6} Torr by vacuum system equipped with roughing pump and diffusion pump. The 99.999% aluminum pallets (1/8"×1/8") from Kurt J. Lesker company were used in the metal evaporation process. Metal evaporation was done by heating an alumina-coated tungsten bucket to 1500℃. The relationship between the deposited metal thickness and the applied DC bias and

evaporation time were empirically determined. Thermal evaporation at 60 W for 4 minutes after 1-minute pre-evaporation yield approximately 140 nm Al layer. Aluminum deposition by DC sputtering was time-consuming due to its low deposition rate, and it was required to pause the sputtering process frequently to avoid overheating the target. In contrast, thermal evaporation was convenient and faster than DC sputtering. However, one of the drawbacks in thermal evaporation is its lack of thickness control. It was identified that the reuse of heating bucket causes the problem of the thicker film than expected. The reason was that the pre-deposited Al on the heating bucket evaporated in addition to the added Al pallets, thereby result in thicker Al deposited on the sample. This problem can be avoided by using a new heating bucket and also with a more sophisticated solution which is assembling a mass flow detector to monitor the deposited film thickness.

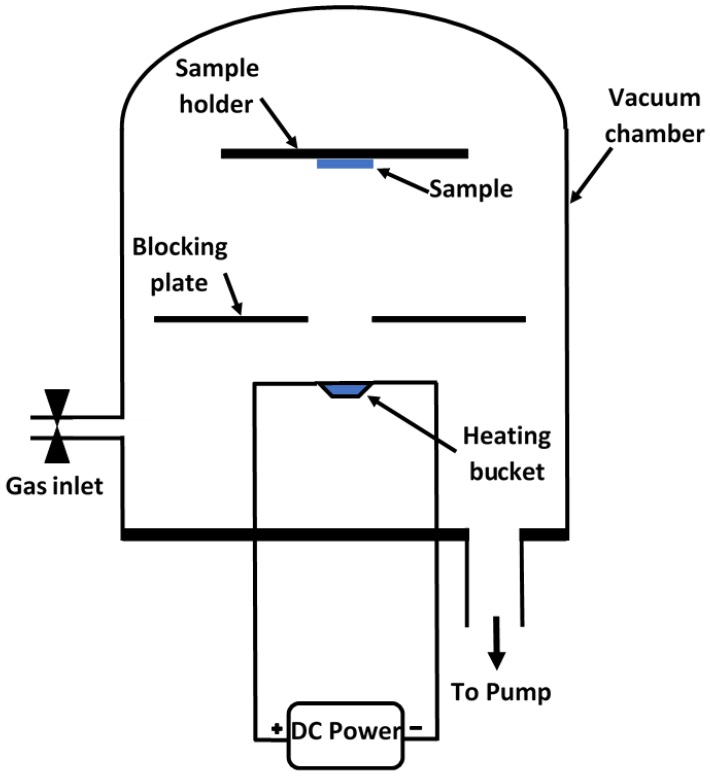

Figure 4.1-7: Schematic diagram of the thermal evaporation system.

4.1.6 Lift-off

Lift-off is a process that removes the excess metal deposited on the substrate by stripping photoresist underneath. In this dissertation work, wet chemical lift-off was performed with acetone to dissolve photoresist and lift-off the excess metal to pattern metal contacts on the substrate. The duration of the lift-off process depends on several factors such as the thickness of the metal film, type of photoresist, post-apply bake temperature, UV exposure dose, and quality of the photoresist layer.

4.1.7 Rapid Thermal Annealing (RTA)

Rapid thermal annealing (RTA) is mainly employed to activate implanted dopants and yield excellent ohmic contact by interfacial diffusion of metal and semiconductor. In this dissertation, RTA was used to obtain good ohmic behavior for deposited Ti/Pd and Ti/Ir contacts. RTA treatment at 300℃ for 1 minute under N_2 ambient could yield contact resistivity as low as $3.34\times10^{-4}\ \Omega\ cm^2$ and $1.68\times10^{-5}\ \Omega\ cm^2$ for Ti/Ir and Ti/Pd contacts on ZnO, respectively. At 300℃ oxygen from ZnO diffuse into Ti to form TiO generating oxygen vacancies (V_0) in ZnO [22]. The Gibbs free energy per mole of oxygen for TiO_2 ($\Delta G_{600\ K}$=-833.972 kJ/mole) is lower than that of ZnO ($\Delta G_{600\ K}$=-290.452 kJ/mole) [23]. Therefore, the formation of TiO is preferable at 300℃ RTA. The created V_0 at the ZnO/Ti interface act as shallow donors to enhance the conduction [24]. The RTA system consists of a vacuum chamber, an infrared optical pyrometer, and a rheostat to control the current. Figure 4.1-8 shows the schematic diagram of the RTA system.

The RTA system used in this work contains two carbon stripes separated by 2” as the heating element. First, the samples were placed in a carbon crucible and then the crucible was mounted on the carbon strip. The infrared optical pyrometer located right above the vacuum

chamber focused to the carbon stripe adjacent to the sample. Then the vacuum chamber was vented to achieve 2×10^{-7} Torr by the use of a roughing pump and then a diffusion pump. After that, the chamber was filled with high purity N_2 and brought the chamber pressure to atmospheric pressure. The carbon stripe was heated to obtain 300℃ by carefully adjusting the input power. During the 1 minute RTA under N_2 ambient, the temperature of the sample was maintained at 300℃. Right after the annealing time elapsed; the samples were cooled down to the room temperature rapidly with the aid of a mechanical fan located closer to the vacuum chamber.

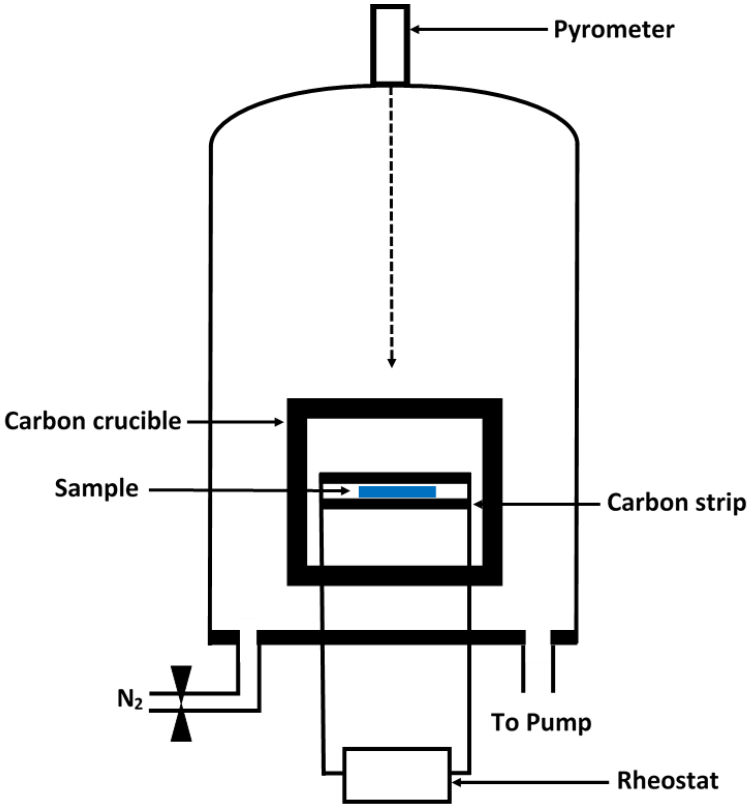

Figure 4.1-8: Schematic diagram of rapid thermal annealing (RTA) system.

The back-gated ZnO TFTs were prepared for electrical measurements by attaching a gold-plated ceramic plate to the back of the Si substrate by conducting silver paste. The back of the Si substrate was scratched out to remove natural oxide to access conducting Si substrate which

employed as the gate electrode in the ZnO TFTs. The attached gold plate was used to land probe to the gate electrode. Figure 4.1-9 shows a picture of the fabricated ZnO TFTs for this dissertation work.

4.2 Experimental Procedure

In this work, ZnO film analysis and characterizations were performed by micro-Raman spectroscopy, photoluminescence, and X-ray diffraction spectroscopy. The current-voltage (I-V) and capacitance-voltage (C-V) measurements were carried out as electrical characterizations of ZnO TFTs. The proton irradiation experiment on ZnO TFTs and ZnO films were done by the 2MV Tandem source Pelletron accelerator in Leach science center, Auburn University.

4.2.1 Micro-Raman Spectroscopy

Mainly Raman spectrometer consists of 4 components as listed as follows;

1) Excitation source
2) Sample holder and microscope
3) Wavelength selector
4) Detection and computer controlled processing system.

The laser has been used as an excitation source of modern Raman spectroscopy due to the ideal characteristics of large peak power in the order of MW, monochromatic beam with weak spurious lines, smaller beam diameter, and the availability of wide range of wavelength. The He-Cd laser provides blue (441.563 nm) and UV (325 nm) laser lines with average power 40 and 10 MW, respectively. The Rayleigh and anti-stokes can be eliminated by using edge filters. The Raman scattering is an inherently weak signal. Therefore, the laser beam needs to focus on the sample and collect the scattered beam from the sample. The laser excitation and scattered beam collection

from the sample can be done with several optical configurations such as 90° and 180° scattering geometries in the lens system. The preliminary focusing of the incident laser beam on the sample is done by an optical microscope. During the sample focusing by the optical microscope, the laser beam was blocked by a shutter system. Once the sample focus is done, the shutter was opened and the adjustable mirrors were moved to focus the laser beam on the sample. The grating monochromators are used as wavelength selectors. A selective wavelength is used in Raman spectroscopy to obtain better resolution and accordingly to the scanning range. The 2400 lines/mm grating facilitates wider scan range (200-750 nm) while 3600 lines/mm provides better resolution compared to 2400 lines/mm. The charge-coupled detector (CCD) has used as the detection device in Raman spectrometer. The CCD is a silicon-based arranged array of photosensitive elements. When a photon strikes on each pixel, it stored as a small charge. Therefore, each pixel store charges as a function of the stricken photon on individual pixel. The low readout noise in CCD is an advantage compared to other multi-channel detectors. Hence, the signal intensification for weak Raman signal is unnecessary with CCD. A wider range of wavelengths for detection can be obtain with the use of CCD as well.

Our custom-made Raman spectrometer consists of He-Cd laser from Kimmon Koha Co.Ltd., which excites 441.563 and 325 nm laser lines. The diameter of the laser beam measured as 5-10 μm after focused on the sample by the optical microscope. An edge filter used to filter out Rayleigh and anti-stock signals before entering to the Jobin Yvon spectrometer. The CCD with 2048×512 pixel array used to detect the Raman signal with higher precision. The scan with 2400 lines/mm grating provided 1 cm^{-1} resolution. The schematics diagram of Raman spectroscopic system is presented in figure 3.1-3.

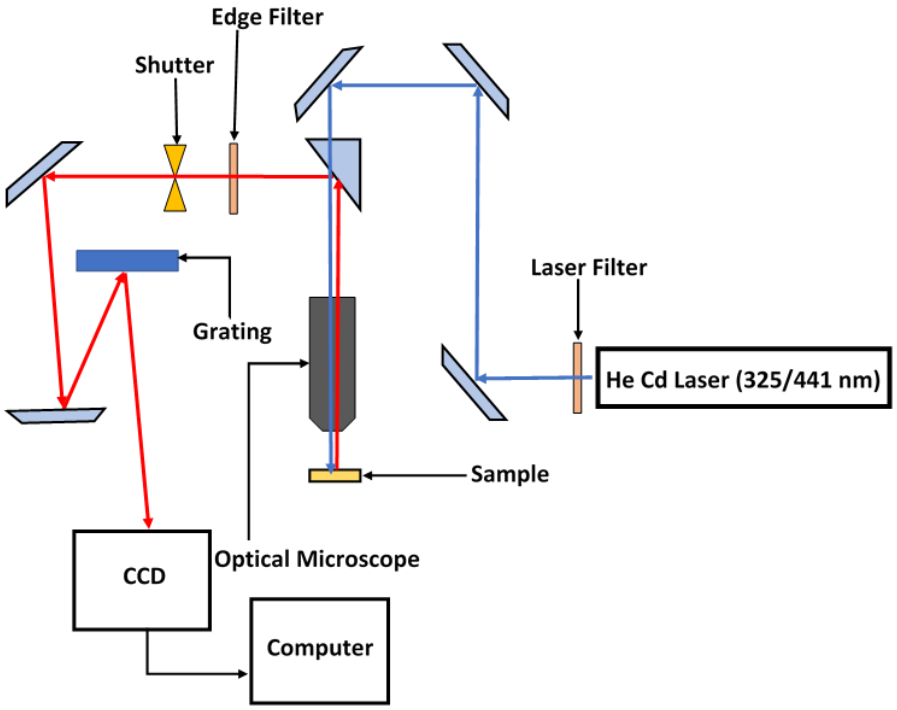

Figure 4.2-1: Schematic diagram of micro-Raman spectrometer.

4.2.2 Photoluminescence (PL)

In photoluminescence, ZnO films were exposed to 325 nm laser line generated by He-Cd laser from Kimmon Koha Co.Ltd. The PL spectra were dispersed with 2400 lines/mm grating. The PL measurements were performed at room temperature. The penetration depth of 325 nm laser into ZnO layer is determined as around 60 nm. Therefore, PL spectra represent the characteristics of bulk ZnO. The variation in the intensity of the UV peak and the broad visible luminescence peak would provide the insight into the crystal quality and the defect concentration in the sub-bandgap region of ZnO. The blue, green and yellow luminescence observed in PL spectra are produced by the electron transitions from neutral oxygen vacancy to valence band (~2.8 eV), singly ionized oxygen vacancy to valance band (~2.5 eV), and delocalized electron near conduction band

recombination with doubly ionized oxygen vacancy (~2.2 eV), respectively [25]–[27]. The UV peak observed in PL spectrum is caused by the band to band radiative recombination in ZnO. Figure 4.2-2 shows the comparison of PL spectra of ZnO films deposited by the sol-gel method and the rf-magnetron sputtering.

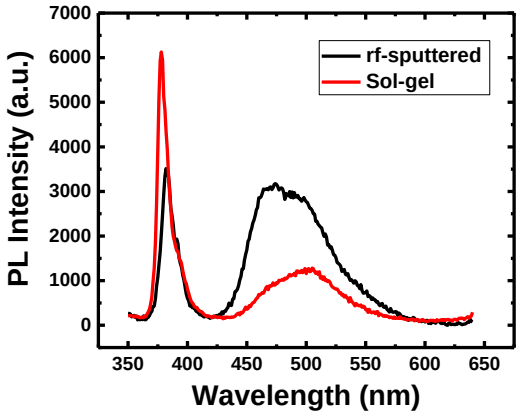

Figure 4.2-2: The PL spectra of ZnO films deposited by sol-gel spin coating and rf-magnetron sputtering.

As can be seen in figure 4.2-2, the near band edge UV emission is dominated over deep level emission in sub-bandgap region for ZnO. Sol-gel derived ZnO films show high intensity in UV peak compared to visible luminescence. Visible luminescence in PL spectra can be attributed to native defects such as oxygen vacancies and other impurities introduced during the film deposition. Therefore, the high intensity in visible luminescence in rf-sputtered ZnO indicates high level of native defects and impurities in film. Since sol-gel ZnO shows higher I_{UV}/I_{Vis} compared to rf-sputtered films, sol-gel derived ZnO films are much favorable for optoelectronic applications.

4.2.3 X-Ray Diffraction Spectroscopy (XRD)

The XRD analysis of ZnO films was employed to determine the crystal quality of the ZnO. The Bruker D2 Phaser XRD system used in this dissertation work is shown in figure 4.2-3.

Figure 4.2-3: Picture of Bruker D2 Phaser XRD system in the department of Geosciences, Auburn University.

The XRD analyzer consists of a Lynxeye detector and a Cu shutter tube. The X-ray was generated with 300 W power, and the wavelength was 1.54184 $\dot{A}$. Sample was rotated at a speed of 20 rpm during the data collection to obtain a spectrum for the sample. The sample scan was performed in continuous PSD mode with 0.5 s scan time and 0.02^0 2θ increment for the scan range. It is important to use the same procedure to load the sample to the XRD chamber to avoid the spurious parallel shift in XRD spectra. For example, if the upper surface of the sample is elevated compared to the surface of the sample holder, the XRD peaks tend to shift in higher 2θ direction. When the upper surface of the sample is located below the surface of the sample holder, the XRD peaks shift in lower 2θ direction. Therefore, the shift in XRD peaks due to stress and strain in ZnO crystal structure can be shadowed by the spurious shift in XRD spectra.

The grain size of polycrystalline ZnO can be extracted from XRD data by using Debye-Scherrer relationship [28].

$$D = \frac{k\lambda}{B\cos\theta} \quad \text{4.2-1}$$

where, D is the grain size, k is 0.94, λ is the wavelength of x-ray, B is the full width at half-maximum (FWHM) of (0002) peak in radians, and θ is the Bragg angle for the (0002) peak. For hexagonal structures, the biaxial stress of the film along c-axis can be obtained by [29],

$$\sigma_{film} = \frac{2C_{13}^2 - C_{33}(C_{11}+C_{12})}{C_{13}} . \varepsilon_z \quad \text{4.2-2}$$

where, C_{11}= 209.7 GPa, C_{12}= 121.1 GPa, C_{13}= 105.1 GPa, and C_{33}= 210.9 GPa are the elastic stiffness constants for ZnO [30]. The ε_z is strain in the lattice along c-axis, which can be deduced by [29],

$$\varepsilon_z = \frac{(C - C_0)}{C_0} \quad \text{4.2-3}$$

where C and C_0 are the strained and strain-free lattice parameters of ZnO, respectively. The strain-free lattice parameter (C_0) was obtained from a joint committee of powder diffraction standards (JCPD) card 75-0576 card. The lattice parameter for (002) peak of ZnO film was calculated by the following equation [31];

$$\frac{1}{d_{(hkl)}^2} = \frac{4}{3}\left[\frac{h^2+hk+k^2}{a^2}\right] + \frac{l^2}{c^2} \quad \text{4.2-4}$$

where a and c are lattice parameters of ZnO. The $d_{(002)}$ can be obtained by Bragg's equation;

$$d_{(002)} = \frac{\lambda}{2\sin\theta_{(002)}} \quad \text{4.2-5}$$

where, λ is the wavelength of x-ray and $\theta_{(002)}$ is the Bragg angle for (002) peak. Figure 4.2-4 shows the XRD spectra for ZnO films deposited by sol-gel spin coating and rf-mangetron sputtering.

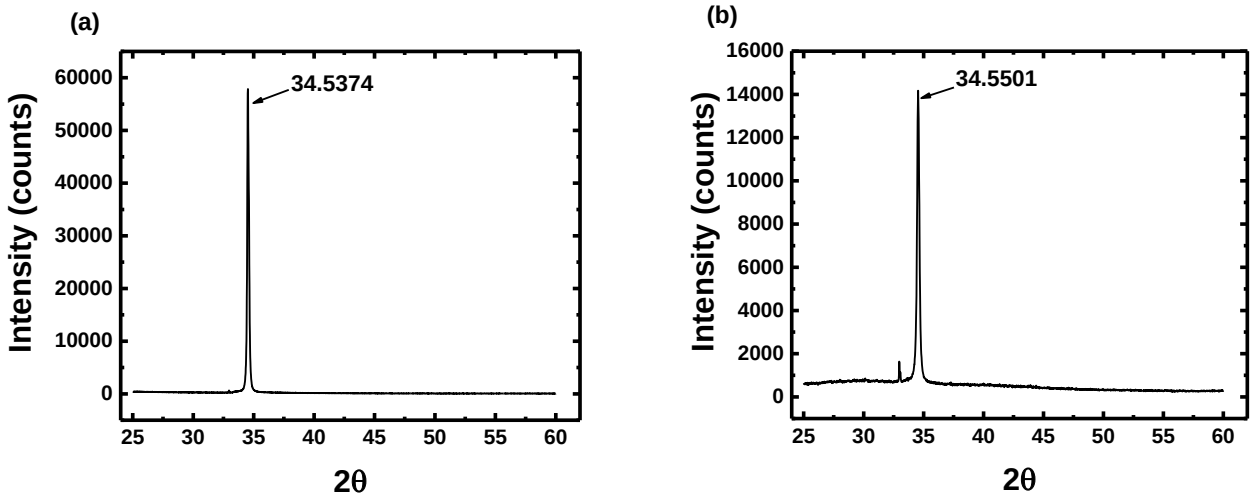

Figure 4.2-4: XRD spectra of ZnO film deposited by (a) sol-gel spin coating, and (b) rf-magnetron sputtering.

The calculalated biaxial stress of the ZnO film along c-axis is summarized in table 4.2-1.

Table 4.2-1 Calculated biaxial stress of the ZnO film along the c-axis.

Deposition technique	σ_{film} (GPa)
Sol-gel	1.469
rf-magnetron sputtering	1.630

4.2.4 Current-Voltage (I-V) and Capacitance-Voltage (C-V) Measurements

I-V measurements for output characterizations and transfer characterizations were done using an H-100 Signatone probe station equipped with Keithley 6517 voltage source. Typically all the electrical measurements were performed at room temperature and in dark environment.

However, in specially designed experiments which required a controlled environment, a cryogenic manipulated probe station from Advanced Research Systems equipped with Keithley 4200-SCS parameter analyzer was used. Low-frequency C-V measurements for the capacitance of vertical $ZnO/SiO_2/Si$ MOS structure were done using an H-100 Signatone probe station equipped with Keithley 590CV analyzer. The C-V analyses were also performed at room temperature and in dark environment. Calibrated cables with Signatone S-725 micropositioners were used in electrical measurements to increase the signal to noise ratio. The electrical measurement data were extracted from a Labview programme written to collect output, transfer characteristics, and capacitance.

4.2.5 Proton Irradiation

The proton irradiation process for data reported in chapter 6 and appendix II performed by a 2 MV Tandem source Pelletron accelerator in Leach science center, Auburn University. Figure 4.2-5 shows the schematic diagram of the Pelletron accelerator.

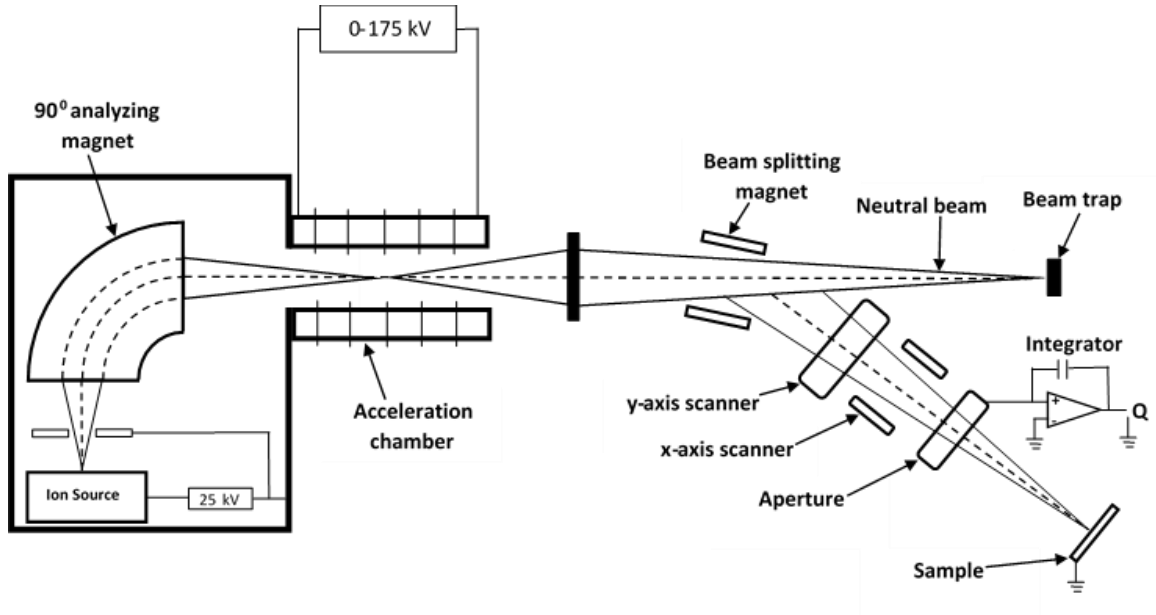

Figure 4.2-5: Schematic diagram of the particle accelerator.

Protons were generated by stripping an electron from hydrogen with nitrogen. Then the protons were accelerated to gain 200 keV energy. The energetic proton beam was guided towards the sample mounted at the end of the beam line with a beam splitting magnet. The sample was under the vacuum with a pressure of 5×10^{-6} Torr, and cooling water was flowing through the sample holder to keep the sample at room temperature during the irradiation. The fluence of the proton radiation was carefully maintained at 1.0×10^{14} protons/cm^2 by monitoring the beam current throughout the irradiation process. The proton beam was scanned over a 6.3 cm diameter circular aperture area with a scan rate of 64 Hz in the y-axis and 517 Hz in the x-axis. Four isolated Faraday cups located on the aperture, 4" apart from each other were monitored the proton beam current. Equal current readout in all four Faraday cups indicates a uniform distribution of proton across the sample. The Fluence of the proton beam was fixed with beam current and the exposure time as following,

$$Time = \frac{q\times fluence\times A}{I} \qquad 4.2\text{-}6$$

where q is the charge of a proton, A is the area of the aperture, and I is the beam current. The fluence of 1.0×10^{14} proton/cm^2 was obtained with 781 s irradiation time and 700 nA current. Moreover, a larger movable Faraday cup located 8" upstream of the sample was used to monitor beam current intermittently to confirm uniform proton irradiation over the sample. The ZnO samples were mounted to the sample holder with conducting carbon tape. Therefore, the gate electrodes of ZnO TFTs were grounded during the proton irradiation.

References

[1] S. J. Chen *et al.*, “High-quality ZnO thin films prepared by two-step thermal oxidation of the metallic Zn,” *J. Cryst. Growth*, vol. 240, no. 3, pp. 467–472, 2002.

[2] R. Ayouchi, F. Martin, D. Leinen, and J. R. Ramos-Barrado, “Growth of pure ZnO thin films prepared by chemical spray pyrolysis on silicon,” *J. Cryst. Growth*, vol. 247, no. 3, pp. 497–504, 2003.

[3] W. Tang and D. C. Cameron, “Aluminum-doped zinc oxide transparent conductors deposited by the sol-gel process,” *Thin Solid Films*, vol. 238, no. 1, pp. 83–87, 1994.

[4] Y. Takahashi, M. Kanamori, A. Kondoh, H. Minoura, and Y. Ohya, “Photoconductivity of Ultrathin Zinc Oxide Films,” *Jpn. J. Appl. Phys.*, vol. 33, no. 12R, p. 6611, Dec. 1994.

[5] V. Gupta and A. Mansingh, “Influence of postdeposition annealing on the structural and optical properties of sputtered zinc oxide film,” *J. Appl. Phys.*, vol. 80, no. 2, pp. 1063–1073, 1996.

[6] M. Aoki, K. Tada, T. Murai, and T. Inoue, “A new technique for the vapour phase epitaxial growth of ZnO as a guided-wave optical material,” *Thin Solid Films*, vol. 83, no. 2, pp. 283–288, 1981.

[7] X. W. Sun and H. S. Kwok, “Pulsed laser deposition of silicate phosphor thin films,” *Appl. Phys. Mater. Sci. Process.*, vol. 69, no. 7, pp. S39–S43, 1999.

[8] H.-B. Kang, K. Nakamura, S.-H. Lim, and D. Shindo, “Epitaxial growth of ZnO films on (0001) sapphire at low temperatures by electron cyclotron resonance-assisted molecular beam epitaxy and their microstructural characterizations,” *Jpn. J. Appl. Phys.*, vol. 37, no. 3R, p. 781, 1998.

[9] E. Fortunato *et al.*, “Recent advances in ZnO transparent thin film transistors,” *Thin Solid Films*, vol. 487, no. 1–2, pp. 205–211, 2005.

[10] A. E. Jimenez-Gonzalez, J. A. S. Urueta, and R. Suarez-Parra, “Optical and electrical characteristics of aluminum-doped ZnO thin films prepared by solgel technique,” *J. Cryst. Growth*, vol. 192, no. 3, pp. 430–438, 1998.

[11] S. Bandyopadhyay, G. K. Paul, R. Roy, S. K. Sen, and S. Sen, “Study of structural and electrical properties of grain-boundary modified ZnO films prepared by sol–gel technique,” *Mater. Chem. Phys.*, vol. 74, no. 1, pp. 83–91, 2002.

[12] H. Li *et al.*, “Sol–gel preparation of transparent zinc oxide films with highly preferential crystal orientation,” *Vacuum*, vol. 77, no. 1, pp. 57–62, 2004.

[13] S. A. Campbell, *The science and engineering of microelectronic fabrication*. Oxford University Press, USA, 1996.

[14] J. E. Mahan, “Physical vapor deposition of thin films,” *Phys. Vap. Depos. Thin Films John E Mahan Pp 336 ISBN 0-471-33001-9 Wiley-VCH January 2000*, p. 336, 2000.

[15] D. L. Smith, “Thin-film deposition: principles and practice. 1995,” *N. Y. Tc McGraw-Hill*.

[16] M. K. Sanganeria *et al.*, “Ultrahigh Vacuum Rapid Thermal Chemical Vapor Deposition of Epitaxial Silicon onto (100) Silicon I. The Influence of Prebake on (Epitaxy/Substrate) Interfacial Oxygen and Carbon Levels,” *J. Electrochem. Soc.*, vol. 142, no. 11, pp. 3961–3969, 1995.

[17] G. R. Srinivasan, “Recent advances in silicon epitaxy and its application to high performance integrated circuits,” *J. Cryst. Growth*, vol. 70, no. 1–2, pp. 201–217, 1984.

[18] W. Kern, “The evolution of silicon wafer cleaning technology,” *J. Electrochem. Soc.*, vol. 137, no. 6, pp. 1887–1892, 1990.

[19] M. Rothschild *et al.*, “Recent trends in optical lithography,” *Linc. Lab. J.*, vol. 14, no. 2, pp. 221–236, 2003.

[20] A. Elshabini, A. A. Elshabini-Riad, and F. D. Barlow, *Thin film technology handbook*. McGraw-Hill Professional, 1998.

[21] R. C. Jaeger, G. W. Neudeck, and R. F. Pierret, *Introduction to Microelectronic Fabrication, 2002*. Prentice Hall.

[22] S. Y. Kim *et al.*, “Low-resistance Ti/Al ohmic contact on undoped ZnO,” *J. Electron. Mater.*, vol. 31, no. 8, pp. 868–871, 2002.

[23] I. Barin and G. Platzki, *Thermochemical data of pure substances*, vol. 304. Wiley Online Library, 1989.

[24] A. Pöppl and G. Völkel, "ESR and Photo-ESR Investigations of Zinc Vacancies and Interstitial Oxygen Ions in Undoped ZnO Ceramics," *Phys. Status Solidi A*, vol. 125, no. 2, pp. 571–581, 1991.

[25] K. Vanheusden, W. L. Warren, C. H. Seager, D. R. Tallant, J. A. Voigt, and B. E. Gnade, "Mechanisms behind green photoluminescence in ZnO phosphor powders," *J. Appl. Phys.*, vol. 79, no. 10, pp. 7983–7990, 1996.

[26] H. S. Kang, J. S. Kang, J. W. Kim, and S. Y. Lee, "Annealing effect on the property of ultraviolet and green emissions of ZnO thin films," *J. Appl. Phys.*, vol. 95, no. 3, pp. 1246–1250, 2004.

[27] Y.-J. Lin, C.-L. Tsai, Y.-M. Lu, and C.-J. Liu, "Optical and electrical properties of undoped ZnO films," *J. Appl. Phys.*, vol. 99, no. 9, p. 093501, 2006.

[28] L. V. Azároff and R. J. Donahue, *Laboratory experiments in x-ray crystallography*. McGraw-Hill, 1969.

[29] M. K. Puchert, P. Y. Timbrell, and R. N. Lamb, "Postdeposition annealing of radio frequency magnetron sputtered ZnO films," *J. Vac. Sci. Technol. Vac. Surf. Films*, vol. 14, no. 4, pp. 2220–2230, 1996.

[30] A. M. Hellwege and K. H. Hellwege, *Numerical Data and Functional Relationships in Science and Technology: Nuclear Physics and Technology. New Series, Group I.* Springer-Verlag, 1961.

[31] S. R. Stock and B. D. Cullity, "Elements of X-ray Diffraction," *Up. Saddle River NJ*, 2001.

Chapter 4
Device Processing & Experimental Procedure

4.1 Device Processing Procedure

In this chapter, a summary of the procedure of ZnO thin film transistors (TFTs) fabrication process and the fabrication recipes are presented. Mainly, the theoretical background of the device processing and the detailed description of the primary experimental procedures are described.

4.1.1 Growth

Thin films of ZnO can be grown by various deposition techniques such as thermal oxidation of metallic zinc films [1], spray pyrolysis [2], sol-gel process [3], dip-coating [4], rf-sputtering [5], chemical vapor deposition (CVD) [6], pulsed laser deposition (PLD) [7], and molecular beam epitaxy (MBE) [8]. Each technique has its advantages towards quality ZnO film as well as its drawbacks. For example, MBE, CVD, and PLD methodologies have been able to produce high-quality ZnO films. However, those methods require expensive instrumentation and carefully controlled environment. The rf-magnetron sputtering of ZnO resulted in polycrystalline films with preferred c-axis orientation at higher deposition rate. The growth of defect-free optical quality ZnO films by rf-sputtering is still an issue. The sol-gel, spray pyrolysis, and dip-coating are three different deposition techniques that use solution based ZnO. The advantages of the solution based film deposition are its inexpensive instrumentation and the capability to deposit films on very large substrates. In this dissertation work, the sol-gel process and rf-magnetron sputtering have used to deposit ZnO films. The table 4.1-1 shows a summary of device charactrstics of ZnO TFTs fabricated with various deposition methods.

Table 4.1-1 Summary of device characteristics of ZnO TFT fabricated by various film deposition methods [9].

Technique	Annealing temperature (°C)	Mobility (cm^2 /V.s)	V_{TH} (V)	On/off ratio	I_{sat} (μA)
Ion beam	600-800	0.2-2.5	10-20	10^6	70
Pulsed laser	450	0.031-0.97	-1.0-2.5	10^6	80
So-gel	700-800	0.2	-	10^7	14
rf-magnetron sputtering	Room temperature	20-70	1.8	10^5	1000

4.1.2 Sol-gel Process

1. ZnO Sol-gel Preparation

Zinc acetate dihydrate ($Zn(CH_3COO)_2.2H_2O$), isopropanol (C_3H_8O), and monoethanolamine ($HO(CH_2)_2NH_2$) are used in the ZnO sol-gel preparation process as the source of zinc, solvent, and stabilizer, respectively. To obtain 55 ml of 0.3 mole/cm^3 ZnO sol-gel, 3.58 g of zinc acetate dihydrate from Avantor performance materials Inc. was dissolved in 54 ml of isopropanol with 1 ml of 99% monoethanolamine (MEA) from Alfa Aesar. The solution mixture was stirred by a magnetic stirrer for 2 hours at 70℃ to yield a clear homogenous solution. The reaction between zinc acetate dihydrate and isopropanol initially forms a complex called monoacetate ($[ZnCH_3COO]^+$) [10]. The chemical reaction can be written as follows,

$$Zn(CH_3COO)_2.2H_2O + C_3H_8O \rightarrow [ZnCH_3COO]^+ + [CH_3COO]^- + 2H^+ + 2(OH)^- + C_3H_8O \quad 4.1\text{-}1$$

Low quantity of water in the solution slows the hydrolysis process of Zn cation and disturbs the condensation. Moreover, the MEA further prevent the Zn cation condensation result in milky solution turns into clear solution after adding MEA. Also, the MEA is an amine which increases the pH value of the solution to enhance the ZnO formation. The $[CH_3COO]^-$ and H^+ reacts to form acetic acid (CH_3COOH) and the monoacetate reacts with $(OH)^-$ groups to form zinc hydroxide ($Zn(OH)_2$) at temperatures below 150℃ [10].

$$[ZnCH_3COO]^+ + H^+ + 2OH^- \rightarrow CH_3COOH + Zn(OH)_2 \quad \text{4.1-2}$$

The chemical reaction mechanism and the subproducts of the ZnO sol-gel process were determined by FTIR absorption [10], [11] and transmittance spectra analysis [12]. The clear ZnO sol-gel contains zinc hydroxide and needs to be stored below 100℃ temperatures to avoid partial ZnO formation in the solution.

2. Spin Coating Process

Spin coating is a technique which uses centrifugal force generated by the rotating substrate combined with the surface tension of the solution to deposit thin film (typically ~ 10s of nm) across the surface of the substrate. One of the advantages of the spin coating process is its capability to deposit films on substrates with a broader range of sizes from few mm samples to larger flat panel TV screens. Also, due to the instrumental simplicity, it is easy to integrate into the process. The ability to achieve uniform and consistent film with high spin speeds is another advantage. However, there are few drawbacks in the techniques also such as low throughput due to single substrate deposition compared to batch deposition and high chemical waste. There is only 10% of the chemical used in the process while the rest being flung off during the deposition. The spin coating process involves three steps mechanism as shown in figure 4.1-1.

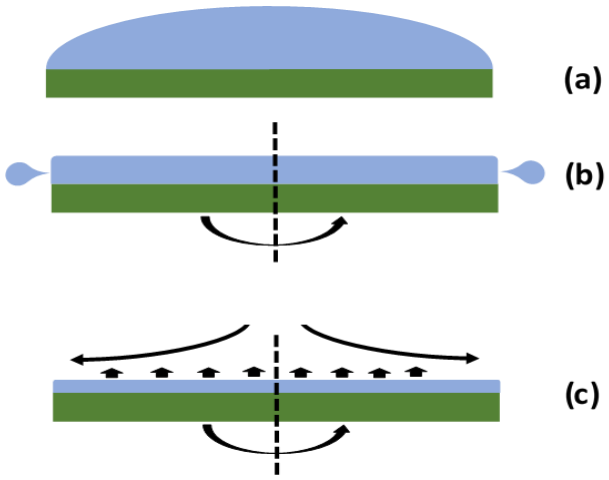

Figure 4.1-1: Schematic diagram of main steps of film deposition in spin coating; (a) sol-gel poured onto the substrate, (b) substrate spins at high speed, and excess solution fling off to sides, and (c) airflow dries the coated film by evaporating excess solvent.

The thickness of the film depends on the parameters such as speed of the spinner, the viscosity of the solution, vapor pressure, temperature and local humidity. The film thickness (t) and the spin-coated film can be obtained by [13],

$$t = k\frac{p^2}{\sqrt{\omega}} \sim \frac{v^{0.4}}{\omega^{0.2}} \qquad 4.1\text{-}3$$

where k is spinner constant, p is the percentage of solids in the solution, ω is the spin speed in rpm, and v is the viscosity of the solution. It is standard practice to determine the required conditions empirically to achieve the desired thickness for a film.

3. ZnO Thin Fim Deposition

The oxidized Si wafers with 100 nm dry oxidized SiO_2 and highly p doped (Boron) Si substrate with <100> orientation and 0.001-0.005 Ω. cm resistivity purchased from University wafers Inc. First, the Si wafer was cleaned with house nitrogen are gun to remove any dust particles

on the surface and attached to the spinning head of the spin coater. It is essential to make sure the Si wafer is well centered and leveled. The ZnO sol-gel solution pours onto an oxidized Si wafer to spin coat a thin film of ZnO. The spin speed was maintained at 3000 rpm for 30 s at room temperature under ambient. Then the coated film was calcined at 285℃ for 5 minutes on a hot plate under ambient. At 285℃ with O_2 from the air, zinc hydroxide decomposes into ZnO as following,

$$Zn(OH)_2 \rightarrow ZnO + H_2O \qquad 4.1\text{-}4$$

The thickness of the film was measured by profilometer and recorded as ~ 25 nm. The spin coating and following calcination process was repeated to obtain the desired ZnO film thickness, e.g., four times repetition to obtain 100 nm ZnO film. Finally, the film was post-annealed at 800℃ in air for 1 hour to achieve polycrystalline phase in deposited ZnO film.

4.1.3 Radio-Frequency Magnetron Sputtering

1. The principle of rf-Magnetron Sputtering

Sputtering systems use energetic ions generated in a plasma to bombard on a target which is the cathode of the setup. Then the ejected atoms from the surface of the target impinge on a substrate (sample) mounted to the anode to form a film [14]. In general, Ar^+ is widely used as the bombarding ions in the plasma. Sputtering systems can be categorized based on the source of plasma discharge; direct-current (DC) sputtering and radio-frequency (rf) sputtering. The rf-sputtering employed rf source to generate a plasma while DC sputtering used DC gaseous discharge. In rf-sputtering system, the cathode and the anode are in series with a blocking capacitor. The blocking capacitor is a part of an impedance matching network to maximize the

power transform from rf source to plasma. The rf source operates at fixed 13.56 MHz. Figure 4.1-2 shows the schematic diagram of an rf-sputtering system.

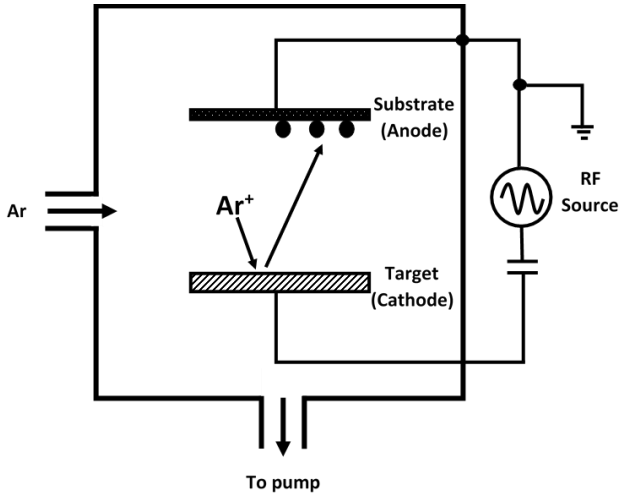

Figure 4.1-2: Schematic diagram of the rf-sputtering system.

The magnetron is a source that intensifies the plasma by using a magnetic field [15]. In the magnetron configuration, a permanent magnet is applied to create magnetic flux parallel to the surface of the target. Therefore, the plasma gets intensified due to the electron trapping took place with the magnetic field near the target surface. This phenomenon results in enhanced sputtering rate in rf-sputtering.

2. ZnO Thin Film Deposition

A 99.9% pure ZnO target from Kurt J. Lesker company was bonded to a copper back plate to enhance the conductivity between the cathode and the target. The diameter and the thickness of the target were 3" and 0.125", respectively. First, the ZnO target was attached to the cathode of the rf-sputtering system. Then the oxidized Si wafers with 100 nm dry oxidized SiO_2 and highly p doped (Boron) Si substrate with <100> orientation and 0.001-0.005 Ω. cm resistivity purchased

from University wafers Inc. loaded and attached to the anode. The parameters were fixed as shown in table 4.1-2 to deposit a thin film of ZnO.

Table 4.1-2 Parameters applied to Denton Discovery 18 rf-magnetron sputtering system

Material	ZnO
Pre-sputtering power (W)	160
Pre-sputtering time (s)	300
Sputtering power (W)	160
Sputtering time (s)	1200
Ar flow rate (sccm)	25
O_2/N_2 flow rate (sccm)	1
Deposition temperature (℃)	RT
Deposition pressure (mTorr)	5
Substrate holder rotation (%)	50

Then the films were post-annealed at 800℃ for 2 hours in air to obtain polycrystalline ZnO film. The thickness of the film was measured as 70 nm by a profilometer.

4.1.3 Cleaning

A clean substrate surface has been recognized as an essential requirement in the fabrication of semiconductor microelectronic devices. The micro-contamination causes 50% of yield loss in integrated circuit fabrication. The contaminants can be introduced to the surface during the storage and fabrication process through process chemicals, tools, and human operations. These impurities can be diffused into the material under high-temperature fabrication process leading to device

failure. Therefore, it is required to remove organic contaminants, metallic impurities, adsorbed molecules and residual species before and after low-temperature processing steps [16], [17]. The surface contaminants can be categorized into three main domains; molecular compounds, ionic materials, and atomic species [18]. Molecular compounds are most likely the organic contaminants from photoresist, solvent residues, storage containers, and metal oxides or hydroxides. Ionic materials such as sodium ions, fluorine ions, and chlorine ions are physically adsorbed to the surface during the processing. The atomic species such as gold and copper are mainly introduced by equipment.

For device fabrication, the ZnO deposited Si wafer was diced into 1×1 cm pieces. Then the individual pieces were chemically cleaned in the order of acetone and methanol in an ultrasonic bath for 5 minutes in each solvent. Finally, the samples were rinsed with deionized (DI) water to remove any remained acetone or methanol residuals. House nitrogen gas blew on the pieces to dry the samples before use for photolithography.

4.1.4 Photolithography

Photolithography is a process that uses light to transfer a pattern into the substrate. The photolithography has its limitation with the minimum feature sizes to be in few μm. Therefore, in most modern device fabrication process, electron beam lithography is employed to obtain smaller feature sizes in nm scale. In this dissertation, the sensitivity of the photolithography was sufficient with required minimum device dimensions. The patterns are initially transferred from the photomask to light-sensitive polymer called photoresist. Chemical or plasma etching is then used to transfer the pattern to the substrate. The typical photolithography process involves multiple steps

to follow to yield the device pattern on the substrate. Figure 4.1-3 illustrates the order of photolithography process.

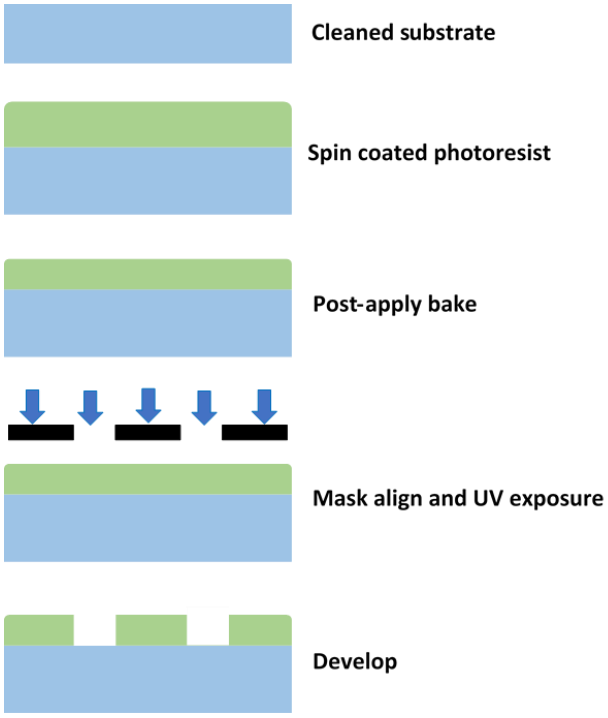

Figure 4.1-3: The order of photolithography process with positive photoresist.

Initially, a diced sample was attached to the center of a mechanical grade 3" Si wafer by acetone-soluble wax. Then the sample-wafer assembly was coated with photoresist (AZ-5414e IR) by spin coating at 4000 rpm for 30 s. Next, the sample was annealed in a process called post-apply bake. During the post-apply bake, the excess solvent in the photoresist layer will be removed. Hence, the thickness of the photoresist film reduces and also the adhesion of the photoresist to the substrate increases. The post-apply bake was carried out in an oven at 110℃ for 1 minute. The final thickness of the photoresist layer was approximately 1.4 µm. There are two types of photoresists; positive photoresist (e.g., AZ-5414e-IR) and negative photoresist (e.g., AZ-nLOF 2070). The positive photoresist becomes more soluble when it exposed to UV light, and negative photoresist gets harden with UV exposure. The selection of the type of photoresist depends on the

kind of photomask used to transfer the pattern. Figure 4.1-4 indicates the use of positive and negative photoresists.

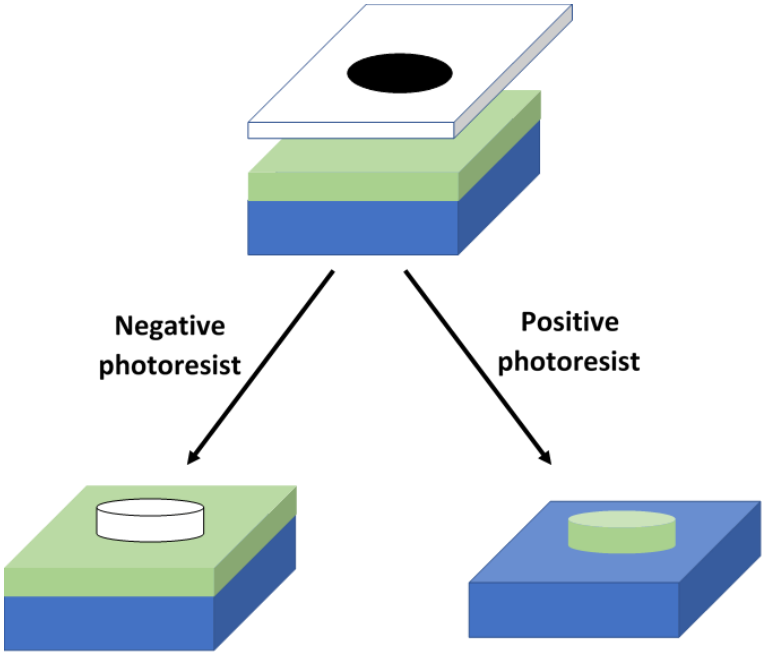

Figure 4.1-4: Illustration of pattern transfer mechanism of positive and negative photoresist.

After the post-apply bake, the sample was mounted to sample holder of the mask aligner to initiate photolithography process. A Karl Suss MJB3 UV400 mask aligner equipped with a 160W Hg lamp as the UV source was used for the photolithography. A photomask which is a quartz plate patterned with chromium was mounted above the sample. Then the sample and the pattern on the photomask were aligned by using the optical microscope attached to the mask aligner. After that, the sample was exposed to UV light for 30 s. Depending on the type of photomask and the photoresist, it is required to do post-exposure bake. Clear field photomask has an opaque pattern on a transparent background, and dark field photomask has a transparent pattern on an opaque background. AZ-5214e photoresist has a capability of image reversal (IR). A crosslinking (hardening) agent form in the photoresist when the post-exposure bake is applied at

110℃ for 1 minute. A direct Re-exposure of UV (flood exposure) to the post-exposure baked sample makes photoresist harden in areas where a higher dose of UV absorbed than the lower dose, results in the image reversal. Figure 4.1-5 illustrates the image reversal process with post-exposure bake and UV flood exposure.

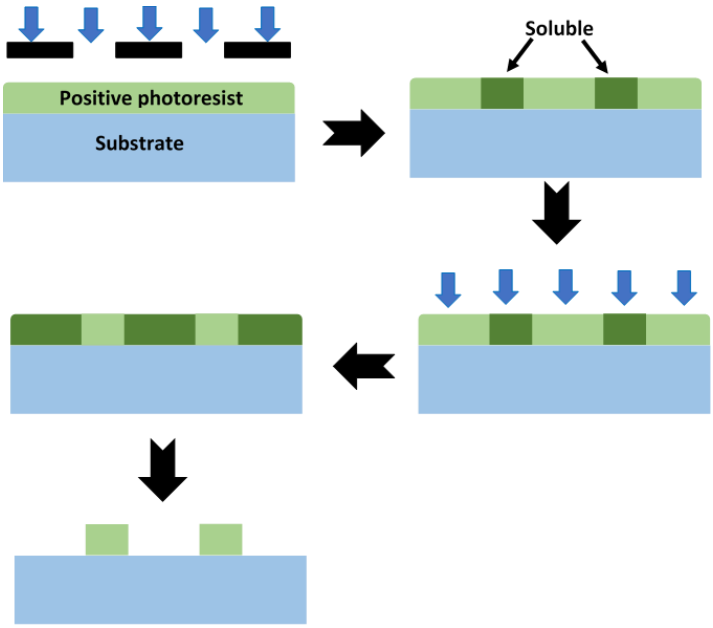

Figure 4.1-5: Illustration of image reversal process with AZ-5214e-IR (positive) photoresist.

Then the sample was developed in AZ 726 MIF developer to dissolve the soluble area of the photoresist film to develop the negative image of the pattern on the substrate. The shape of the transferred pattern and the linewidth control depend on the reaction between the developer and resist. In this work, the puddle development technique, which spins the substrate to spread developer efficiently was used develop the pattern on the photoresist. When the developing time elapsed, the additional developer was rinsed with DI water. It is essential to employ the rinsing immediately after development to avoid over developed patterns.

The spatial resolution of the photolithography process defines the minimum feature size (MFS) of the pattern. The MFS depends on the optical element and the wavelength of the light as follows [19],

$$resolution = \frac{\lambda}{NA} \quad 4.1\text{-}5$$

where λ is the wavelength of the exposure light, and *NA* is the numerical aperture.

4.1.5 Metal Deposition

1. Direct-Current (DC) Magnetron Sputtering

Sputtering is a process in which material is removed from a target at the cathode by bombarding energetic ions from the plasma and the ejected materials transport to the surface of the sample to deposit [20]. In a DC sputtering system, plasma is created with DC voltage applied between the cathode and the anode. Argon (Ar) is used as the regular feed gas to generate plasma with ions (Ar^+). The magnetron configuration enhances the intensity of the plasma by increasing energetic electron density near the target. Therefore, a DC magnetron sputtering system can yield higher sputtering rate compared to ordinary parallel electrode DC sputtering. Figure 4.1-6 is a schematic diagram of a DC magnetron sputtering system and elaborated metal deposition mechanism.

In the DC magnetron sputtering system in Leach science center of Auburn University, a high vacuum of 3×10^{-7} Torr can be achieved by a vacuum system coupled with roughing pump and turbopump. It consists of four 2" diameter magnetron sputtering guns and maximum DC power of 1000 W. The sample holder plate is located right above the sputtering target. The sample holder plate can be mechanically rotated once the vacuum chamber is closed. Therefore, it is plausible to

deposit four different metals on the same or several samples successively without venting the vacuum.

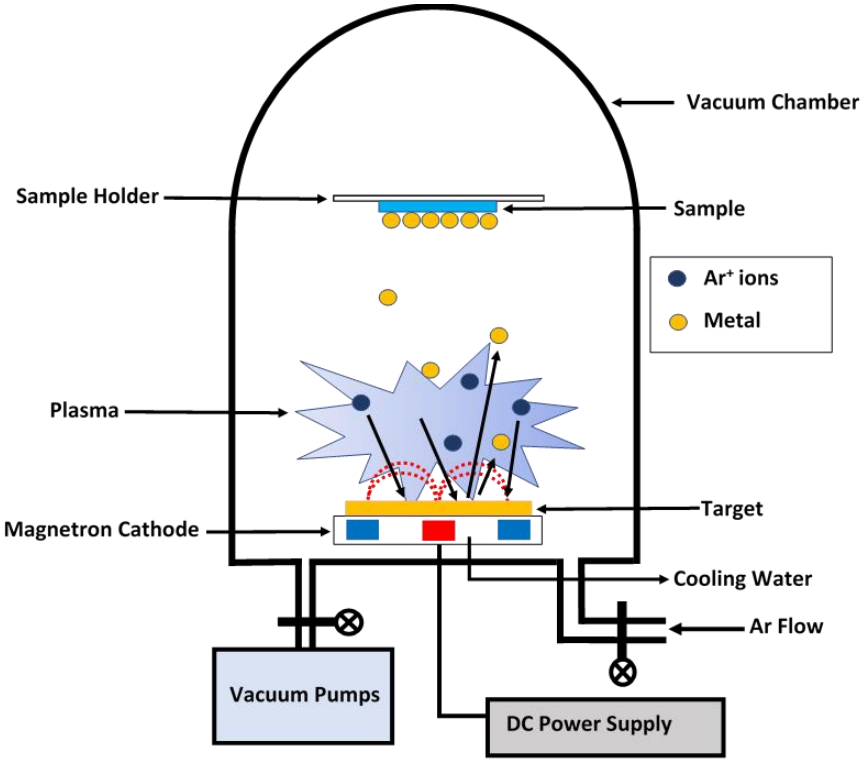

Figure 4.1-6: Schematic diagram of the DC magnetron sputtering system and the metal deposition process.

First, the 2" diameter sputtering target was attached to the sputtering gun and placed a chimney to keep the ejected material form wide spreading. Then the photolithographically patterned samples were attached to a 3" Si wafer and then mounted to the sample holder plate. The vacuum chamber was vented with the pumping assembly until it reaches to 3×10^{-7} Torr. During the sputtering, Ar was flowing into the chamber at the rate of 95 sccm (standard cubic centimeter per minute), and the pressure of the chamber was maintained at 17 mTorr. The samples were at room temperature during the deposition. A summary of parameters to be fixed for each metal deposition was given in table 4.1-3.

Table 4.1-3 Summary of sputtering parameters for different metal depositions

Metal	Voltage (V)	Current (A)	Pre-sputter time (s)	Sputter time (s)	Film thickness (nm)
Ti	290	0.25	180	360	100
Pd	380	0.25	40	120	140
Ir	490	0.25	60	20	15
$Ni_{93\%}$ $V_{7\%}$	340	0.25	120	240	40

The pre-sputter time is required to remove any impurities on the target surface before depositing the metal on samples. During the pre-sputter, the samples were kept away from the sputter target by mechanically rotating the sample holder. When the sputtering time is elapsed, the samples were taken out after venting the vacuum in the sputtering chamber.

2. Thermal Evaporation

Thermal evaporation method required to heat metal to the point of vaporization, and then the evaporated metal deposited on the surface of the sample. A higher vacuum is essential to control the composition of the deposited metal in thermal evaporation technique [21].

Figure 4.1-7 shows the schematic diagram of the thermal evaporation system in this dissertation work to deposit Aluminum (Al). The pressure of the chamber was maintained at approximately 5×10^{-6} Torr by vacuum system equipped with roughing pump and diffusion pump. The 99.999% aluminum pallets (1/8"×1/8") from Kurt J. Lesker company were used in the metal evaporation process. Metal evaporation was done by heating an alumina-coated tungsten bucket to 1500℃. The relationship between the deposited metal thickness and the applied DC bias and

evaporation time were empirically determined. Thermal evaporation at 60 W for 4 minutes after 1-minute pre-evaporation yield approximately 140 nm Al layer. Aluminum deposition by DC sputtering was time-consuming due to its low deposition rate, and it was required to pause the sputtering process frequently to avoid overheating the target. In contrast, thermal evaporation was convenient and faster than DC sputtering. However, one of the drawbacks in thermal evaporation is its lack of thickness control. It was identified that the reuse of heating bucket causes the problem of the thicker film than expected. The reason was that the pre-deposited Al on the heating bucket evaporated in addition to the added Al pallets, thereby result in thicker Al deposited on the sample. This problem can be avoided by using a new heating bucket and also with a more sophisticated solution which is assembling a mass flow detector to monitor the deposited film thickness.

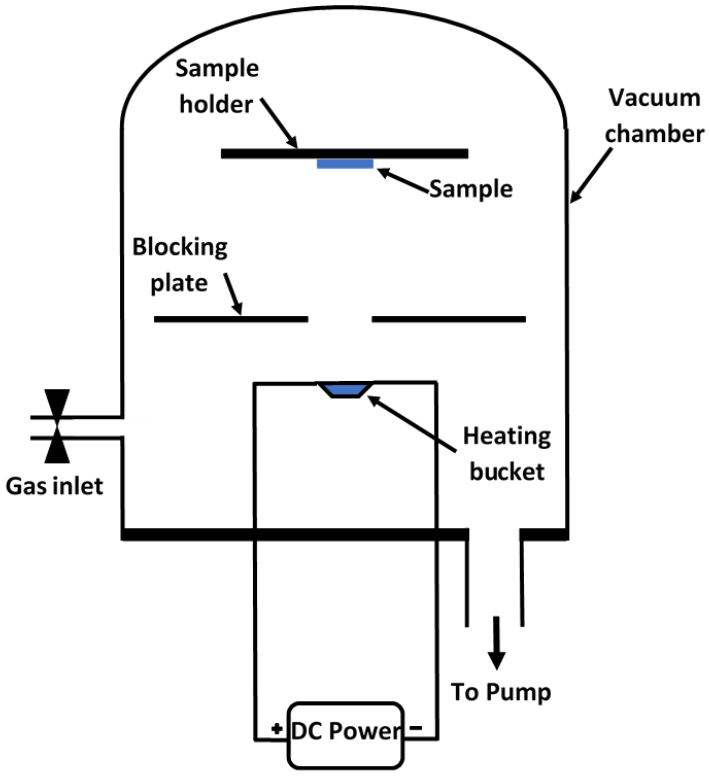

Figure 4.1-7: Schematic diagram of the thermal evaporation system.

4.1.6 Lift-off

Lift-off is a process that removes the excess metal deposited on the substrate by stripping photoresist underneath. In this dissertation work, wet chemical lift-off was performed with acetone to dissolve photoresist and lift-off the excess metal to pattern metal contacts on the substrate. The duration of the lift-off process depends on several factors such as the thickness of the metal film, type of photoresist, post-apply bake temperature, UV exposure dose, and quality of the photoresist layer.

4.1.7 Rapid Thermal Annealing (RTA)

Rapid thermal annealing (RTA) is mainly employed to activate implanted dopants and yield excellent ohmic contact by interfacial diffusion of metal and semiconductor. In this dissertation, RTA was used to obtain good ohmic behavior for deposited Ti/Pd and Ti/Ir contacts. RTA treatment at 300℃ for 1 minute under N_2 ambient could yield contact resistivity as low as $3.34\times10^{-4}\ \Omega\ cm^2$ and $1.68\times10^{-5}\ \Omega\ cm^2$ for Ti/Ir and Ti/Pd contacts on ZnO, respectively. At 300℃ oxygen from ZnO diffuse into Ti to form TiO generating oxygen vacancies (V_0) in ZnO [22]. The Gibbs free energy per mole of oxygen for TiO_2 ($\Delta G_{600\ K}$=-833.972 kJ/mole) is lower than that of ZnO ($\Delta G_{600\ K}$=-290.452 kJ/mole) [23]. Therefore, the formation of TiO is preferable at 300℃ RTA. The created V_0 at the ZnO/Ti interface act as shallow donors to enhance the conduction [24]. The RTA system consists of a vacuum chamber, an infrared optical pyrometer, and a rheostat to control the current. Figure 4.1-8 shows the schematic diagram of the RTA system.

The RTA system used in this work contains two carbon stripes separated by 2” as the heating element. First, the samples were placed in a carbon crucible and then the crucible was mounted on the carbon strip. The infrared optical pyrometer located right above the vacuum

chamber focused to the carbon stripe adjacent to the sample. Then the vacuum chamber was vented to achieve 2×10^{-7} Torr by the use of a roughing pump and then a diffusion pump. After that, the chamber was filled with high purity N_2 and brought the chamber pressure to atmospheric pressure. The carbon stripe was heated to obtain 300℃ by carefully adjusting the input power. During the 1 minute RTA under N_2 ambient, the temperature of the sample was maintained at 300℃. Right after the annealing time elapsed; the samples were cooled down to the room temperature rapidly with the aid of a mechanical fan located closer to the vacuum chamber.

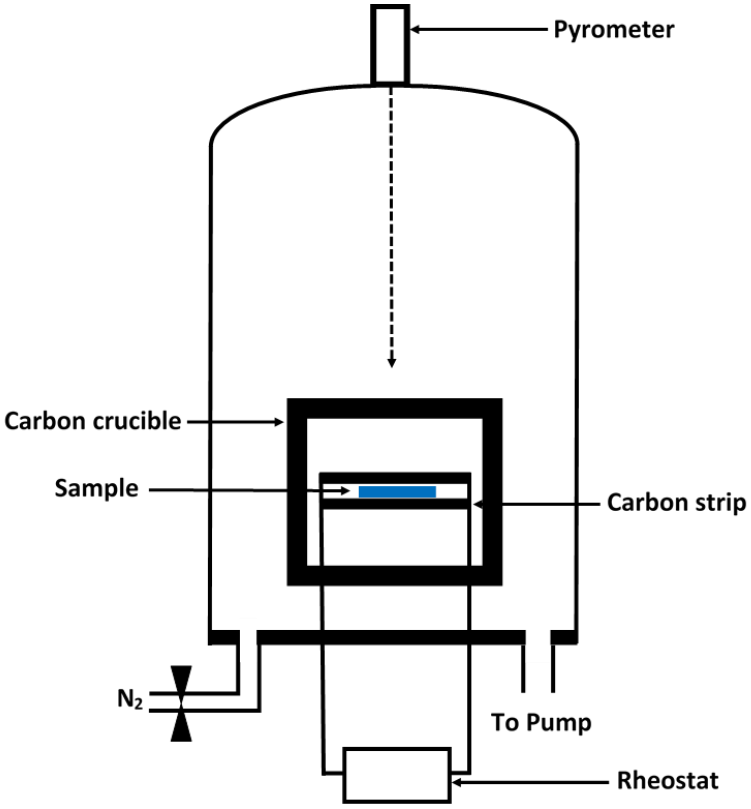

Figure 4.1-8: Schematic diagram of rapid thermal annealing (RTA) system.

The back-gated ZnO TFTs were prepared for electrical measurements by attaching a gold-plated ceramic plate to the back of the Si substrate by conducting silver paste. The back of the Si substrate was scratched out to remove natural oxide to access conducting Si substrate which

employed as the gate electrode in the ZnO TFTs. The attached gold plate was used to land probe to the gate electrode. Figure 4.1-9 shows a picture of the fabricated ZnO TFTs for this dissertation work.

4.2 Experimental Procedure

In this work, ZnO film analysis and characterizations were performed by micro-Raman spectroscopy, photoluminescence, and X-ray diffraction spectroscopy. The current-voltage (I-V) and capacitance-voltage (C-V) measurements were carried out as electrical characterizations of ZnO TFTs. The proton irradiation experiment on ZnO TFTs and ZnO films were done by the 2MV Tandem source Pelletron accelerator in Leach science center, Auburn University.

4.2.1 Micro-Raman Spectroscopy

Mainly Raman spectrometer consists of 4 components as listed as follows;

1) Excitation source
2) Sample holder and microscope
3) Wavelength selector
4) Detection and computer controlled processing system.

The laser has been used as an excitation source of modern Raman spectroscopy due to the ideal characteristics of large peak power in the order of MW, monochromatic beam with weak spurious lines, smaller beam diameter, and the availability of wide range of wavelength. The He-Cd laser provides blue (441.563 nm) and UV (325 nm) laser lines with average power 40 and 10 MW, respectively. The Rayleigh and anti-stokes can be eliminated by using edge filters. The Raman scattering is an inherently weak signal. Therefore, the laser beam needs to focus on the sample and collect the scattered beam from the sample. The laser excitation and scattered beam collection

from the sample can be done with several optical configurations such as 90° and 180° scattering geometries in the lens system. The preliminary focusing of the incident laser beam on the sample is done by an optical microscope. During the sample focusing by the optical microscope, the laser beam was blocked by a shutter system. Once the sample focus is done, the shutter was opened and the adjustable mirrors were moved to focus the laser beam on the sample. The grating monochromators are used as wavelength selectors. A selective wavelength is used in Raman spectroscopy to obtain better resolution and accordingly to the scanning range. The 2400 lines/mm grating facilitates wider scan range (200-750 nm) while 3600 lines/mm provides better resolution compared to 2400 lines/mm. The charge-coupled detector (CCD) has used as the detection device in Raman spectrometer. The CCD is a silicon-based arranged array of photosensitive elements. When a photon strikes on each pixel, it stored as a small charge. Therefore, each pixel store charges as a function of the stricken photon on individual pixel. The low readout noise in CCD is an advantage compared to other multi-channel detectors. Hence, the signal intensification for weak Raman signal is unnecessary with CCD. A wider range of wavelengths for detection can be obtain with the use of CCD as well.

Our custom-made Raman spectrometer consists of He-Cd laser from Kimmon Koha Co.Ltd., which excites 441.563 and 325 nm laser lines. The diameter of the laser beam measured as 5-10 μm after focused on the sample by the optical microscope. An edge filter used to filter out Rayleigh and anti-stock signals before entering to the Jobin Yvon spectrometer. The CCD with 2048×512 pixel array used to detect the Raman signal with higher precision. The scan with 2400 lines/mm grating provided 1 cm^{-1} resolution. The schematics diagram of Raman spectroscopic system is presented in figure 3.1-3.

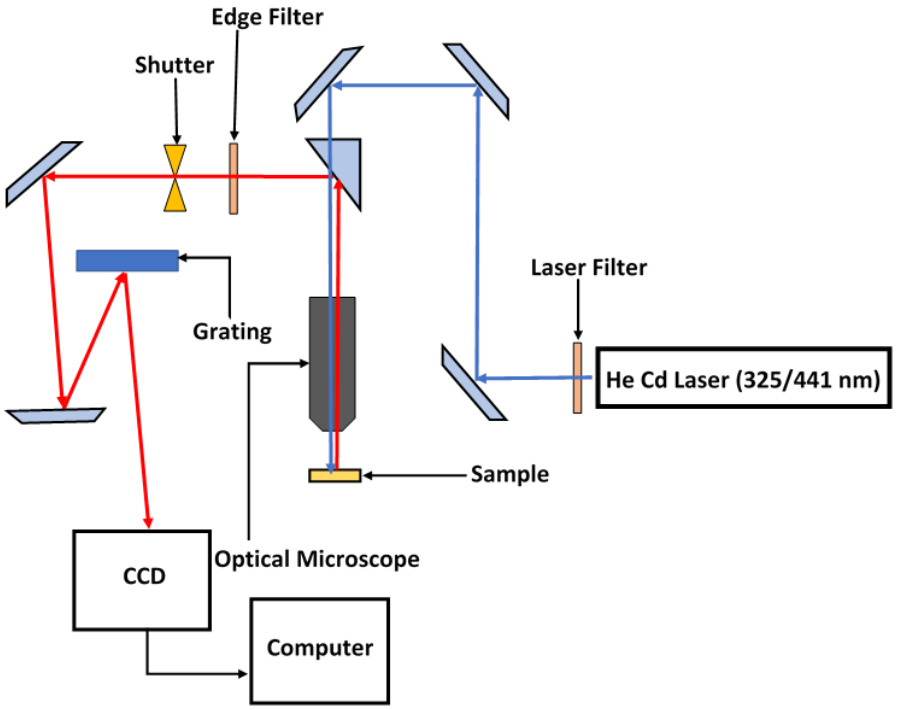

Figure 4.2-1: Schematic diagram of micro-Raman spectrometer.

4.2.2 Photoluminescence (PL)

In photoluminescence, ZnO films were exposed to 325 nm laser line generated by He-Cd laser from Kimmon Koha Co.Ltd. The PL spectra were dispersed with 2400 lines/mm grating. The PL measurements were performed at room temperature. The penetration depth of 325 nm laser into ZnO layer is determined as around 60 nm. Therefore, PL spectra represent the characteristics of bulk ZnO. The variation in the intensity of the UV peak and the broad visible luminescence peak would provide the insight into the crystal quality and the defect concentration in the sub-bandgap region of ZnO. The blue, green and yellow luminescence observed in PL spectra are produced by the electron transitions from neutral oxygen vacancy to valence band (~2.8 eV), singly ionized oxygen vacancy to valance band (~2.5 eV), and delocalized electron near conduction band

recombination with doubly ionized oxygen vacancy (~2.2 eV), respectively [25]–[27]. The UV peak observed in PL spectrum is caused by the band to band radiative recombination in ZnO. Figure 4.2-2 shows the comparison of PL spectra of ZnO films deposited by the sol-gel method and the rf-magnetron sputtering.

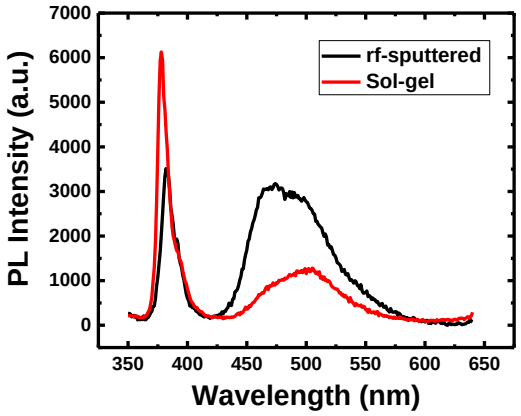

Figure 4.2-2: The PL spectra of ZnO films deposited by sol-gel spin coating and rf-magnetron sputtering.

As can be seen in figure 4.2-2, the near band edge UV emission is dominated over deep level emission in sub-bandgap region for ZnO. Sol-gel derived ZnO films show high intensity in UV peak compared to visible luminescence. Visible luminescence in PL spectra can be attributed to native defects such as oxygen vacancies and other impurities introduced during the film deposition. Therefore, the high intensity in visible luminescence in rf-sputtered ZnO indicates high level of native defects and impurities in film. Since sol-gel ZnO shows higher I_{UV}/I_{Vis} compared to rf-sputtered films, sol-gel derived ZnO films are much favorable for optoelectronic applications.

4.2.3 X-Ray Diffraction Spectroscopy (XRD)

The XRD analysis of ZnO films was employed to determine the crystal quality of the ZnO. The Bruker D2 Phaser XRD system used in this dissertation work is shown in figure 4.2-3.

Figure 4.2-3: Picture of Bruker D2 Phaser XRD system in the department of Geosciences, Auburn University.

The XRD analyzer consists of a Lynxeye detector and a Cu shutter tube. The X-ray was generated with 300 W power, and the wavelength was 1.54184 $\dot{A}$. Sample was rotated at a speed of 20 rpm during the data collection to obtain a spectrum for the sample. The sample scan was performed in continuous PSD mode with 0.5 s scan time and 0.02^0 2θ increment for the scan range. It is important to use the same procedure to load the sample to the XRD chamber to avoid the spurious parallel shift in XRD spectra. For example, if the upper surface of the sample is elevated compared to the surface of the sample holder, the XRD peaks tend to shift in higher 2θ direction. When the upper surface of the sample is located below the surface of the sample holder, the XRD peaks shift in lower 2θ direction. Therefore, the shift in XRD peaks due to stress and strain in ZnO crystal structure can be shadowed by the spurious shift in XRD spectra.

The grain size of polycrystalline ZnO can be extracted from XRD data by using Debye-Scherrer relationship [28].

$$D = \frac{k\lambda}{B\cos\theta} \quad \text{4.2-1}$$

where, D is the grain size, k is 0.94, λ is the wavelength of x-ray, B is the full width at half-maximum (FWHM) of (0002) peak in radians, and θ is the Bragg angle for the (0002) peak. For hexagonal structures, the biaxial stress of the film along c-axis can be obtained by [29],

$$\sigma_{film} = \frac{2C_{13}^2 - C_{33}(C_{11}+C_{12})}{C_{13}} . \varepsilon_z \quad \text{4.2-2}$$

where, C_{11}= 209.7 GPa, C_{12}= 121.1 GPa, C_{13}= 105.1 GPa, and C_{33}= 210.9 GPa are the elastic stiffness constants for ZnO [30]. The ε_z is strain in the lattice along c-axis, which can be deduced by [29],

$$\varepsilon_z = \frac{(C - C_0)}{C_0} \quad \text{4.2-3}$$

where C and C_0 are the strained and strain-free lattice parameters of ZnO, respectively. The strain-free lattice parameter (C_0) was obtained from a joint committee of powder diffraction standards (JCPD) card 75-0576 card. The lattice parameter for (002) peak of ZnO film was calculated by the following equation [31];

$$\frac{1}{d_{(hkl)}^2} = \frac{4}{3}\left[\frac{h^2+hk+k^2}{a^2}\right] + \frac{l^2}{c^2} \quad \text{4.2-4}$$

where a and c are lattice parameters of ZnO. The $d_{(002)}$ can be obtained by Bragg's equation;

$$d_{(002)} = \frac{\lambda}{2\sin\theta_{(002)}} \quad \text{4.2-5}$$

where, λ is the wavelength of x-ray and $\theta_{(002)}$ is the Bragg angle for (002) peak. Figure 4.2-4 shows the XRD spectra for ZnO films deposited by sol-gel spin coating and rf-mangetron sputtering.

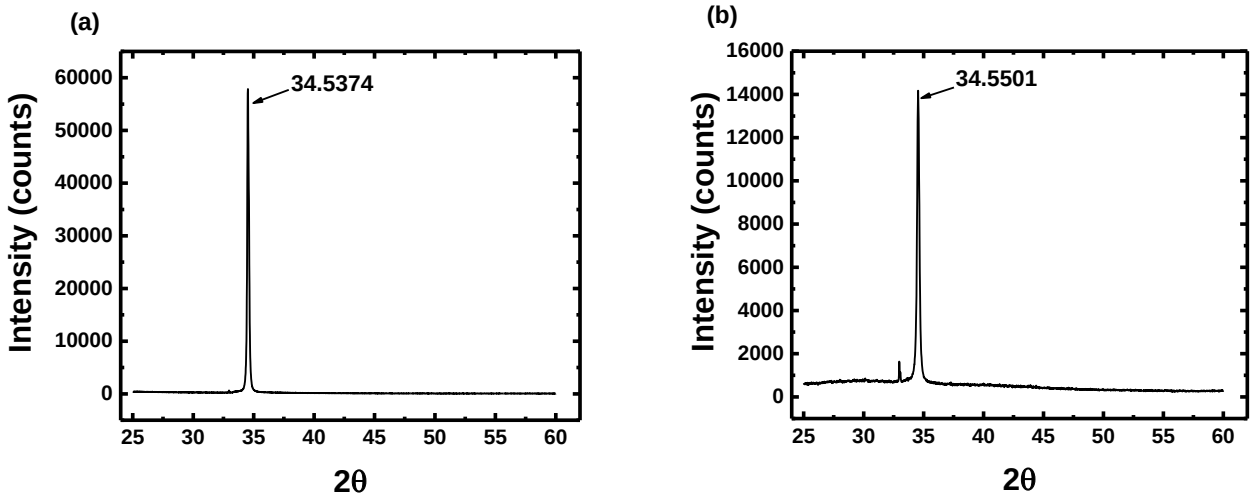

Figure 4.2-4: XRD spectra of ZnO film deposited by (a) sol-gel spin coating, and (b) rf-magnetron sputtering.

The calculalated biaxial stress of the ZnO film along c-axis is summarized in table 4.2-1.

Table 4.2-1 Calculated biaxial stress of the ZnO film along the c-axis.

Deposition technique	σ_{film} (GPa)
Sol-gel	1.469
rf-magnetron sputtering	1.630

4.2.4 Current-Voltage (I-V) and Capacitance-Voltage (C-V) Measurements

I-V measurements for output characterizations and transfer characterizations were done using an H-100 Signatone probe station equipped with Keithley 6517 voltage source. Typically all the electrical measurements were performed at room temperature and in dark environment.

However, in specially designed experiments which required a controlled environment, a cryogenic manipulated probe station from Advanced Research Systems equipped with Keithley 4200-SCS parameter analyzer was used. Low-frequency C-V measurements for the capacitance of vertical $ZnO/SiO_2/Si$ MOS structure were done using an H-100 Signatone probe station equipped with Keithley 590CV analyzer. The C-V analyses were also performed at room temperature and in dark environment. Calibrated cables with Signatone S-725 micropositioners were used in electrical measurements to increase the signal to noise ratio. The electrical measurement data were extracted from a Labview programme written to collect output, transfer characteristics, and capacitance.

4.2.5 Proton Irradiation

The proton irradiation process for data reported in chapter 6 and appendix II performed by a 2 MV Tandem source Pelletron accelerator in Leach science center, Auburn University. Figure 4.2-5 shows the schematic diagram of the Pelletron accelerator.

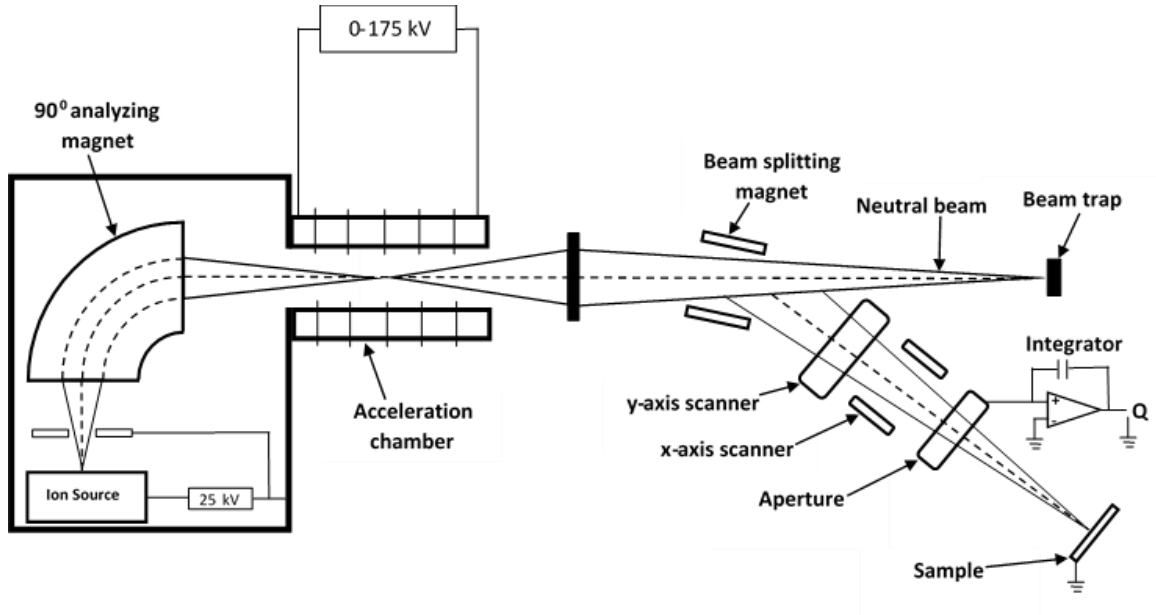

Figure 4.2-5: Schematic diagram of the particle accelerator.

Protons were generated by stripping an electron from hydrogen with nitrogen. Then the protons were accelerated to gain 200 keV energy. The energetic proton beam was guided towards the sample mounted at the end of the beam line with a beam splitting magnet. The sample was under the vacuum with a pressure of 5×10^{-6} Torr, and cooling water was flowing through the sample holder to keep the sample at room temperature during the irradiation. The fluence of the proton radiation was carefully maintained at 1.0×10^{14} protons/cm^2 by monitoring the beam current throughout the irradiation process. The proton beam was scanned over a 6.3 cm diameter circular aperture area with a scan rate of 64 Hz in the y-axis and 517 Hz in the x-axis. Four isolated Faraday cups located on the aperture, 4" apart from each other were monitored the proton beam current. Equal current readout in all four Faraday cups indicates a uniform distribution of proton across the sample. The Fluence of the proton beam was fixed with beam current and the exposure time as follows,

$$Time = \frac{q\times fluence\times A}{I} \qquad 4.2\text{-}6$$

where q is the charge of a proton, A is the area of the aperture, and I is the beam current. The fluence of 1.0×10^{14} proton/cm^2 was obtained with 781 s irradiation time and 700 nA current. Moreover, a larger movable Faraday cup located 8" upstream of the sample was used to monitor beam current intermittently to confirm uniform proton irradiation over the sample. The ZnO samples were mounted to the sample holder with conducting carbon tape. Therefore, the gate electrodes of ZnO TFTs were grounded during the proton irradiation.

References

[1] S. J. Chen *et al.*, “High-quality ZnO thin films prepared by two-step thermal oxidation of the metallic Zn,” *J. Cryst. Growth*, vol. 240, no. 3, pp. 467–472, 2002.

[2] R. Ayouchi, F. Martin, D. Leinen, and J. R. Ramos-Barrado, “Growth of pure ZnO thin films prepared by chemical spray pyrolysis on silicon,” *J. Cryst. Growth*, vol. 247, no. 3, pp. 497–504, 2003.

[3] W. Tang and D. C. Cameron, “Aluminum-doped zinc oxide transparent conductors deposited by the sol-gel process,” *Thin Solid Films*, vol. 238, no. 1, pp. 83–87, 1994.

[4] Y. Takahashi, M. Kanamori, A. Kondoh, H. Minoura, and Y. Ohya, “Photoconductivity of Ultrathin Zinc Oxide Films,” *Jpn. J. Appl. Phys.*, vol. 33, no. 12R, p. 6611, Dec. 1994.

[5] V. Gupta and A. Mansingh, “Influence of postdeposition annealing on the structural and optical properties of sputtered zinc oxide film,” *J. Appl. Phys.*, vol. 80, no. 2, pp. 1063–1073, 1996.

[6] M. Aoki, K. Tada, T. Murai, and T. Inoue, “A new technique for the vapour phase epitaxial growth of ZnO as a guided-wave optical material,” *Thin Solid Films*, vol. 83, no. 2, pp. 283–288, 1981.

[7] X. W. Sun and H. S. Kwok, “Pulsed laser deposition of silicate phosphor thin films,” *Appl. Phys. Mater. Sci. Process.*, vol. 69, no. 7, pp. S39–S43, 1999.

[8] H.-B. Kang, K. Nakamura, S.-H. Lim, and D. Shindo, “Epitaxial growth of ZnO films on (0001) sapphire at low temperatures by electron cyclotron resonance-assisted molecular beam epitaxy and their microstructural characterizations,” *Jpn. J. Appl. Phys.*, vol. 37, no. 3R, p. 781, 1998.

[9] E. Fortunato *et al.*, “Recent advances in ZnO transparent thin film transistors,” *Thin Solid Films*, vol. 487, no. 1–2, pp. 205–211, 2005.

[10] A. E. Jimenez-Gonzalez, J. A. S. Urueta, and R. Suarez-Parra, “Optical and electrical characteristics of aluminum-doped ZnO thin films prepared by solgel technique,” *J. Cryst. Growth*, vol. 192, no. 3, pp. 430–438, 1998.

[11] S. Bandyopadhyay, G. K. Paul, R. Roy, S. K. Sen, and S. Sen, “Study of structural and electrical properties of grain-boundary modified ZnO films prepared by sol–gel technique,” *Mater. Chem. Phys.*, vol. 74, no. 1, pp. 83–91, 2002.

[12] H. Li *et al.*, “Sol–gel preparation of transparent zinc oxide films with highly preferential crystal orientation,” *Vacuum*, vol. 77, no. 1, pp. 57–62, 2004.

[13] S. A. Campbell, *The science and engineering of microelectronic fabrication*. Oxford University Press, USA, 1996.

[14] J. E. Mahan, “Physical vapor deposition of thin films,” *Phys. Vap. Depos. Thin Films John E Mahan Pp 336 ISBN 0-471-33001-9 Wiley-VCH January 2000*, p. 336, 2000.

[15] D. L. Smith, “Thin-film deposition: principles and practice. 1995,” *N. Y. Tc McGraw-Hill*.

[16] M. K. Sanganeria *et al.*, “Ultrahigh Vacuum Rapid Thermal Chemical Vapor Deposition of Epitaxial Silicon onto (100) Silicon I. The Influence of Prebake on (Epitaxy/Substrate) Interfacial Oxygen and Carbon Levels,” *J. Electrochem. Soc.*, vol. 142, no. 11, pp. 3961–3969, 1995.

[17] G. R. Srinivasan, “Recent advances in silicon epitaxy and its application to high performance integrated circuits,” *J. Cryst. Growth*, vol. 70, no. 1–2, pp. 201–217, 1984.

[18] W. Kern, “The evolution of silicon wafer cleaning technology,” *J. Electrochem. Soc.*, vol. 137, no. 6, pp. 1887–1892, 1990.

[19] M. Rothschild *et al.*, “Recent trends in optical lithography,” *Linc. Lab. J.*, vol. 14, no. 2, pp. 221–236, 2003.

[20] A. Elshabini, A. A. Elshabini-Riad, and F. D. Barlow, *Thin film technology handbook*. McGraw-Hill Professional, 1998.

[21] R. C. Jaeger, G. W. Neudeck, and R. F. Pierret, *Introduction to Microelectronic Fabrication, 2002*. Prentice Hall.

[22] S. Y. Kim *et al.*, “Low-resistance Ti/Al ohmic contact on undoped ZnO,” *J. Electron. Mater.*, vol. 31, no. 8, pp. 868–871, 2002.

[23] I. Barin and G. Platzki, *Thermochemical data of pure substances*, vol. 304. Wiley Online Library, 1989.

[24] A. Pöppl and G. Völkel, "ESR and Photo-ESR Investigations of Zinc Vacancies and Interstitial Oxygen Ions in Undoped ZnO Ceramics," *Phys. Status Solidi A*, vol. 125, no. 2, pp. 571–581, 1991.

[25] K. Vanheusden, W. L. Warren, C. H. Seager, D. R. Tallant, J. A. Voigt, and B. E. Gnade, "Mechanisms behind green photoluminescence in ZnO phosphor powders," *J. Appl. Phys.*, vol. 79, no. 10, pp. 7983–7990, 1996.

[26] H. S. Kang, J. S. Kang, J. W. Kim, and S. Y. Lee, "Annealing effect on the property of ultraviolet and green emissions of ZnO thin films," *J. Appl. Phys.*, vol. 95, no. 3, pp. 1246–1250, 2004.

[27] Y.-J. Lin, C.-L. Tsai, Y.-M. Lu, and C.-J. Liu, "Optical and electrical properties of undoped ZnO films," *J. Appl. Phys.*, vol. 99, no. 9, p. 093501, 2006.

[28] L. V. Azároff and R. J. Donahue, *Laboratory experiments in x-ray crystallography*. McGraw-Hill, 1969.

[29] M. K. Puchert, P. Y. Timbrell, and R. N. Lamb, "Postdeposition annealing of radio frequency magnetron sputtered ZnO films," *J. Vac. Sci. Technol. Vac. Surf. Films*, vol. 14, no. 4, pp. 2220–2230, 1996.

[30] A. M. Hellwege and K. H. Hellwege, *Numerical Data and Functional Relationships in Science and Technology: Nuclear Physics and Technology. New Series, Group I.* Springer-Verlag, 1961.

[31] S. R. Stock and B. D. Cullity, "Elements of X-ray Diffraction," *Up. Saddle River NJ*, 2001.

Chapter 6

Proton-Induced Displacement Damage in ZnO Thin Film Transistors: Impact of Damage Location

6.1 Introduction

Radiation hard electronics has been a hot topic in scientific research community due to the advancement of space exploration. The Van Allen radiation belts located near the Earth's orbit contains high energy protons and electrons. The inner belt located in the lower Earth's orbit contains protons with energy ranging between 0.1 and 400 MeV although the flux density is not well established due to the unpredictability of solar activities and limited real-time data [1]. Therefore, it is necessary to study the effect of proton irradiation on the semiconductor materials and devices for space applications.

Zinc Oxide (ZnO) has been considered as one of the candidates for radiation-hard TFT fabrication due to its higher radiation tolerance than other semiconductors such as GaN, Si, CdS, and GaAs [2]. The atomic displacement energy threshold (E_d) is one of the measures of radiation hardness of the material. A material with higher E_d is likely to have less permanent displacement damage (DD) upon irradiation. Therefore, a higher atomic displacement energy threshold of ZnO [57 eV, 18.5 eV (Zn), and 41.4 eV (O)] [3],[4] compared to GaN (19.5 eV), Si (12.9 eV), and GaAs (9.5 eV) might be the reason for higher radiation tolerance of ZnO than other materials [1]. Extensive studies of the high-energy electron [2], [5], [6] and gamma-ray [7], [8] irradiation on ZnO have been reported. However, only limited work has been reported on the effect of proton

irradiation of ZnO materials and devices [9], [10]. Auret *et al.* [9] have characterized single crystal ZnO exposed to 1.8 MeV protons with fluence up to 7×10^{14} protons/cm^2. The C-V measurements have provided evidence that ZnO shows higher resistance to proton irradiation with less than two orders of magnitude carrier removal compared to GaN. Meanwhile, Jo *et al.*, [11] Hong *et al.*, [12] and Choe *et al.* [13] have studied the proton-induced effects on ZnO nanowire-based field effect transistors (FETs). Jo *et al.* [11] have applied a bilayer polyimide (PI) with a SiO_2 dielectric to modulate the FET electrical characteristics by separating the radiation-induced charges from ZnO/SiO_2 interface. The observed threshold voltage (V_{TH}) shift in negative gate bias direction was attributed to the radiation-induced oxide-trapped charges in the SiO_2 gate dielectric. Moreover, Hong *et al.* [12] have shown a novel approach of suspending-type channel FETs to mitigate the channel/dielectric interface effect on device characteristics. As reported by the authors, the FETs with suspended the ZnO nanowire have shown a significant improvement over regular dielectric channel FETs upon proton irradiation. Choe *et al*. [13] investigated the ultraviolet (UV) photoconductivity characteristics of ZnO nanowire FETs treated with the proton beam. The larger depletion layer width and higher barrier potential might have delayed the photogenerated electron-hole pair recombination, resulting in a longer relaxation time than the unirradiated samples. Therefore, the authors claimed that the photocurrent persists longer in ZnO nanowire devices than other materials which are exposed to proton beam. Moon *et al*. [10] reported the analysis and comparison of ZnO TFT performances under rapid thermal annealing (RTA) process and post proton bombardment with 6.1 MeV energy at 6.7×10^{12} cm^{-2} to 6.5×10^{14} cm^{-2} fluences. The combined treatment of RTA and post proton irradiation showed the V_{TH} shift in positive gate bias direction in ZnO TFTs. However, previous studies have not reported extended details on the DD

effect on the device characteristics. The DD effect is much permanent in device structures than TID effect and could cause complete device failer when occurred.

In order to elucidate the displacement damage occurring in which region is much sensitive to altering the device characteristics, we have deliberately located the proton dose distribution maxima on two different regions (ZnO film and ZnO/SiO_2 interface) along the depth of the device by using the passivation layers with two different thicknesses. Since the displacement damage is less favorable to occur for thin active layers in TFTs if the energy of the proton is sufficiently high, a thick passivation layer needs to be employed to slow down the protons in order to promote the nuclear collision with atoms in the lattice [14]. Therefore, we have designed the passivation layers in such a way to locate the maximum proton dose in the ZnO film and ZnO/SiO_2 interface, thereby obtained maximum DD effect in corresponding regions. The energy of the proton irradiation (200 keV) was chosen based on two reasons. First, the principle of selectivity to use minimum passivation thickness for samples and still be comparable with radiation limit in the Van Allen radiation belt [1]. Second, the shell of the spacecraft is shielded with heavy materials such as Tungsten (W) and Aluminum (Al). High energy protons slow down significantly while they penetrate through heavy metal shield [15]. Therefore, protons lose a significant amount of its energy when they completely penetrated through the outer shield. Hence, protons with energy in MeVs tend to be in keVs when they interfere with electronics on board the spacecraft. A higher fluence (1×10^{14} proton/cm^2) was applied to simulate long-term radiation effect in ZnO TFTs in the real outer space environment. In the Van Allen belts, the protons with energy higher than 100 keV have 1×10^{7} protons/cm^2/s flux [16]. The 10^{14} protons/cm^2 fluence equals to the amount of proton radiation imposed on electronics through 10 years in Van Allen belts. A high fluence would generate a larger DD effect compared to lower fluences [14]. Since the motive of this work is to

study the DD effect based on the impact location, it is essential to apply a proton dosage that would generate sufficient amount of displacement damage to be detected.

6.2 Experiment

1. Device Fabrication

The bottom gate ZnO TFTs were fabricated on thermally oxidized highly p doped (Boron) Si wafers (purchased from University Wafer) with <100> orientation and 0.001-0.005 Ω.cm resistivity. The wafer has a SiO_2 dielectric layer formed by dry oxidation, and the thickness of the SiO_2 layer is about 100 nm. The ZnO channel layer was deposited on the SiO_2 layer by Radio-Frequency (RF) magnetron sputtering. The sputtering power, Ar flow rate, O_2 flow rate and the deposition pressure were maintained as 160 W, 25 sccm, 1 sccm, and 5 mTorr, respectively.

The device structures were photolithographically defined. Titanium (Ti) and iridium (Ir) bimetallic stack were deposited as source and drain ohmic contacts *via* direct-current (DC) sputtering, followed by lift-off process. The width (W) and the length (L) of the channel were 975 µm and 101 µm, respectively, providing 9.6 width-to-length ratio (W/L). The unintentionally grown oxide on the back side of the Si substrate was removed and conducting silver paste was applied to the backside of the Si wafer to attach the sample to a gold plated ceramic pad, forming gate electrodes for electrical measurements.The gold plated ceramic pad was removed before the proton radiation exposure.

2. Proton Irradiation

The Monte Carlo code TRIM (Transport of Ions in Matter) was used to simulate the proton dose distribution in the passivation layer (Pd/photoresist) and ZnO/SiO_2/Si stack [15]. The photoresist was used in between the Pd and ZnO layer since it is easy to remove and it would prevent the Pd diffusion into ZnO. Two different thicknesses of the passivation layer were used to

locate the maximum of proton dose absorption in two different locations; one in ZnO and the other at ZnO/SiO_2 interface (hereafter to be referred as Type Z and Type I, respectively). The AZ 5214-e photoresist from AZ electronic materials were deposited by spin coating, followed by the DC sputter deposition of the Pd layer. The thickness of the photoresist layer was 2.15 µm for both samples, and thicknesses of Pd layers were 140 nm and 106 nm for type Z and I devices, respectively. Both types of devices were irradiated at room temperature with 200 keV proton beam of 1×10^{14} protons/cm^2 fluence generated by 2 MV Tandem source Pelletron accelerator.

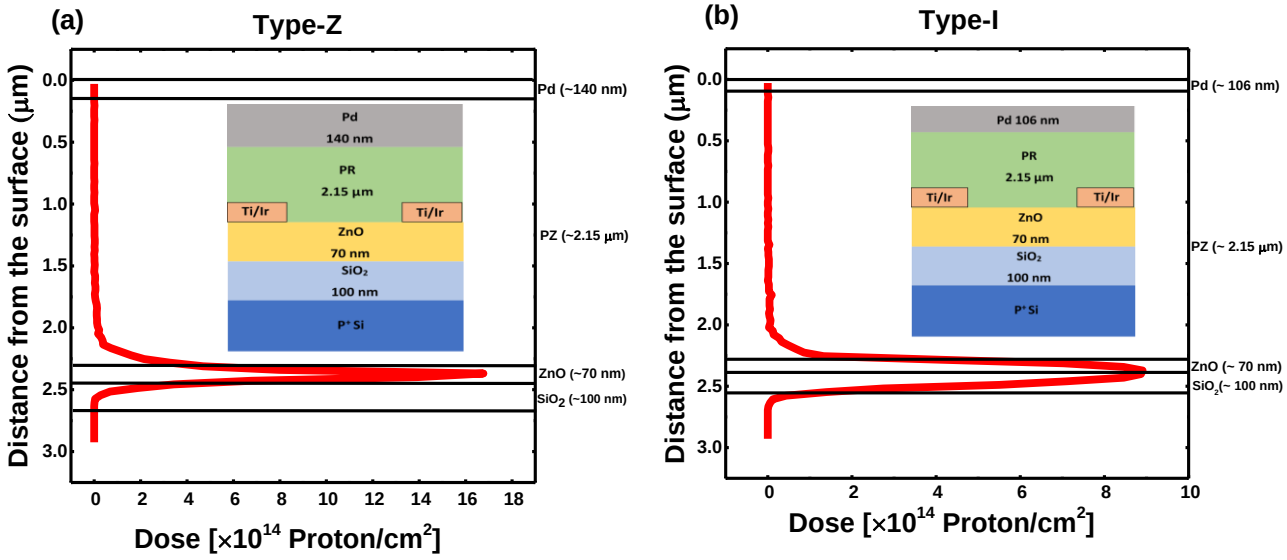

Figure 6.2-1: Proton dose-depth profile along the device structure for (a) type-Z, and (b) type-I devices. The inset shows the schematic cross-section of the device structures (not in scale)

The ZnO structural analysis before and after the irradiation for both type-Z and I devices were done by room temperature micro-Raman spectroscopy. The samples were illuminated with a 441.53 nm laser line generated by He-Cd laser from Kimmon Koha Co.Ltd. The Raman spectrum was obtained after feeding Raman signals to CCD through Jobin Yvon spectrometer consisted of 2400 lines/mm grating. The electrical characteristics of type-Z and I devices were measured before

and after irradiation. The gate electrode of the devices was grounded during the irradiation process. The transistor output characteristics and transfer characteristics were studied using an H-100 Signatone probe station equipped with Keithley 6517 voltage source. All the electrical measurements of the devices and Raman spectroscopic analysis were performed at room temperature and in a dark environment.

6.3 Results & Discussion

The samples with dimension 1 cm× 1 cm were mounted on a grounded sample holder for proton irradiation. The irradiation was done in a vacuum at an of pressure 5×10^{-6} Torr. and the sample temperature was maintained at room temperature with cooling water flowing through the sample holder during the irradiation. Hence, the annealing effect of the radiation-induced defects can be neglected in this work. The proton beam was scanned over a 6.3 cm diameter circular aperture area with scan rate 517 Hz in the x-direction, and 64 Hz in the y-direction. Four isolated and biased Faraday cups located about the aperture plate continuously monitor the current. Equal current observed in all four Faraday cups indicated the uniform exposure of the sample to the proton beam. Moreover, the current was periodically measured using Faraday cup located approximately 8 inches upstream of the sample to confirm the uniformity of the fluence during the total exposure time. A constant beam current was maintained at 700 nA for 781 s exposure time to obtain 1×10^{14} proton/cm^2 fluence.

Figure 6.2-1 shows the TRIM simulated proton dose profile for type-Z and I devices. The TRIM simulation shows that proton dose is peaking at ZnO layer and ZnO/SiO_2 interface for type-Z and type-I devices, respectively. Figure 6.3-1 shows the corresponding nonionizing energy loss (NIEL) *vs.* penetration depth along the ZnO film for type-Z and I.

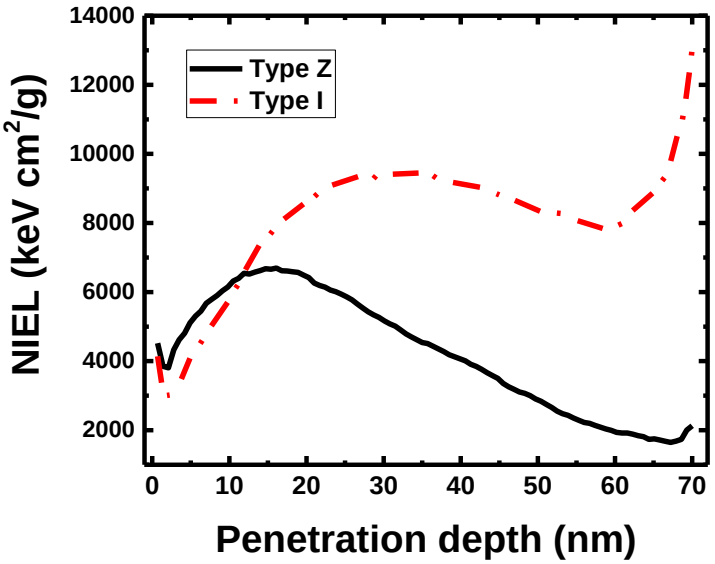

Figure 6.3-1: Nonionizing energy loss (NIEL) variation in the ZnO channel from the ZnO surface to ZnO/SiO_2 interface for type-Z and I devices irradiated with 200 keV protons.

As shown in figure 6.3-1, the maximum NIEL for type-Z locates closer to the surface of the ZnO film. The type-I shows a relatively broad distribution of NIEL with the maximum NIEL closer to the ZnO/SiO_2 interface. Note that the NIEL in ZnO layer for the type-I is higher than the maximum value of type-Z. The NIEL data can quantify the displacement damage energy distribution ($E_{d\ (damage)}$) across the material upon ion irradiation. The product of NIEL and proton fluence provides the displacement damage related deposited energy per unit mass of the material [14], [19]. The NIEL with respect to the penetration depth in ZnO film was extracted from the calculations with TRIM vacancy production rate data as described by Messenger *et al*. [20] (see Appendix I). The atomic displacement threshold energy of 18.5 eV (Zn) and 41.4 eV (O) were used in the calculation since those values showed the best agreement theoretically and experimentally [5], [4]. The contact resistance for Ti/Ir contact was measured before and after the

proton irradiation by LTLM measurements. The calculated contact resistance (ρ_C) values are summarized in table 6.2-1.

Table 6.2-1 Contact resistance of Ti/Ir before and after 200 keV, 1×10^{14} protons/cm^2 irradiation.

	ρ_C (Ω cm^2)
Before irradiation	0.032 ± 0.011
After irradiation	0.026 ± 0.005

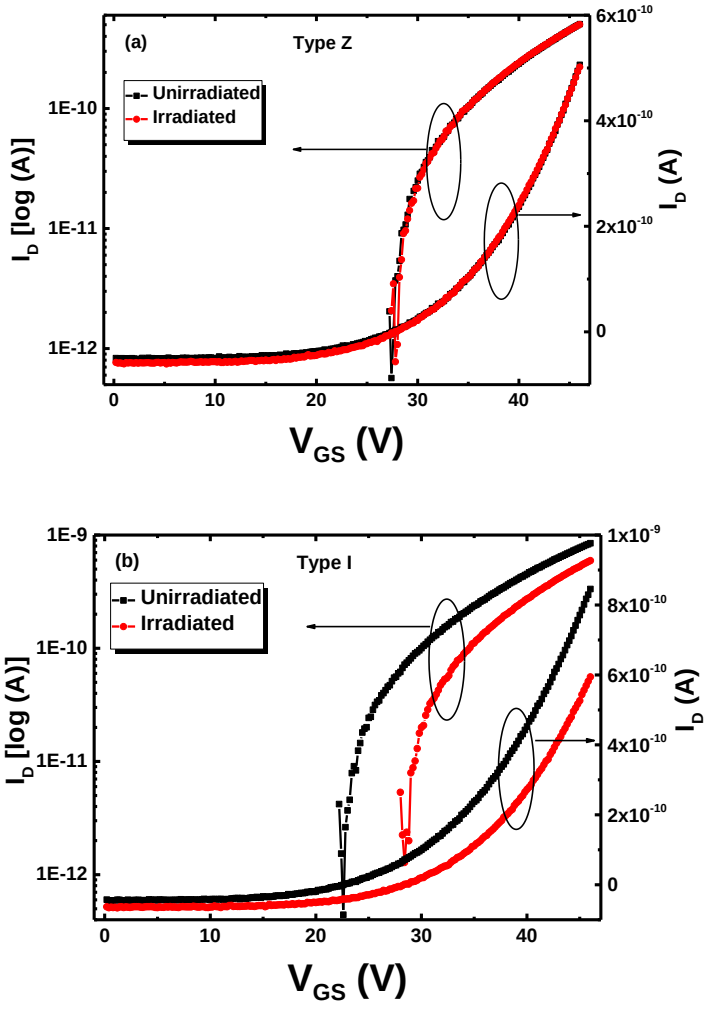

Figure 6.3-2: Transfer characteristics of ZnO TFTs collected at V_{DS}=0.1V before and after 200 keV proton irradiation for (a) type-Z and (b) type-I devices.

Figure 6.3-2 shows the transfer characteristics (collected at V_{DS}=0.1V) for the type-Z and I devices before and after the irradiation. Data collected from 10 devices from each type for electrical characterizations. As observed in figure 6.3-2 (b), the V_{TH} has shifted to the positive gate bias direction after the proton bombardment in the type-I. In contrast, the V_{TH} shift after the irradiation is negligible in type-Z as shown in figure 6.3-2 (a). The V_{TH} is determined by linear extrapolation of the following equation.

$$I_D = \mu C_i \left(\frac{W}{L}\right)(V_{GS} - V_{TH})V_{DS} \qquad 6.3\text{-}1$$

where μ is the mobility, C_i is the capacitance of the dielectric layer (SiO_2). The C_i was calculated by $C_i = {k\varepsilon_0}/{d}$, where k is the relative dielectric constant of SiO_2 (3.9), ε_0 is the vacuum permitivity, and d is the thickness of the SiO_2 layer (100 nm). The calculated value of C_i is 3.45 $\times 10^{-8}$ F/cm^2. (W/L) is the channel width-to-length ratio, and V_{DS} is the drain voltage. It has been previously reported that V_{TH} shift after the proton irradiation is mainly caused by radiation-induced electron-hole pair production (ionization damage) near or at the ZnO/SiO_2 interface [11]–[13]. When the number of negatively charged interface traps (N_{it}) increases, the barrier potential at the interface increases and widens the interface depletion region [12], [21], [22]. The destructive electric field resulting from the negatively charged traps at the interface causes the V_{TH} shift in positive gate bias direction. The V_{TH} shift in negative gate bias direction has also been reported [11]. The radiation-induced holes trapped in SiO_2 could act as fixed positive charges and enhance the gate electric field, [12] shifting V_{TH} to the negative gate bias direction. Therefore, the observed positive shift in V_{TH} can be merely attributed to the negatively charged interface traps since it is unlikely to accumulate negatively charged traps in SiO_2 after proton (H^+) irradiation. In the case

of the type-Z, the negligible shift in V_{TH} was observed, which indicates that the radiation-induced defects in the bulk of ZnO is not contributing to the interface trap density (D_{it}) for the type-Z.

Since the maximum proton dose is confined to the ZnO/SiO_2 interface in type-I, the atomic displacement damage at the interface might have contributed to the interface trap density increment after the irradiation. The transfer characteristic curve tends to stretch out in the subthreshold region when D_{it} increases in the metal-oxide-semiconductor (MOS) transistors [23]. Hence the subthreshold swing (*SS*) increases with increase in D_{it}.

$$SS = \left(\frac{dlog\ I_D}{dV_{GS}}\right)^{-1} \quad 6.3\text{-}2$$

The shift in subthreshold swing due to the irradiation-induced interface trap density is the difference between the *SS* before and after the irradiation; i.e.,

$$\Delta(SS) = (SS)_{Before} - (SS)_{After} \quad 6.3\text{-}3$$

Once the $\Delta(SS)$ calculated, the increment in number of interface traps can be calculated by

$$\Delta D_{it} = \left(\left[\frac{0.434\ \Delta(SS)}{\left({k_B T}/{q}\right)} - 1\right]\frac{C_i}{q}\right) \quad 6.3\text{-}4$$

where k_B is the Boltzmann constant, T is the absolute temperature (300 K). The calculated ΔD_{it} from the equation (4) are illustrated in figure 6.3-3. The inset of figure 6.3-3 shows the V_{TH} shift after the irradiation for both type-I and type-Z devices. As shown in figure 6.3-3, the interface trap density has dramatically increased after proton bombarded at ZnO/SiO_2 interface for type-I compared to type-Z. Therefore, it can be conjectured that radiation-induced defects at the interface increased the interface trap density, causing the V_{TH} shift to the positive gate bias direction.

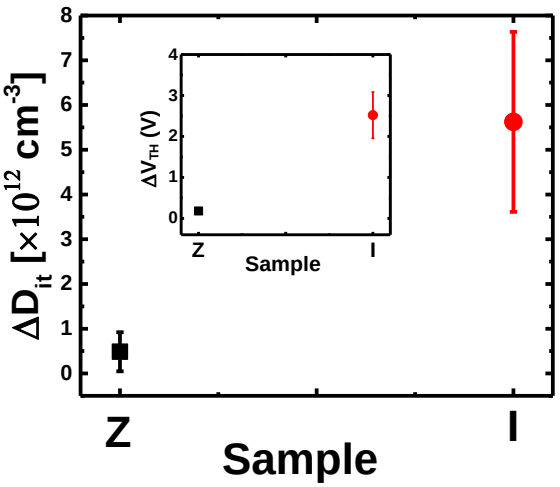

Figure 6.3-3: The increment of interface trap density after the irradiation for type-Z and type-I devices. The inset shows the threshold voltage shift after the irradiation for both types of devices.

Figure 6.3-4 shows the field effect mobility variation with gate bias for type Z and I before and after irradiation. It is known that field-effect mobility (μ_{FE}) variation with gate bias would provide good insight into the interface trap distribution. The μ_{FE} was calculated by using the transconductance data extracted from transfer characteristics and applied to the following equation [21].

$$\mu_{FE(V_{GS})} = \frac{g_{m(V_{GS})}}{C_i\left(\frac{W}{L}\right)V_{DS}} \qquad 6.3\text{-}5$$

where $g_m(V_{GS})$ is the transconductance [$g_m(V_{GS})$= dI_D/dV_{GS}], (W/L) is the channel width-to-length ratio, and V_{DS} is the drain voltage.

As shown in the figure 6.3-4, the μ_{FE} shows a negligible change in type-Z devices while a noticeable reduction in μ_{FE} was observed for type-I devices. This observation further supports the fact that proton irradiation induced traps created at the ZnO/SiO_2 interface are the predominant

contributor to the V_{TH} shift while defects created in ZnO bulk shows the negligible effect on the electrical instability of devices.

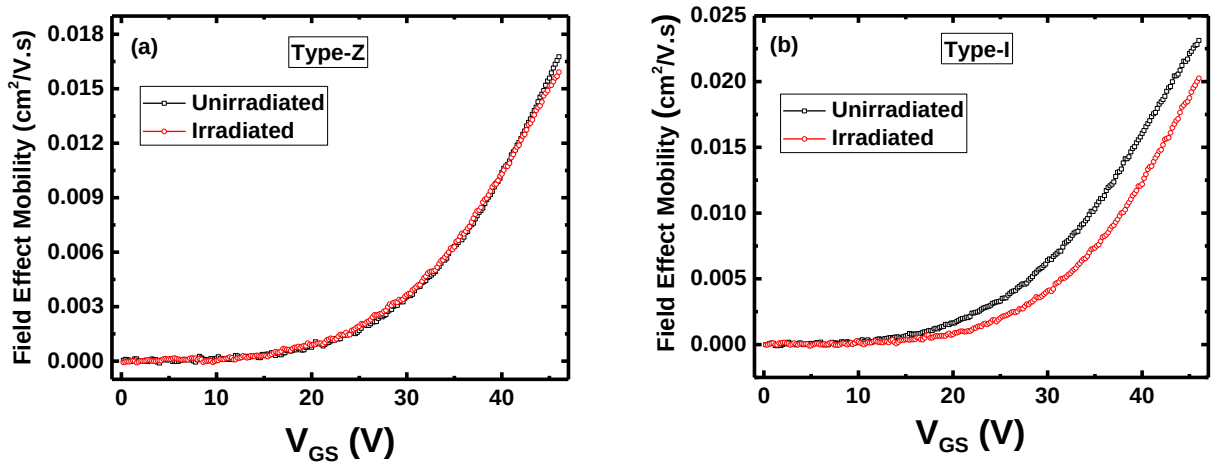

Figure 6.3-4: Field effect mobility *vs.* gate bias for unirradiated and irradiated devices of (a) type-Z, and (b) type-I devices.

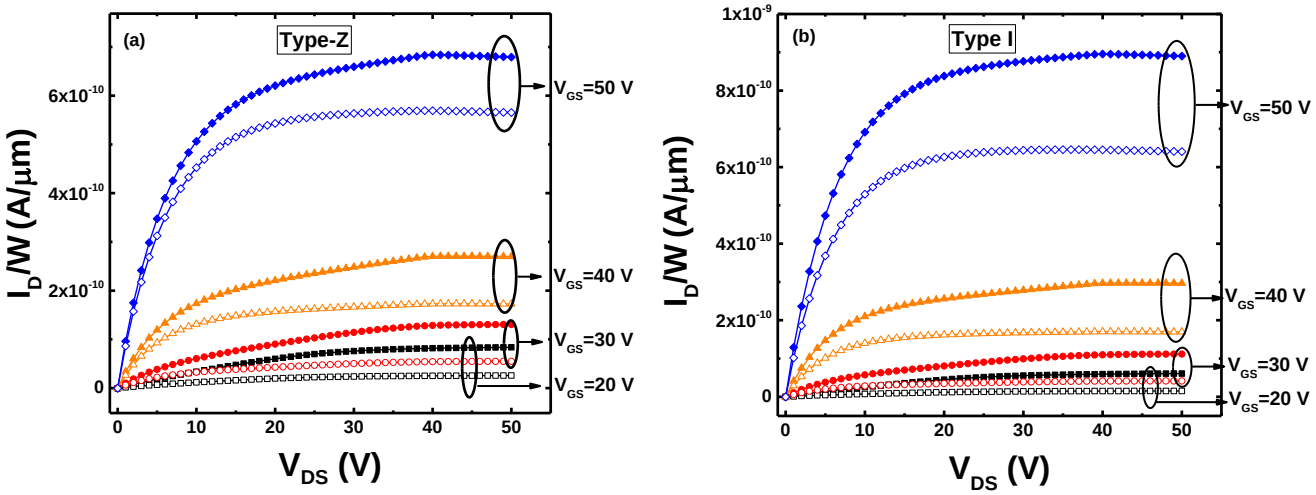

Figure 6.3-5: The output characteristics extracted before and after irradiation for (a) type-Z, and (b) type-I devices. The solid markers and hollow markers indicate unirradiated and irradiated devices, respectively for both (a) and (b).

Figure 6.3-5 shows the output characteristics of type-Z and I devices before and after irradiation. The drain current for all the devices exhibits linear behavior at low source-drain bias and saturates at higher V_{DS}, indicating the typical pinch-off characteristics of *n*-type semiconductor TFTs [25]. As shown in figure 6.3-5, the electrical conductance has decreased in both the samples after the irradiation. A higher reduction in $I_{D,\,sat}$ was observed in type-I (which shows higher ΔD_{it} than type-Z), which implies that a correlation between increased D_{it} and the reduced electrical conductance can be made. The increased D_{it} widens the depletion region at the ZnO/SiO_2 interface [11]. The decreased electrical conductance in the type-I may be attributed to the widening of the depletion region due to the increased proton-induced interface defects. Even though the proton irradiation has induced a negligible V_{TH} shift, the electrical conductance is also reduced in type-Z devices. In the case of the type-Z, proton irradiation has shown no contribution to the depletion region widening at the interface, which is also evidenced by a negligible change in D_{it} before and after irradiation compared to type-I. The $I_{D,\,sat}$ reduction in type-Z might have produced by other types of defects generated in the ZnO layer due to displacement damage. A significant amount of vacancies are generated as a result of displacement damage. The oxygen vacancies (V_O^{2+}) are considerd as deep donors and zinc vacancies (V_{Zn}^{2-}) can be acted as compansating centers in n-type-ZnO [26]. Overall higher NIEL in ZnO layer for type-I devices compared to type-Z devices indicates higher [V_{Zn}^{2-}] to be presented in type-I devices (see figure 6.3-1). The migration of V_{Zn}^{2-} is hindered upto 540 K [26]. Also, implanted H^+ tend to form bound-centered configuration with V_{Zn}^{2-}. The formed complex, $(V_{Zn}\text{-}H)^-$ is the enegetically most favorable configuration and stable upto 1200K [27]. Therefore, a higher concentration of stable negatively charged complex were accumilated at the ZnO/SiO_2 interface and largely contributed to D_{it} in type-I devices.

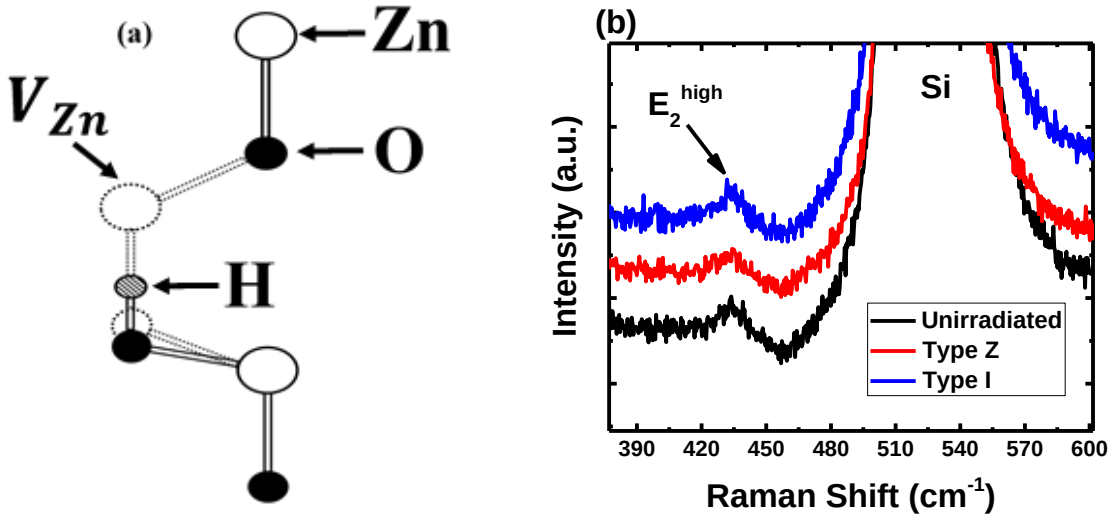

Figure 6.3-6: (a) Schematic of V_{Zn}-H aligned along c-axis. Black, white, and shaded circles represent Zn, O, and H atoms, respectively. (b) room temperature micro-Raman spectra for ZnO channel of type-Z and type-I devices.

Figure 6.3-6 (a) shows the energetically most stable bond-centered configuration of H^+ along c-axis in the ZnO lattice. The neighboring Zn-O bond tends to deform ~ 2 % from its original bond length due to the V_{Zn}-H center[27]. This deformation induces a stress in the ZnO lattice. The stress induced by native defects and incorporated impurities is known as hydrostatic stress [28]. The induced hydrostatic stress can be detected with the shift of Raman frequency [29]. Figure 6.3-6(b) shows the room temperature Raman spectroscopic analysis on ZnO channel of type-Z and type-I devices. In the limits of Hook's law validity, the stress can be calculated with Raman frequency shift as following [30],

$$\Delta\omega\ (cm^{-1}) = 2\tilde{a}\sigma_{xx} + \tilde{b}\sigma_{zz} \qquad 6.3\text{-}6$$

where $\tilde{a}$ and $\tilde{b}$ are phonon deformation constants. The in-plane and normal stress components are denoted as σ_{xx} and σ_{zz}, respectively. For hydrostatic stress (σ_{xx}=σ_{zz}), the equation 6.3-6 can be modified to obtain induced stress in the ZnO film.

$$\sigma_{(film)}(GPa) = \frac{\Delta\omega\ (cm^{-1})}{(2\tilde{a}+\tilde{b})} \qquad 6.3\text{-}7$$

where $\Delta\omega$ is the Raman shift of E_2^{high} peak after the irradiation with respect to the unirradiated sample. The calculated stress values are 83.4 ± 24.3 MPa and 259.3 ± 31.6 MPa for type-Z and type-I ZnO films, respectively.

The ZnO film in type-I devices has undergone significant stress compared to type-Z devices. A higher $[V_{Zn}^{2-}]$ generated through severe displacement damage in type-I devices compared to type-Z devices would form more complexes with implanted H^+, thereby larger stress would induced to the ZnO film as observed in results.

References

[1] A. Johnston, *Reliability and radiation effects in compound semiconductors*, 1st ed., Singapore, World Scientific, 2010, ch. 8, pp. 206.

[2] D. C. Look, D. C. Reynolds, J. W. Hemsky, R. L. Jones, and J. R. Sizelove, "Production and annealing of electron irradiation damage in ZnO," *Appl. Phys. Lett.*, vol. 75, no. 6, pp. 811–813, 1999.

[3] D. R. Locker and J. M. Meese, "Displacement thresholds in ZnO," *IEEE Trans. Nucl. Sci.*, vol. 19, no. 6, pp. 237–242, 1972.

[4] J. A. Van Vechten and S. P. Keller, *Handbook on Semiconductors*, Vol 3, Elsevier, 1980, Amsterdam, North-Holland, ch. 1, pp. 1–111.

[5] D. C. Look, J. W. Hemsky, and J. R. Sizelove, "Residual native shallow donor in ZnO," *Phys. Rev. Lett.*, vol. 82, no. 12, p. 2552, 1999.

[6] C. Coskun, D. C. Look, G. C. Farlow, and J. R. Sizelove, "Radiation hardness of ZnO at low temperatures," *Semicond. Sci. Technol.*, vol. 19, no. 6, p. 752, 2004.

[7] J. I. Ramirez *et al.*, "Radiation-Hard ZnO Thin Film Transistors," *IEEE Trans. Nucl. Sci.*, vol. 62, no. 3, pp. 1399–1404, Jun. 2015.

[8] J. I. Ramirez, Y. V. Li, H. Basantani, and T. N. Jackson, "Effects of gamma-ray irradiation and electrical stress on ZnO thin film transistors," in *71st Device Research Conference*, 2013, pp. 171–172.

[9] F. D. Auret, S. A. Goodman, M. Hayes, M. J. Legodi, H. A. Van Laarhoven, and D. C. Look, "Electrical characterization of 1.8 MeV proton-bombarded ZnO," *Appl. Phys. Lett.*, vol. 79, no. 19, pp. 3074–3076, 2001.

[10] Y.-K. Moon, D.-Y. Moon, S. Lee, and J.-W. Park, "Enhancement of ZnO thin film transistor performance by high-dose proton irradiation," *Nucl. Instrum. Methods Phys. Res. Sect. B Beam Interact. Mater. At.*, vol. 268, no. 16, pp. 2522–2526, Aug. 2010.

[11] G. Jo, W. K. Hong, M. Choe, W. Park, Y. H. Kahng, and T. Lee, "Proton Irradiation-Induced Electrostatic Modulation in ZnO Nanowire Field-Effect Transistors With Bilayer Gate Dielectric," *IEEE Trans. Nanotechnol.*, vol. 11, no. 5, pp. 918–923, Sep. 2012.

[12] W.-K. Hong *et al.*, "Tuning of the Electronic Characteristics of ZnO Nanowire Field Effect Transistors by Proton Irradiation," *ACS Nano*, vol. 4, no. 2, pp. 811–818, Feb. 2010.

[13] M. Choe *et al.*, "UV photoconductivity characteristics of ZnO nanowire field effect transistor treated by proton irradiation," *Thin Solid Films*, vol. 520, no. 9, pp. 3624–3628, Feb. 2012.

[14] S. J. Pearton, F. Ren, E. Patrick, M. E. Law, and A. Y. Polyakov, “Review—Ionizing Radiation Damage Effects on GaN Devices,” *ECS J. Solid State Sci. Technol.*, vol. 5, no. 2, pp. Q35–Q60, Jan. 2016.

[15] J. E. Naugle and D. A. Kniffen, “Flux and energy spectra of the protons in the inner Van Allen belt,” *Phys. Rev. Lett.*, vol. 7, no. 1, p. 3, 1961.

[16] D. M. Sawyer and J. I. Vette, “AP-8 trapped proton environment for solar maximum and solar minimum,” *NASA STIRecon Tech. Rep. N*, vol. 77, 1976.

[17] J. F. Ziegler, “SRIM-2003,” *Nucl. Instrum. Methods Phys. Res. Sect. B Beam Interact. Mater. At.*, vol. 219, pp. 1027–1036, 2004.

[18] J. W. Wilson *et al.*, “Materials for shielding astronauts from the hazards of space radiations,” *MRS Online Proc. Libr. Arch.*, vol. 551, 1998.

[19] I. Jun *et al.*, “Proton nonionizing energy loss (NIEL) for device applications,” *IEEE Trans. Nucl. Sci.*, vol. 50, no. 6, pp. 1924–1928, 2003.

[20] S. R. Messenger *et al.*, “Nonionizing energy loss (NIEL) for heavy ions,” *IEEE Trans. Nucl. Sci.*, vol. 46, no. 6, pp. 1595–1602, 1999.

[21] A. Suresh and J. F. Muth, “Bias stress stability of indium gallium zinc oxide channel based transparent thin film transistors,” *Appl. Phys. Lett.*, vol. 92, no. 3, p. 33502, 2008.

[22] J.-M. Lee, I.-T. Cho, J.-H. Lee, and H.-I. Kwon, “Bias-stress-induced stretched-exponential time dependence of threshold voltage shift in InGaZnO thin film transistors,” *Appl. Phys. Lett.*, vol. 93, no. 9, p. 93504, 2008.

[23] Pj. McWhorter and P. S. Winokur, “Simple technique for separating the effects of interface traps and trapped-oxide charge in metal-oxide-semiconductor transistors,” *Appl. Phys. Lett.*, vol. 48, no. 2, pp. 133–135, 1986.

[24] C. Jagadish and S. J. Pearton, *Zinc oxide bulk, thin films and nanostructures: processing, properties, and applications*, 1st ed., Oxford, UK, Elsevier, 2011, ch. 12, pp. 428.

[25] S. M. Sze and K. K. Ng, *Physics of semiconductor devices*, 3rd ed., New Jersey, USA, John wiley & sons, 2006, ch. 6, pp. 296-297.

[26] A. Janotti and C. G. Van de Walle, “Fundamentals of zinc oxide as a semiconductor,” *Rep. Prog. Phys.*, vol. 72, no. 12, p. 126501, 2009.

[27] M. G. Wardle, J. P. Goss, and P. R. Briddon, “Theory of Fe, Co, Ni, Cu, and their complexes with hydrogen in ZnO,” *Phys. Rev. B*, vol. 72, no. 15, p. 155108, 2005.

[28] H. Harima, “Properties of GaN and related compounds studied by means of Raman scattering,” *J. Phys. Condens. Matter*, vol. 14, no. 38, p. R967, 2002.

[29] G. Callsen *et al.*, “Phonon deformation potentials in wurtzite GaN and ZnO determined by uniaxial pressure dependent Raman measurements,” *Appl. Phys. Lett.*, vol. 98, no. 6, p. 61906, 2011.

[30] J.-M. Wagner and F. Bechstedt, “Phonon deformation potentials of α-GaN and-AlN: An ab initio calculation,” *Appl. Phys. Lett.*, vol. 77, no. 3, pp. 346–348, 2000.

Chapter 7
Conclusions and Future Work

7.1 Conclusions

In chapter 6, the investigation of the device instability of solution based ZnO TFTs was described by studying the time-evolution of electrical characteristics during the electrical gate stressing and subsequent relaxation. Systematic comparison of electrical characteristics between ambient conditions and the vacuum was carried out to identify the effect of oxygen and moisture on device instability. Based on positive V_{TH} shift under both environmental conditions with positive gate stressing and full device recovery with longer relaxation, we have concluded that charge trapping is the predominant device instability mechanism. A significant change in subthreshold swing (*SS*) under the ambient conditions compared to vacuum attests the creation of temporary new defect level coexists with charge trapping in the presence of oxygen and moisture. Time dependence of the threshold voltage shift follows the stretch exponential function under ambient conditions further, confirms the defect level creation with oxygen and moisture adsorption on the channel layer. Other than the well-defined oxygen-related acceptor-like trap creation, we have used a multi-step model to explain H_2O assisted charge trapping. Further, our proposed mechanism of migration of the newly created trap closer to the semiconductor/dielectric interface via grain boundary voids well explains the observed reduction in field effect mobility during the gate-stressing under ambient conditions. Moreover, oxygen and moisture associated traps are acting as deep traps and causing significant degradation in device quality.

In chapter 7, we have investigated the displacement damage effect on the electrical characteristics of ZnO thin film transistors after the proton irradiation. The distribution of proton dose significantly manipulates the degree of displacement damage in different locations in the device structure.The ZnO TFTs with two different passivation layer thicknesses were prepared to obtain the maximum proton dose distribution in two distinct locations in the device structure. The type-Z and the type-I have maximum proton dose in ZnO layer and ZnO/SiO_2 interface, respectively. Hence, the majority of DD effect prevailed in the ZnO bulk and the proximity of ZnO/SiO_2 in type-Z and type-I devices, respectively. The device characteristics of type-I devices degraded more than type-Z after proton irradiation. A slight change in passivation layer thickness has produced drastically different DD effect in the device. The location of the impact of DD effect along the structure resulted in significant change in device performance. Hence, care must be exercised when analyzing the data for the impact of charged particle irradiation on device electrical characteristics. Even though two devices are irradiated with proton beam with the same energy and fluence, the change in thickness (and composition) of the passivation layer may lead to a substantially different proton dose distribution and NIEL, resulting in entirely different device performances. Further, the application of passivation layer with an appropriate thickness corresponding to the proton energies would make the ZnO TFTs highly radiation tolerant towards proton irradiation.

7.2 Future Work

As concluded in chapter 6, a proper passivation layer on ZnO TFTs yields minimum damage due to the proton irradiation. The material and the structure are deciding factor for the effectiveness of passivation layer. Typically, heavy elements (e.g., W, and Au) are used as shielding materials against radiation, and light elements such as polymers are employed as

passivation of electronic devices. However, there are pros and cons of each material as listed in table 7.2-1.

Table 7.2-1 Pros and cons of shielding and passivation materials against charged particle radiation.

Passivation Material	**Pro**	**Con**
Heavy element (e.g., W, Au)	Thinner layer	Secondary radiation
Lighter element (Polymer)	Minimum secondary radiation	Thicker layer

The higher stopping potential efficiently slows down incoming charge particles in heavy elements. Hence, only a thinner layer of heavy element is required for shielding. However, the intense collisions during the stopping process generate secondary radiation. In contrast, light elements generate minimum secondary radiation because of lower stopping potential against incoming charged particles. Therefore, a thicker layer of polymers is required to passivate devices. I have proposed a state of the art passivation layer structure composed of multilayers as shown in figure 7.2-1.

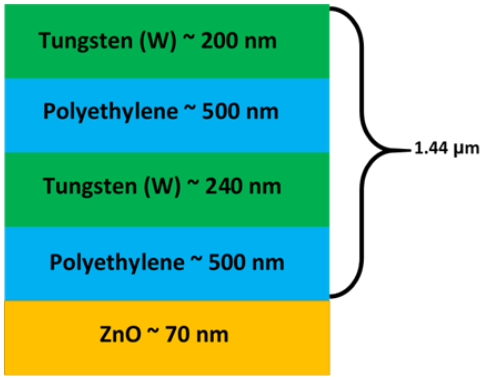

Figure 7.2-1: Schematic cross-section of the multilayer passivation on ZnO.

The thickness of the passivation layer was optimized with the use of different thicknesses of tungsten and polyethylene. The hybrid structure efficiently reduces the secondary radiation and provide efficient shielding. As shown in figure 7.2-2, the NIEL profile in ZnO channel layer indicates that significantly low displacement damage is expected in ZnO TFTs when the proposed multilayer passivation is applied against proton radiation.

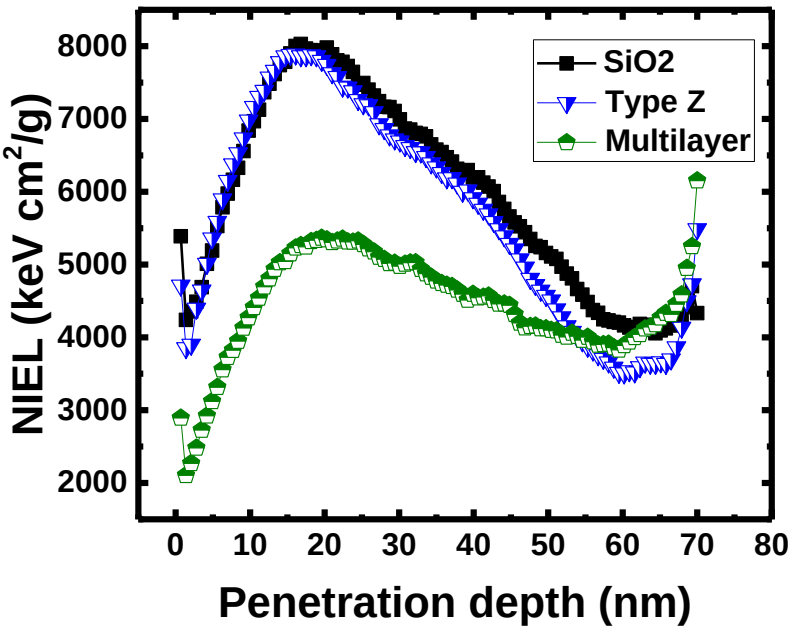

Figure 7.2-2: NIEL profile along the ZnO channel layer under various passivation.

Further experiments and data analysis is required to develop much effective passivation layer to be used under both charged particle and neutral radiation such as neutrons and gamma rays.

Appendices

Appendix I

NIEL Calculation by TRIM Simulation Data

The TRIM simulation ran for 200 keV proton beam with zero angle of incidence for device structure as shown in the Fig. 1 (a), and (b). The TRIM files called VACANCY.TXT was extracted for each sample. The three columns in the VACANCY.TXT file represent the ion depth (D, in $\dot{A}$), the vacancy production rate (in # vacancies/$\dot{A}$/ion) due to ions (IONV,), and recoils (RECV), respectively. The energy needed to produce a vacancy (in keV/vacancy) was calculated by

$$M = \frac{1}{1000}\left[\left(\frac{T_d}{0.4} + 2\right)\right] \quad \text{(A1)}$$

where, T_d is the atomic displacement threshold energy for the atom in the lattice. The 2 is added to allow the binding energy loss accompanied by each vacancy in TRIM simulation, and 1000 is the conversion factor of eV to keV. The M_{Zn} and M_O were calculated by using $T_{d,\,Zn}$= 18.5 eV and $T_{d,\,O}$= 41.4 eV [1], [2]. The NIEL (in keV cm^2/g) as a function of depth was calculated by,

$$NIEL_{(D)} = M\left(INOV_{(D)} + RECV_{(D)}\right)\frac{10^8}{\rho} \quad \text{(A2)}$$

where ,ρ is the density of the target material ($\rho_{ZnO} = 5.605\ g\ cm^{-3}$) [3]. The NIEL for ZnO was determined by weighting the NIEL of Zn and O according to the Bragg's rule [4].

Appendix II

The characterization of proton radiation-induced defects in $ZnO/SiO_2/Si$ device structure.

The influence of defects induced by the $ZnO/SiO_2/Si$ structure and their effect on device performances were studied using the direct exposure of device structure to 200 keV protons with 1×10^{14} protons/cm^2 fluence. The ZnO films were deposited by the spin coating method and post-annealed at 800℃ for 1 hour to obtain polycrystalline phase. The films were directly exposed to proton radiation before device fabrication to avoid the possibility of contact metal damage during the irradiation. The back gate ZnO TFTs were fabricated on unirradiated and irradiated ZnO films to compare the device performances.

Figure A1 shows the transfer characteristics extracted from unirradiated and irradiated ZnO TFTs. The V_{TH} has shifted to negative gate bias direction in irradiated devices compared to unirradiated devices.

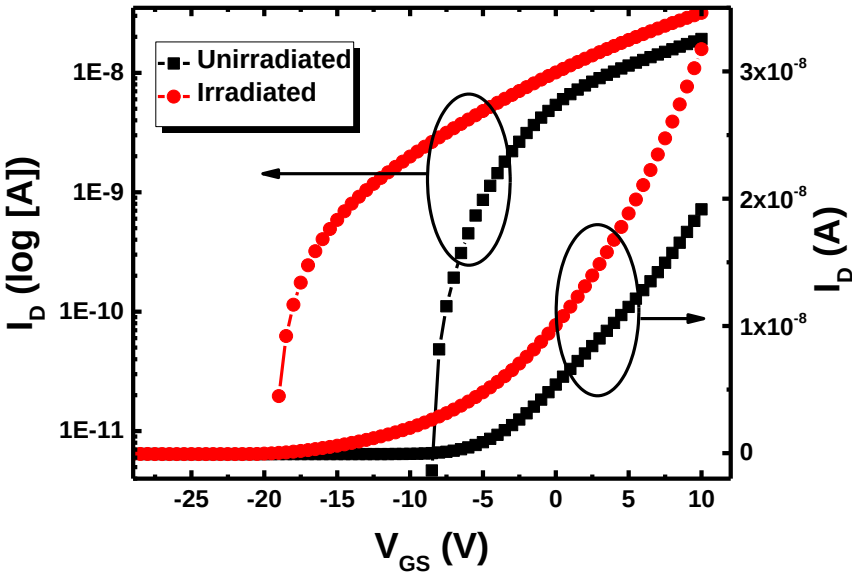

Figure A1: Transfer characteristics of unirradiated and irradiated ZnO TFTs extracted at

V_{DS}=0.1V.

The negative shift in V_{TH} can be attributed to the constructive electric field generated by trapped oxide charges. The total ionizing dose (TID) effect is significant in SiO_2 compared to ZnO. The covalent bonds in SiO_2 can be damaged with few eV energies and caused permeant damage in the lattice structure. The TID effect in SiO_2 has extensively studied under electron, proton and gamma-ray irradiations. The radiation-induced positively charged holes trapped in SiO_2 generate the constructive electric field to shift the V_{TH} along the negative gate bias direction [5], [6]. Also, bombarded proton could generate defects at the ZnO/SiO_2 interface that influence the V_{TH} shift and the reduction in field-effect mobility. The interface trap density was calculated as follows,

$$D_{it} = \left[\frac{0.434.SS}{0.0256} - 1\right]\left(\frac{C_i}{q}\right) \quad \text{(A3)}$$

where C_i is the capacitance of the dielectric layer, SS is the subthreshold swing, and q is the charge of an electron. The calculated D_{it} for unirradiated and irradiated devices were given in table A1.

Table A1: Summery of V_{ON}, V_{TH}, and D_{it} for unirradiated and irradiated ZnO TFTs.

Sample	**V_{ON} (V)**	**V_{TH} (V)**	**D_{it} (cm^{-2})**
Unirradiated	**-8.55**	**- 2.56**	**7.81×10^{12}**
Irradiated	**-19.81**	**- 4.92**	**2.68×10^{13}**

The increased D_{it} in irradiated devices indicates that proton radiation has induced defects at the ZnO/SiO_2 interface. The V_{TH} shift must be manipulated by both trapped oxide charges and interface trap density. In order to identify the role of each type of defects in device performances, the effect of each type defects needs to be eliminated systematically. The irradiated devices were

annealed from 200℃ with 50℃ intervals for 1 minute in ambient. The I-V and C-V characterizations were performed after each annealing step. The figure A2 shows the transfer characteristics of the same device after each annealing treatment.

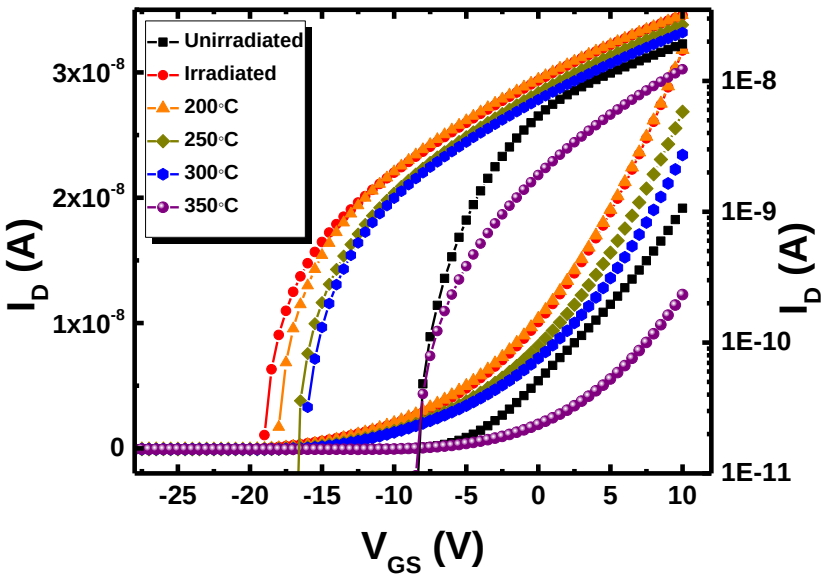

Figure A2: The transfer characteristics of ZnO TFTs under systematic annealing treatment.

The V_{ON} has shifted to positive gate bias direction with the increased annealing temperature. After 350℃, V_{ON} has coincided with the V_{ON} of the unirradiated device. However, after 350℃, the V_{TH} has surpassed the V_{TH} of the unirradiated device. The V_{ON} and V_{TH} shift in positive gate bias direction towards the unirradiated value indicates the annihilation of radiation-induced defects. To identify the type of defects being annihilated, the D_{it} was calculated after each heat treatment. Figure A3 shows the variation of D_{it} with annealing temperature.

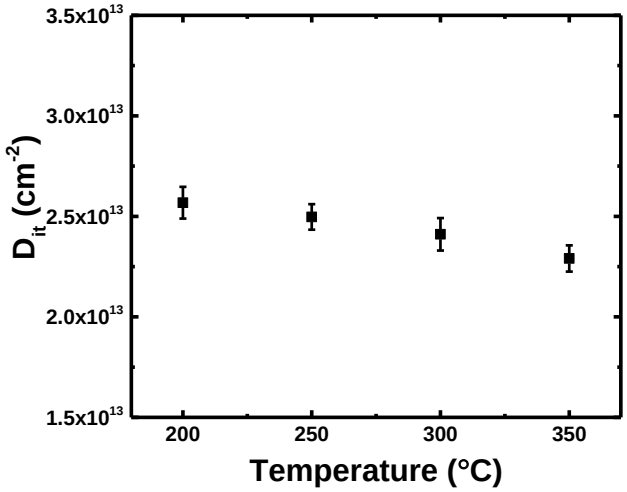

Figure A3: The interface trap density (D_{it}) variation as a function of annealing temperature.

As indicated in figure A3, D_{it} shows negligible change upon the annealing process. This result indicates that the defects at the ZnO/SiO_2 interface have not been affected by the annealing treatment. The field effect mobility was extracted at each temperature to further confirm the behavior of D_{it} with annealing temperature. Figure A4 shows that the field effect mobility as a function of annealing temperature.

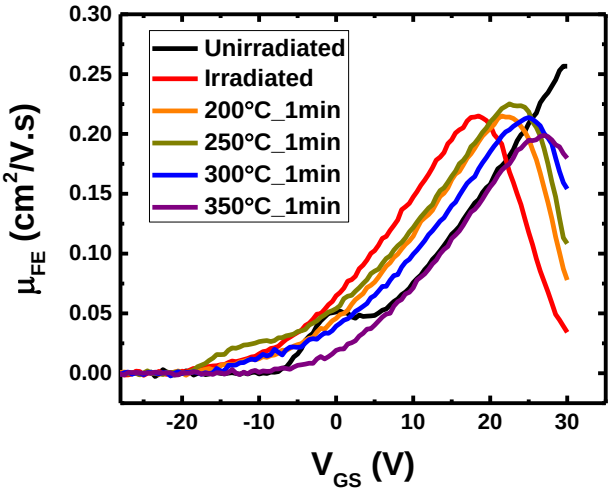

Figure A4: The field effect mobility variation as a function of V_{GS} with the annealing process.

The negligible change in maximum μ_{FE} of irradiated devices with annealing temperature further confirms the fact that D_{it} has not been annihilated during the annealing. Therefore, the shift of V_{TH} along the positive gate bias direction must be caused by the anneal-out of trapped oxide charges. At 350℃, majority of trapped oxide charges have de-trapped.

Therefore, the radiation-induced trapped oxide charges in SiO_2 and traps at ZnO/SiO_2 interface are influencing the device reliability simultaneously. The positive trapped oxide charges generate constructive electric field while negatively charged interface traps generate a destructive electric field at the interface. The substantial number of trapped oxide charges might have generated stronger constructive electric field over interface field. As a result, the V_{TH} has shifted to the negative gate bias direction. Then the heat treatment has annealed out most of the trapped oxide charges and resulted in weakening the constructive electric field. The unchanged D_{it} effect has been dominated at 350℃ in the absence of sufficient trapped oxide charges in SiO_2. The reduced I_D after 350℃ indicates the current reduction due to the interface depletion. The depleted interface due to the D_{it} caused the V_{TH} shift beyond the V_{TH} of unirradiated devices. The figure A5 illustrates the mechanism behind the V_{TH} shift due to trapped oxide charges and radiation-induced $D_{it.}$

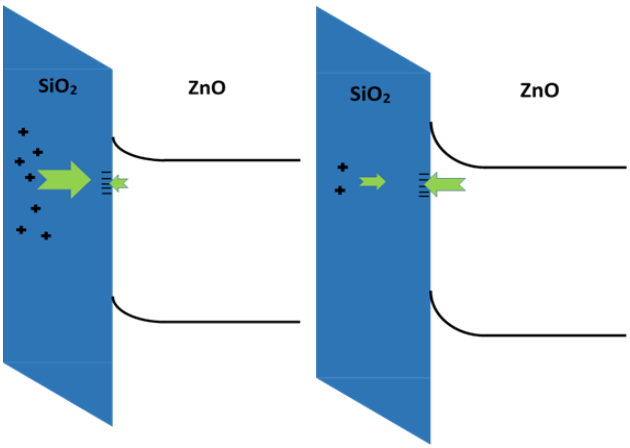

Figure A5: Illustration of ZnO/SiO_2 band diagram under the influence of radiation-induced defects.

The C-V characteristics in figure A6 indicate stretch-out after irradiation and parallel shift with annealing temperature. The stretch-out in C-V curve suggests the increased interface trap density after irradiation. The parallel shift of C-V curve to the positive bias direction represents the reduction of trapped oxide effect with persistent D_{it} effect. This observation supports the fact that D_{it} was unaffected during the annealing and the trapped oxide charges were annihilated.

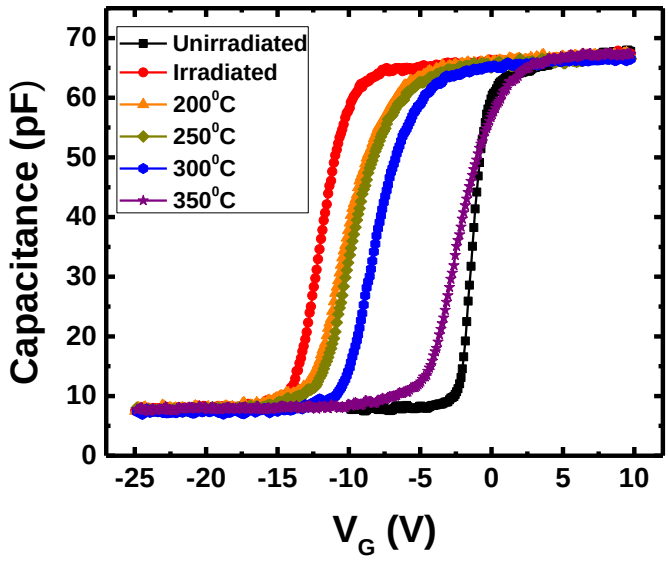

Figure A6: The comparison of capacitance vs. voltage of unirradiated, irradiated, and after each annealing process.

References

[1] J. A. Van Vechten and S. P. Keller, “Handbook on Semiconductors,” *Vol 3North-Holl. Amst.*, pp. 1–111, 1980.

[2] D. C. Look, J. W. Hemsky, and J. R. Sizelove, “Residual native shallow donor in ZnO,” *Phys. Rev. Lett.*, vol. 82, no. 12, p. 2552, 1999.

[3] D. R. Lide, *Hdbk of Chemistry & Physics 73rd Edition*, vol. 73. CRC, 1992.

[4] I. Jun *et al.*, “Proton nonionizing energy loss (NIEL) for device applications,” *IEEE Trans. Nucl. Sci.*, vol. 50, no. 6, pp. 1924–1928, 2003.

[5] G. Jo, W. K. Hong, M. Choe, W. Park, Y. H. Kahng, and T. Lee, “Proton Irradiation-Induced Electrostatic Modulation in ZnO Nanowire Field-Effect Transistors With Bilayer Gate Dielectric,” *IEEE Trans. Nanotechnol.*, vol. 11, no. 5, pp. 918–923, Sep. 2012.

[6] W.-K. Hong *et al.*, “Tuning of the Electronic Characteristics of ZnO Nanowire Field Effect Transistors by Proton Irradiation,” *ACS Nano*, vol. 4, no. 2, pp. 811–818, Feb. 2010.